The Influence of Microstructure on the Deformation and Failure of Ultrafine-Grained Aluminum

by

Adam David Kammers

A dissertation submitted in partial fulfillment
of the requirements for the degree of
Doctor of Philosophy
(Mechanical Engineering)
in The University of Michigan
2014

Doctoral Committee:

Assistant Professor Samantha Hayes Daly, Chair
Professor John Edmond Allison
Professor Krishnakumar R. Garikipati
Professor Michael Thouless
Professor J. Wayne Jones

For Oanh and Elliott

ACKNOWLEDGEMENTS

This thesis would not have been possible without the help and support that came from an excellent group of people that I've worked with at the University of Michigan. First and foremost, I am sincerely grateful for the support and guidance provided by my advisor, Professor Samantha Daly, and my committee. My fellow lab members Jason Geathers, Kyubum Kim, Michael Kimiecik, and Jared Tracy have also been instrumental in the success of my research. I would like to specifically acknowledge Jared who suffered through the early days of SEM-DIC along side of me and was always available for academic and not-so-academic discussions. I would also like to acknowledge my undergraduate research assistant Sara Nitz who assisted me with sample preparation and carrying out numerous UFG experiments. My research wouldn't have been possible without the exceptional training and assistance provided by Dr. John Mansfield, Dr. Haiping Sun, and Dr. Kai Sun at EMAL and Dr. Sandrine Martin, Dr. Pilar Herrera-Fierro, Greg Allion, and Matthew Oonk, at the LNF. I must also thank Bobby Kerns at FEI who always took the time to answer my questions and train me on basic maintenance procedures for the Quanta. Finally, I would like to thank my family for their support and love, especially my wife Oanh and my son Elliott.

TABLE OF CONTENTS

LIST OF FIGURES

LIST OF TABLES

LIST OF APPENDICES

Appendix

LIST OF ABBREVIATIONS

APTMS (3-aminopropyl)trimethoxysilane

ARB Accumulative Roll Bonding

AuNP Gold Nanoparticle

CCD Charge-Coupled Device

DI De-Ionized

DIC Digital Image Correlation

EBSD Electron Backscatter Diffraction

ECAP Equal-Channel Angular Pressing

EDM Electric Discharge Machining

EMAL Electron Microbeam Analysis Laboratory

FEG Field Emission Gun

FIB Focused Ion Beam

FOV Field of View

GIS Gas Injection System

HPT High Pressure Torsion

HFW Horizontal Field Width

HAGB High Angle Grain Boundary

LAGB Low Angle Grain Boundary

LNF Lurie Nanofabrication Facility

LVDT Linear Variable Differential Transformer

MPMDMS (3-mercaptopropyl)methyl)dimethoxysilane

PID Proportional Integral Derivative Controller

SEM Scanning Electron Microscope/Scanning Electron Microscopy

SPD Severe Plastic Deformation

TEM Transmission Electron Microscope/Transmission Electron Microscopy

UFG Ultrafine-Grained

ABSTRACT

The Influence of Microstructure on the Deformation and Failure of
Ultrafine-Grained Aluminum

by

Adam David Kammers

Chair: Samantha Hayes Daly

Ultrafine-grained (UFG) aluminum produced by equal channel angular pressing
(ECAP) is considerably stronger than its coarse grained counterpart, while main-
taining significant ductility. There have been a number of prior investigations into
the material's unique properties, yet the relationships between the heterogeneous mi-
crostructure and the microstructure-scale strain localization and active deformation
mechanisms are not understood, motivating this work. This research investigates the
effect of the material's heterogeneous microstructure on strain accommodation and
clarifies the relationship between macroscopic strain rate sensitivity and the ECAP
processed microstructure.

To carry out this research, a new experimental methodology combining scanning
electron microscopy (SEM) and digital image correlation (DIC) was developed and
utilized. We devised new nano-scale surface patterning techniques, improved SEM
micrograph image distortion correction methodologies, and provided a better under-
standing of the effects of SEM imaging parameters on noise in DIC data. This work
significantly improved this methodology and enabled highly accurate displacement

measurements.

Application of this experimental methodology to UFG 99.99% pure aluminum was used to characterize the relationships between the microstructure and active deformation mechanisms. Analysis of room temperature *in-situ* tension tests revealed that dislocation slip was the primary deformation mechanism in large grains and in grains separated by low angle grain boundaries. In regions of microstructure possessing ultrafine grains separated by high angle grain boundaries, strain localized primarily at grain boundaries. Grain boundary sliding was active at high angle grain boundaries separating distinct banded microstructure features.

Variable strain rate experiments carried out at 200°C revealed the microstructural features responsible for the UFG 99.99% pure aluminum's enhanced strain rate sensitivity. Dislocation slip, active in large grains and grains with similarly oriented slip systems, limited strain rate sensitivity. High angle grain boundaries, particularly those separating banded microstructure features, showed the greatest strain rate sensitivity.

CHAPTER I

Introduction

1.1 Ultrafine-Grained Metals

Ultrafine-Grained (UFG) metals have an average equiaxed grain size of between 100 nm and approximately 1 µm [180, 181, 186], and are of interest due to their ability to achieve increased strength over their coarse-grained counterparts while maintaining significant ductility [42, 46, 179, 186]. The strength increase is a direct consequence of the reduction in grain size and follows the classic Hall-Petch relationship:

$$\sigma_y = \sigma_0 + k_y d^{1/2} \tag{1.1}$$

where d is grain diameter, σ_y is the yield stress, σ_0 is the intrinsic yield stress, and k_y is a material constant. These unique properties make UFG materials interesting from a fundamental perspective and attractive for numerous commercial applications [11, 114, 187].

Ultrafine-grained metals can be synthesized through numerous top-down and bottom-up techniques. In top-down processes the UFG microstructure is developed from a material with an initial coarse-grained structure, while in bottom-up processes the material is produced from building blocks as small as individual atoms. The first

top-down technique was developed by Bridgman in 1943 [21, 22], in which a thin metal disc was compressed between two anvils while torsion was applied, similar to the current technique referred to as High Pressure Torsion (HPT). The goal of this work was to improve the ductility of brittle materials, but grain refinement was not sufficient to lead to mechanical property enhancements due to the low stresses applied. Bottom-up techniques to produce nanocrystalline and UFG metals were first developed by Herbert Gleiter and colleagues in 1989 [61]. Since then, many techniques, including bottom-up and top-down methods, have been developed to produce UFG metals. The most common bottom up methods are electrodeposition [44], inert gas condensation [61], ball milling and subsequent consolidation [96], and cryomilling with hot isostatic compression [117, 196]. These bottom-up methods have shortcomings that include only being able to produce very small samples that contain residual porosity and low levels of contamination.

Recently, top-down Severe Plastic Deformation (SPD) processing techniques have gained attention due to their ability to produce bulk, fully dense UFG material. SPD techniques generate ultrafine-grained materials from coarse grained materials through the application of very high strain which leads to a high dislocation density, which re-arrange into grain boundaries through continued processing. SPD is capable of producing bulk UFG materials at relatively low temperatures and without changing the material dimensions. On the other hand, conventional processing techniques such as rolling and extrusion cannot apply a high enough strain to generate the UFG microstructure. Conventional techniques also reduce the dimensions of the material, limiting the amount of processing that can be carried out. Common top-down SPD processing techniques are Equal-Channel Angular Pressing (ECAP) [79, 186], HPT [163, 203], and Accumulative Roll Bonding (ARB) [148]. Bulk UFG materials produced by SPD have a fairly equiaxed and homogeneous microstructure, with a high percentage of High Angle Grain Boundary (HAGB)s. The material studied in

this work was produced by ECAP and thus the following section will focus on its development and application.

1.2 Equal Channel Angular Pressing

Equal channel angular pressing was developed by Segal in 1981 [155]. However, the unique properties achieved in the materials processed by ECAP went unnoticed until the 1990s [183, 185]. These early works encouraged further development of the ECAP technique and investigation of ECAP processed materials.

ECAP is the most widely used SPD technique due to its ability to be applied to large billets, ease of application, applicability to a wide range of materials, and promise for scaling up for industrial applications. Typical ECAP billets are 10mm in diameter, but recent work has investigated scaling the billet size up for industrial applications, resulting in processed billets with cross sections as large as 100 mm x 100 mm [26, 70]. ECAP has been applied to many engineering metals including aluminum [71, 75, 197], magnesium alloys [49, 199], steel [56, 158], and titanium [159, 165, 187].

1.2.1 ECAP Processing Fundamentals

ECAP processing is a discontinuous process in which a billet of material is repeatedly pressed through the ECAP die shown in figure 1.1(a) typically at room temperature. The ECAP die contains a constant cross-section round or square channel which is bent through an angle Φ of typically 90° as shown in figure 1.1(b). To prevent a "dead zone" from forming at the bend corner, an outer arc of curvature Ψ of 20° − 30° is used [90, 91], see figure 1.1(b). Each time the billet is pressed through the die, it is subjected to simple shear strain at the channel bend. The imposed strain is affected by the ECAP channel intersection angle Φ, and the outer arc of curvature Ψ. A square element pressed into the channel is distorted into a rhombohedron by the shear strain as it passes through the channel angle. This shear strain, γ can be

3

calculated from first principles as [79]

$$\gamma = 2\cot\left(\frac{\Phi}{2} + \frac{\Psi}{2}\right) + \Psi\csc\left(\frac{\Phi}{2} + \frac{\Psi}{2}\right) \tag{1.2}$$

The equivalent strain is [79]

$$\epsilon_{eq} = \left[\frac{2\left[\epsilon_x^2 + \epsilon_y^2 + \epsilon_z^2 + \frac{\gamma_{xy}^2 + \gamma_{yz}^2 + \gamma_{zx}^2}{2}\right]}{3}\right]^{1/2} \tag{1.3}$$

Thus after one cycle, a strain of [79]

$$\epsilon = \left[\frac{2\cot\left(\frac{\Phi}{2} + \frac{\Psi}{2}\right) + \Psi\csc\left(\frac{\Phi}{2} + \frac{\Psi}{2}\right)}{\sqrt{3}}\right] \tag{1.4}$$

is achieved. After N passes through the die, the imposed strain is equal to [79]

$$\epsilon = N\left[\frac{2\cot\left(\frac{\Phi}{2} + \frac{\Psi}{2}\right) + \Psi\csc\left(\frac{\Phi}{2} + \frac{\Psi}{2}\right)}{\sqrt{3}}\right] \tag{1.5}$$

In this work, with an ECAP die possessing a Φ of 90°, a Ψ of 20°, and processing through four passes, the imposed strain is 4.22.

Numerous processing routes, and combinations of routes can be utilized for ECAP processing [48, 58, 72, 76, 78, 154] as shown in figure 1.2. The different routes affect the final grain shape, grain boundary characteristics, and texture. Route A (figure 1.2(a)) in which the sample is not rotated between passes, continually increases the distortion of the rhombohedron. This acts to continually change the shape of the element in the X and Y planes, but does not deform the cube at all in the Z plane.
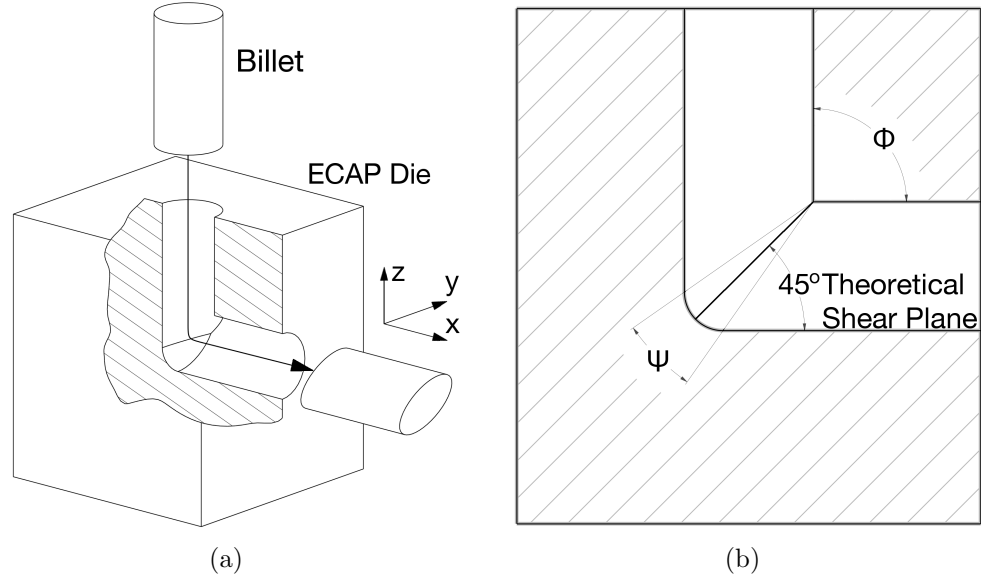
Figure 1.1: In ECAP processing, the billet of material is pressed through the ECAP die, (a). The constant cross-section channel allows the billet to be repeatedly pressed through the die. The important die parameters (b) are the channel intersection angle Φ and the outer arc of curvature Ψ. The theoretical shear plane is controlled by Φ. Shear actually occurs in a fan shaped region surrounding the theoretical shear plane.

Route B_A (figure 1.2(b)) in which the billet is alternately rotated by +/- 90° between passes, continuously changes the shape of the element in all planes, but never returns it to the original cubic shape. Route B_C (figure 1.2(c)) in which the billet is rotated by 90° in the same direction between passes, deforms the element in all planes and returns it to its original cubic shape after 4n passes. Route C (figure 1.2(d)) in which the billet is rotated by 180° between passes, deforms the billet in the X and Y planes but not Z. Route C returns the element to its original cubic shape every 2n passes. Since routes B_C and C return the element to its original shape, they are preferred over routes A and B_A. Route B_C is ultimately the most used route since it additionally deforms the billet in all planes which should yield an equiaxed UFG microstructure after 4n passes. Four passes of route B_C was utilized to process the high purity aluminum for this work.
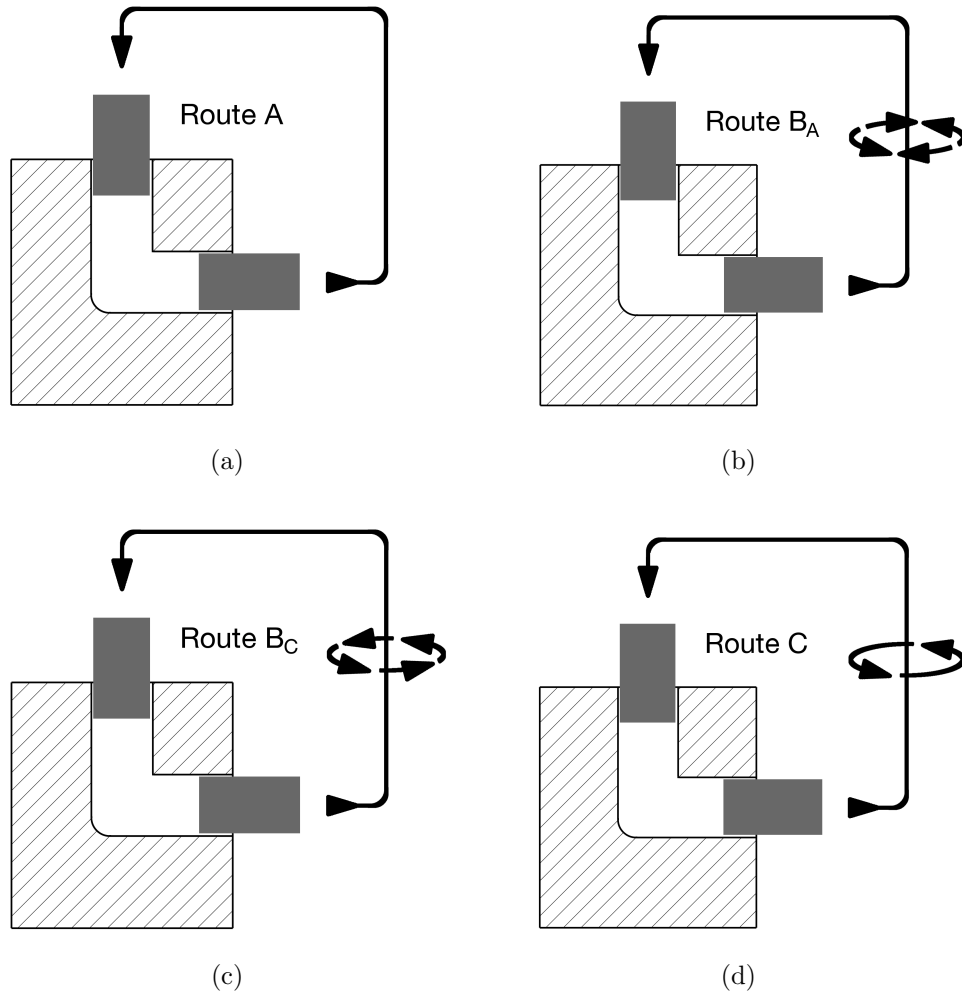
Figure 1.2: The four most common ECAP processing routes. In route A (a) the billet is reinserted with zero rotation. In route B_A (b) and B_C (c) the billet is rotated between passes by 90° in alternating directions and the same direction, respectively. In route C (d) the billet is rotated by 180° between passes.

1.2.2 Microstructure Development

Microstructure evolution in ECAP processing has been thoroughly studied [75, 78, 89, 103, 198, 204]. The angle of the ECAP die channel intersection angle, Φ, has a strong effect on the ECAP microstructure, particularly the inclination angle of grain boundaries. Under a shear strain model, the first pass will result in a grain inclination angle θ_r in respect to the exit channel axis of

$$\theta_r = \cot^{-1}\left(2\cot\left(\frac{\Phi}{2}\right)\right) \tag{1.6}$$

This grain inclination angle changes with each ECAP pass differently based on the processing route being used as shown in table 1.1.

Number of Passes	Grain Inclination Angle (°)			
	Route A	Route B$_\text{C}$	Route B$_\text{A}$	Route C
1	26.6	26.6	26.6	26.6
2	14.0	19.5	19.5	Equiaxed
3	9.5	26.6	12.6	26.6
4	7.1	Equiaxed	10.0	Equiaxed

Table 1.1: Calculated grain inclination angles for different processing routes and number of passes [206].

After the first ECAP pass, the coarse grains are fragmented into arrays of subgrains separated by Low Angle Grain Boundary (LAGB)s. These subgrains are elongated in a banded structure with an average length of 10.1 µm and width of 1.3 µm for the 99.99% pure Al studied in this thesis, and angled at near the predicted grain inclination angle of 26.6°. After one pass, only 11% of the grain boundaries are HAGBs. After two passes following route B$_\text{C}$, the banded microstructure is still apparent, however the subgrains have been fragmented so that they approach equiaxed grains with an average size of 1.8 µm. Additionally, 25% of the grain boundaries are HAGBs. After three passes, the subgrain boundaries evolve into HAGBs (29%)

and the average UFG grain size is 1.4 µm. After four passes, the microstructure is equiaxed and homogeneous with an average grain size of 1.3 µm and a high percentage of HAGBs (50%). With continued processing, the grain size remains consistent, but the percentage of HAGBs continues to increase, up to 74% after twelve passes. Note that these are general characteristics, as the reader will find in chapters IV and V, the four pass ECAP processed microstructure shows significant variation, with many grain boundaries still primarily elongated at an angle of 26.6°.

The equilibrium grain size of the ECAP processed materials is controlled by the rate of recovery of the material being processed. The width of the subgrains after the first pass [78, 176] is very close to the subgrain size reported in material processed by conventional cold working such as extrusion [156]. Thus, the deformation in ECAP is analogous to the deformation that occurs in conventional cold working processes. However, since ECAP allows the material to be repetitively processed, the subgrain boundaries are allowed to evolve into HAGBs by absorbing dislocations. Studies of pure aluminum, and Al-Mg solid solution strengthened alloys [77] demonstrated that as the magnesium content increased, the equilibrium grain size was reduced from 1.3 µm for pure Al to 0.27 µm for Al – 3% Mg. This can be explained by the fact that as the magnesium content increases, and more Mg atoms are present in the Al matrix, the dislocation mobility is reduced. This reduces the recovery rate of the material and also requires additional ECAP straining steps to reach an equiaxed grain size. The fact that dislocation mobility controls the final post-ECAP grain size is further proven by the fact that the equilibrium grain size in pure Cu (Stacking fault energy (SFE): $\sim$40 mJ/m^2) is 0.27 µm while in pure Al (SFE: $\sim$200 mJ/m^2) it is 1.3 µm [99].

The shear deformation that occurs in ECAP has a strong influence on the crystallographic orientation of the post-ECAP billet. In investigations performed by Stout [166, 167], it was found that in copper, {111} slip planes became parallel with the

shear plane when subjected to torsional deformation. Thus, since the shear plane is angled at 45° in ECAP, it is expected that the {111} slip planes should also take this orientation. But, rigid body rotation caused by the constraint forces in the ECAP die results in the {111} slip planes making a smaller angle with the ECAP exit channel axis. Zhu [206] predicted that the {111} slip planes would be angled between 26.6 and 45° after the first pass and change with subsequent passes. This has been confirmed in numerous experimental investigations [2, 75, 136, 204]. The results presented in chapters IV and V of this work will demonstrate that the slip planes still have this preferred angle even after four passes.

The majority of the prior work on ECAP processing has concluded that processing through four passes of route B_C yields a homogeneous microstructure. However, this is not always true, as the post-ECAP microstructure is strongly influenced by the initial coarse-grained microstructure [111, 198, 206]. The microstructure after four passes may consist of ultrafine-grains which are separated by primarily HAGBs [89], ultrafine-grains separated by primarily LAGBs referred to as "supergrains" (defined by D.L. Davidson [35] as groups of grains in which the slip planes in adjacent grains are oriented within 15° of each other), or ultrafine-grains arranged in bands that have been designated "deformation bands" [128, 204]. Here, the term "banded microstructure" is instead used to avoid confusion when discussing Digital Image Correlation (DIC) measured surface deformations. 135,000 µm^2 of the ECAP processed microstructure across 17 tension specimens was analyzed by Electron Backscatter Diffraction (EBSD). 40% of this area was composed of an ultrafine-grained microstructure, 36% was composed of supergrains, and 24% was composed of microstructure bands. Note that the bands in banded microstructure are supergrains but are not included in the percentage of supergrains. Figures illustrating each of these microstructures are provided in chapters IV and V.

1.2.3 Mechanical Properties

UFG metals are significantly stronger than their coarse-grained counterparts due to the reduced grain size and high percentage of grain boundaries. For conventionally processed metals, as strength increases, the ductility decreases [137]. Processing by ECAP can lead to a final material that exhibits superior strength and ductility and whose properties are largely affected by strain rate. Experiments were performed by Horita [71] to investigate the strength and ductility evolution in ECAP processing of commercially pure Al and numerous Al alloys. These experiments found that the greatest increase in yield strength and ultimate tensile strength occurred after one pass. These values continued to increase with subsequent passes at a reduced rate. Ductility underwent the largest decrease after one pass, and subsequently remained constant with additional passes. These experiments also compared the properties of 3004 Al processed by both cold rolling and ECAP. It was found that the yield strength increased with increasing straining of the material for both cold rolling and ECAP. For both processes, ductility decreased by the same amount up to an equivalent strain of 1. Thereafter, ductility remained unchanged for further ECAP processing, while it continued to decrease at a lesser rate for cold rolling.

Valiev performed similar experiments comparing cold rolling and ECAP processing of 99.996% Cu [179]. Cu rolled to a 60% reduction in thickness had a yield strength that was approximately 7 times greater than that of the coarse-grained material. However, the ductility was greatly decreased and the material did not work harden. The Cu processed by two ECAP passes behaved similarly with an 8 times increase in yield strength and only slightly more ductility than the rolled material. However, processing the material through sixteen ECAP passes further increased the yield strength and resulted in a ductility similar to the coarse grained material.

In work by Dvorak on super high purity 99.999% Al [42], ductility was also observed to increase with an increasing number of passes, but unlike with the copper,

the strength decreased with pass number. In this work, it was noted that after two passes, the microstructure consisted of subgrains separated by LAGBs, with an average grain size of 2 µm. Yet after eight passes, the average grain size was 15 µm. The grains were separated by HAGBs but contained smaller subgrains with low dislocation densities. The decrease in strength is explained by the fact that the HAGBs present after a greater number of passes act as sinks for dislocations generated within the grains. This leads to a reduction in dislocation density and fewer tangled dislocations at subgrain boundaries, which reduces the strength of the material. Different results are observed in Al alloys and lower purity Al due to the lessened dislocation mobility due to impurities. Likewise in Cu, the lower stacking fault energy reduces dislocation mobility and thus leads to the continuous increase in strength with further processing. Enhancements to the mechanical properties of other ECAP processed materials and work being done to achieve greater property improvements is beyond the scope of this work, but can be found in [186].

1.2.4   Prior Work

The microstructure-scale strain localization behavior and deformation mechanisms active in ECAP processed aluminum are not fully understood, motivating the investigations carried out in this work. ECAP-processed pure aluminum and its alloys have been examined in prior experimental and computational research, with the majority agreeing that grain boundaries play an important role in the plastic deformation of the material. Several unanswered questions remain, including what deformation mechanisms lead to the enhanced ductility over cold rolled materials, what deformation mechanisms are responsible for the enhanced strain rate sensitivity of the materials, and how does the microstructure affects strain localization.

Grain boundary sliding, a diffusion deformation mechanism typically only considered to be active at elevated temperatures and low strain rates, is thought to be

active at lower temperatures in UFG materials. This behavior is thought to result from the large volume of non-equilibrium high-energy grain boundaries possessing extrinsic, or non-geometrically necessary dislocations [57, 103, 106, 157, 178, 179, 182]. These extrinsic dislocations are able to move along the boundaries enabling sliding without the high temperatures necessary for diffusion. Additional studies have found ECAP processed materials to display enhanced grain boundary diffusion at lower temperatures [8, 41, 141, 150].

Numerous constant strain rate tension/compression experiments performed on ECAP processed aluminum and its alloys have found evidence of grain boundary sliding [100, 144, 145, 146]. These works looked at the post-test surface and found surface relief indicative of grain boundary sliding and micro shear banding. However, while microstructural data from EBSD was used by Ivanov et al. [100], the surface deformation was not related to specific microstructural features and the studies treated the microstructure as being homogeneous. Constant strain rate micro-indentation tests have also been utilized [19, 30, 31]. The works by Chinh et al. [30, 31] measured abrupt steps in the surface surrounding the indentation, with spacing between steps equal to the grain size of UFG pure Al being indented. On the other hand, Böhner et al. [19] did not see these steps and instead saw homogeneous pile-up around the indentation. Böhner et al. also commented that grain boundary sliding is enhanced by indentation tests. Additional tests by Böhner et al. allowed for the calculation of the activation volumes which were in the range of grain boundary diffusion processes. The authors concluded that thermally activated annihilation of dislocations based on slip and diffusive climb processes in the grain boundaries with subsequent recombination were active in the material and responsible for the strain rate sensitivity.

The activation energy or activation volume is often calculated to determine the deformation mechanisms responsible for the strain rate sensitivity of the material. Yu et al. [123] processed an Al-Mg-Si alloy through ECAP with parallel channels,

and then strained samples in tension at 10^{-3} s^{-1}. The activation volume, calculated from the relaxation of the material, was 104–469 b^3 after one and two ECAP passes, where b is the length of the Burgers vector. These values are in the range of thermally activated dislocation glide overcoming dislocation forests. After six passes, when more HAGBs were present, an activation volume of 65–82 b^3 indicated thermally activated annihilation of dislocations at grain boundaries. Additional tests which calculated the activation volume or activation energy concluded that thermally activated climb-controlled annihilation of lattice dislocations in grain boundaries is the source of rate sensitivity [19, 28, 69, 119], as opposed to grain boundary sliding. In a novel experiment by Wheeler et al. [195], strain rate indentation testing was performed at varying temperatures. This work found that while steps on the surface from grain boundary sliding were apparent, activation energies at room temperature are in the range of climb and glide of grain boundary dislocations. As the temperature increased, the deformation mechanism changed to dislocations emitted from grain boundaries. At the highest temperatures of 200 ℃ and 250 ℃, diffusion of aluminum along grain boundaries occurred.

Computational models have been developed to study ECAP processed material. Tomotsugu et al. [157] utilized molecular dynamics to determine that extrinsic grain boundary dislocations function as intergranular deformation sources under shear loading, by decomposing the burgers vector into the normal and parallel components to the grain boundary. Ahmed et al. [3], utilizing a crystal plasticity model that coupled dislocation dynamics and diffusion kinetics simulations, found that grain boundaries act as barriers to dislocation motion. Grain boundaries also absorbed lattice dislocations and transformed them into glide and climb dislocations. Additionally, dynamic recovery at grain boundaries maintains conventional plasticity within grains. Work by Wei et al. [194] developed a mesoscopic continuum model of a two-dimensional polycrystal. The model was capable of accommodating grain interior plasticity, grain-boundary

diffusion and grain-boundary sliding. The results showed that the enhanced strain-rate sensitivity results from the transition to creep under combined grain boundary diffusion and sliding.

To date, there have been few tests (on a UFG cryomilled Al-Mg alloy) that have utilized EBSD and DIC [4, 5, 202]. Ahn et al. [4, 5] used optical microscopy to determine that a bimodal grain size enabled greater dislocation mobility in the coarse grained region. However, due to the large Field of View (FOV) and limited spatial resolution, it is difficult to relate the strain localization to the microstructure. Zhang et al. [202] performed experiments in a Scanning Electron Microscope (SEM) and concluded that larger grains are more likely to exhibit plastic deformation than smaller grains. This work also used a wide FOV and, due to smeared strain values and possibly a large step size, it is difficult to relate strain localization to grains and grain interiors. All of these works were combined with EBSD, but only grain size data was utilized.

There is a lack of experimental investigations relating strain rate sensitivity and strain localization to the underlying microstructure of the material. This information is important and could be utilized to modify the ECAP technique to yield materials that are specialized to exhibit greater strength, or extensive ductility. Thus this thesis will both investigate the deformation mechanisms active in the material and also determine the microstructural features that are most responsible for damage nucleation.

1.2.5 Commercialization

Commercialization of ECAP processed materials is an active area of research. One of the first hurdles is to verify that the technique can be scaled up to produce large scale billets. Recent research has showed promise in scaling up the billet size and utilizing the processed material for forging stock. Horita et al. [70] ECAP

processed Al billets from 6 - 40 mm in diameter and found that grain refinement was independent of billet size and the pressing load was dependent on the material's strength. Chaudhury et al. [26] processed billets of 6061 aluminum with square cross sections as large as 100 x 100 mm. The processed material was then used as forging stock, with the results demonstrating that the forgeability improves following ECAP and forging can be carried out at lower temperatures and produce less waste.

There is also active research in modifying the ECAP process to make it continuous, thus removing the need for reinsertion of the billet into the die. One of the continuous techniques is referred to as ECAP-conform and can be used to continually process wire [138]. It has been successfully applied to aluminum wires with diameters near 3 mm. Continuous processing which utilizes existing rolling equipment is also being developed for sheet samples [66, 107, 108, 147].

Applications for ECAP processed material are rapidly being developed. Current research on the application of ECAP processed materials primarily focuses on their use for hydrogen storage and medical implants. ECAP processed magnesium shows promise for hydrogen storage [86, 160, 161, 162]. Mg is the only pure metal capable of reversibly storing up to 5% hydrogen, however the hydrogen desorption rate is very slow in coarse grained form. ECAP processing of the material can lead to a 50% increase in the desorption rate. ECAP processed titanium is also being studied for dental and other orthopedic implants due to its enhanced strength and osteoblast cell compatibility as compared to coarse grained titanium [45, 104, 131, 187, 192].

1.3   Digital Image Correlation

In this work, the optical metrology technique DIC is combined with SEM and EBSD. This section will begin with an introduction to the DIC technique, followed by a discussion on the challenges associated with combining DIC with SEM (termed SEM-DIC).

1.3.1   Fundamentals

DIC is a non-contact optical metrology used to measure full field displacements and strains on the surface of an object. It was developed at the University of South Carolina in the 1980s [23, 133, 134]. DIC has no inherent length scale and has been applied to fields of view ranging in size from microns in width to those containing entire civil structures. DIC utilizing a single image sensor is capable of measuring displacements in the image sensor plane, with out of plane displacements appearing as dilatory strains. Two image sensors enable 3-dimensional DIC measurements [67, 115]. However, the use of two sensors introduces the need for a thorough calibration procedure to determine the locations of the two cameras with reference to each other.

DIC measures full-field displacements by tracking the motion of markers that have been applied to the surface of the body under study. The pattern created by these markers should be dense, isotropic, high contrast, and random as shown in figure 1.3. The appropriate speckle size follows a general rule that each speckle should cover approximately 3 x 3 pixels [174]. Application of these tracking markers can be a difficult part of a small-scale DIC experiment. For macro-scale experiments, the markers are often applied by sprinkling toner powder over the surface or spraying it with paint from an airbrush or spray can [172]. Techniques for applying a surface pattern in micro-scale experiments will be presented later in this work.

To start the DIC test, a reference image is first taken of the patterned surface under study in its unloaded state, as represented by the dogbone on the left of figure 1.4. As the sample is deformed, additional images are captured. To determine deformation, each deformed image is broken up into small "subsets" represented by the yellow boxes in figure 1.4. Each subset should be sized to contain at least 3 x 3 speckles [174] to ensure the best accuracy. The subsets, each having a unique greyscale intensity distribution due to the surface pattern, are then matched to the undeformed subsets in the reference image by minimizing a normalized cross-correlation function, S:
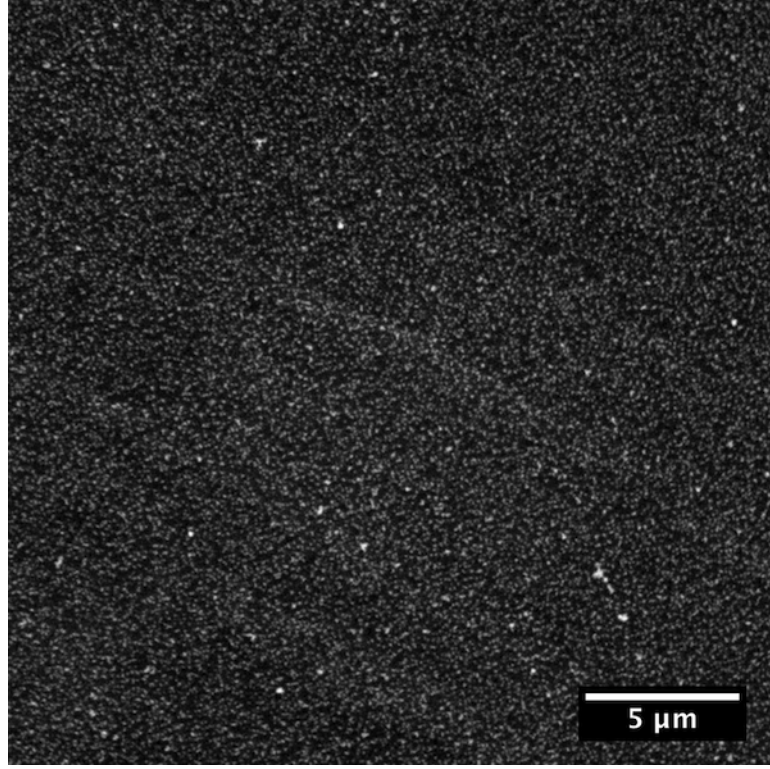
Figure 1.3: DIC tracking pattern composed of 60 nm diameter gold nanoparticles on a high purity aluminum substrate. This pattern was imaged in a SEM with the secondary electron detector.

$$S\left(x, y, u, v, \frac{\partial u}{\partial x}, \frac{\partial u}{\partial y}, \frac{\partial v}{\partial x}, \frac{\partial v}{\partial y}\right) = 1 - \frac{\sum\left[F\left(x, y\right) \cdot G\left(x^*, y^*\right)\right]}{\left[\sum F\left(x, y\right)^2 \cdot \sum G\left(x^*, y^*\right)^2\right]^{1/2}} \qquad (1.7)$$

In equation 1.7, the variable $F\left(x, y\right)$ is the pixel intensity value at point (x, y) in the reference image and $G\left(x^*, y^*\right)$ is the pixel intensity value at the deformed position of the point, (x^*, y^*). The values of $(u, v, \partial u/\partial x, \partial u/\partial y, \partial v/\partial x, \partial v/\partial y)$ that minimize S describe the subset center displacement (u, v) and subset distortion $(\partial u/\partial x, \partial u/\partial y, \partial v/\partial x, \partial/\partial y)$. If motion is on a plane perpendicular to the optical axis, the deformed position (x^*, y^*) can be approximated by a 2D affine transformation, where in 1.8 and 1.9, Δx and Δy are the distance from the subset center:

17

$$x^* = x + u + \frac{\partial u}{\partial x}\Delta x + \frac{\partial u}{\partial y}\Delta y \tag{1.8}$$

$$y^* = y + v + \frac{\partial v}{\partial x}\Delta x + \frac{\partial v}{\partial y}\Delta y \tag{1.9}$$

Improvements to DIC since its development include speed increases and improvements in accuracy. Gains in computation speed were achieved through the application of the Newton-Raphson method to search for matching subsets [23, 173] in place a previous coarse-fine iterative technique [175]. Sub pixel accuracy was achieved in DIC measurements by interpolating pixel intensity values within each subset [174]. Greater accuracy can be achieved by increasing the order of the interpolation functions used [151] with cubic B-splines and quintic B-splines providing the best balance between computational speed and accuracy.
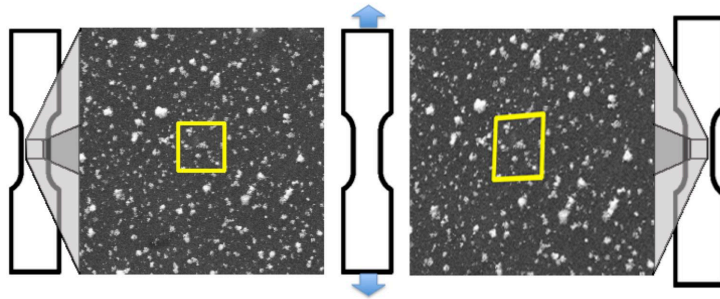
Figure 1.4: Schematic illustrating the DIC process. A reference image is first captured of the unloaded specimen as represented by the dogbone at the left. Images are captured as the specimen is deformed. DIC correlates the deformed and reference patterns in small subsets represented by the boxed area.

1.3.2   Scanning Electron Microscopy - Digital Image Correlation

Recently, digital image correlation has been combined with scanning electron microscopy to enable experimental investigations with nanometer spatial resolution. The first paper utilizing SEM-DIC was written by Jin et al. [81] where the surface rough-

18

ness was used as a tracking pattern to investigate a microelectromechanical system structure. Surface roughness is not suitable for many experiments, thus numerous techniques have been developed to apply small-scale surface patterns on the length scale of the microstructure. Following the general rule of each speckle covering 3 x 3 pixels, a 100 μm Horizontal Field Width (HFW) captured by a SEM with a 2048 x 1768 pixel resolution requires an average speckle diameter of nominally 150 nm. This speckle size is well below the capabilities of patterning methods commonly used for DIC at larger scales, such as airbrushing and toner powder [172]. SEM-DIC patterning methods that have been investigated in our laboratory and by others include nanoparticle (NP) techniques [12, 13], chemical vapor thin film rearrangement [153], through thin film ablation [177], photolithography [153, 172], electron-beam lithography [109, 191], and patterning of polymeric substrates through the use of a contact lithography method [33].

While surface pattern application is the first challenge that must be addressed, SEM image distortion is also a significant problem that was first studied by Sutton et al [169, 170, 171]. Unlike macroscopic DIC in which optical images can be fed directly into commercial correlation software, SEM-DIC requires careful correction of these distortions, which consist of a time varying drift distortion and a spatial distortion, to achieve accurate measurements. These distortions arise from the rastering and time dependent nature of SEM image capture, the electromagnetic lenses, and the beam deflection coils utilized in a SEM. Due to their complexity, these distortions cannot be corrected by classical parametric distortion models. Other imaging challenges include noise, which reduces the signal to noise ratio of the resulting images and has a detrimental effect on DIC accuracy. One way to reduce noise is through image integration, but care must be taken when doing this, as stress relaxation can result in blurred images.

The small fields of view investigated in SEM-DIC enable the data to be combined

with crystallographic data from EBSD. The resulting combined data enables strain localization and deformation to be related to the underlying microstructure. Details on the EBSD technique can be found in many references (for examples see [118, 152]). DIC experiments combined with EBSD have challenges, but are a valuable means for comparing microstructural deformations directly to the underlying crystallography.

1.3.3 Applications

DIC is a flexible and powerful tool that can be used across a wide range of time and length scales. It can be applied to both high-speed impact and low strain rate experiments. Recently, an IMACON 200 ultra high-speed camera was used at a frame rate of 100,000 frames per second (fps) [135] to analyze an aluminum sample in three-point bending resulting from being impacted using a Hopkinson bar setup. In 2009, DIC in combination with a Cordin 550 ultra high-speed camera was used to study crack propagation in an impact-loaded foam sheet at 200,000 (fps) [95]. DIC was also used to measure full-field strains in split Hopkinson pressure bar tension and compression tests on OFE C10100 copper [60] using a Photron APX RS high-speed camera operating at a frame rate of up to 112,500 fps. Conversely, DIC is easily applied to low strain-rate tests, with many applications and experiments ranging from the examination of strain localization phenomena to the characterization of composites [43, 65, 83, 92, 102, 125, 139]. The DIC technique has no inherent length scale, thus is applicable to experiments covering a broad range of FOVs. As an example of a large-scale DIC investigation, Yoneyama et al. detailed the use of DIC to quantify the deflection of a bridge [201].

Recent work using SEM-DIC has provided substantially more information than possible with traditional methods, such as measuring the offset of fiducial lines on the surface. However, while high-quality examples of the application of SEM-DIC to experimental mechanics exist, few incorporate SEM image distortion corrections. Re-

cent experiments utilizing SEM-DIC include a 2011 study investigating damage mechanisms in porous carbonate under compressive loading [34]. In that work, the material had a small failure strain of 0.0011, yet strain localization was observed by keeping the noise levels sufficiently low through the use of a Field Emission Gun (FEG)-SEM, a large spot size, and long dwell times requiring up to seven minutes for a single image capture. While the SEM images used in that study were not corrected for distortion, displacement measurement uncertainties due to errors in positioning of the electron beam and image noise were examined by calculating the standard deviation from stationary image pairs. Experiments have also been conducted on metallic superalloys, including a 2009 work by Tschopp et al. on René 88DT utilizing a combination of EBSD, SEM, and DIC to relate strain localization directly to the Schmid factor of individual grains [177]. Tschopp et al. demonstrated that no relationship exists between the maximum shear strain and the Schmid factor for that material. However, the authors only examined the shear strain field. Depending on the orientation of the active slip system, dislocation slip can appear as shear strain, axial strain, or transverse strain. In 2012, Walley et al. used SEM-DIC to study the high temperature strain localization behavior of the nickel-based superalloy René 104 [191], and determined quantitative measures of strain localization that concentrated primarily at grain boundaries. While Walley et al. did examine the axial, transverse, and shear strain fields, no correlation was found between Schmid factor and strain localization. However, Walley et al. observed slip steps on the surface in grains with high Schmid factors, indicating that the spatial resolution of the DIC experiment may have been too low to capture slip displacements. As mentioned in subsection 1.2.4, Zhang et al. [202] utilized SEM-DIC to investigate strain localization in a UFG Al-Mg alloy, but did not utilize all of the EBSD data to relate strain to the underlying microstructure. In recent work from our laboratory [94], phase transformation in nickel titanium was studied through the application of SEM-DIC. This investigation yielded numerous

21

new findings including that single grains can accommodate a martensite and austenite phase, and grains can be skipped over in the transformation. These works highlight the advantages and strong capabilities of this emerging approach, and the critical need for its careful development and accurate implementation.

1.4   Organization and Goals

The aim of this thesis can be broadly broken into two parts. The first goal is to further the development of the experimental technique combining scanning electron microscopy and digital image correlation. The second, and primary, goal is to expand our knowledge on the microstructure length scale strain localization, strain rate sensitivity, and deformation mechanisms active in ultrafine-grained aluminum under tensile loading at room and elevated temperatures. This thesis is broken up as follows:

Chapter II provides information on the ultrafine-grained material studied and the experimental equipment utilized in this work. It begins by providing details on the 99.99% pure aluminum studied and the parameters used for its ECAP processing. Sample fabrication and surface preparation is then covered, including the polishing procedure utilized, application of platinum alignment markers, EBSD parameters, and the pre-patterning plasma clean process. The chapter concludes with specifics on the Kammrath and Weiss Tensile/Compression module utilized during tension tests.

Chapter III presents work that has been performed on the development of the SEM-DIC technique. SEM-DIC was in its infancy when this research began in 2009, and thus a significant amount of time went into developing the technique. The chapter begins with an overview of the challenges associated with SEM-DIC, including small scale surface patterning and image distortion. Section 3.1 provides a thorough analysis of all of the nano-scale surface patterning techniques that I utilized or developed. A technique utilizing self-assembly of Gold Nanoparticle (AuNP)s was utilized

in the experiments performed here-in. Chapter 3.2 then details work performed to correct SEM images for distortion. This work was based off the techniques originally developed by Sutton et al [169, 170, 171] and updated to account for stress relaxation. New quantitative measures of distortion are presented to demonstrate the necessity of its characterization. The chapter concludes with a discussion of image noise, and recommends imaging parameters to increase the signal to noise ratio in test micrographs. This chapter should provide the reader with the background necessary to carry out SEM-DIC experiments on their own.

In chapter IV, the SEM-DIC technique is applied to room temperature *in-situ* tension tests carried out on ECAP processed UFG high purity aluminum. The goal of this chapter is to demonstrate the effect that the heterogeneous microstructure has on the strain localization and deformation mechanisms active in the material. Eight different fields of view are investigated at various strain rates and magnifications to probe the strain rate sensitivity and measure strain localization at high spatial resolution. These investigations provide new information relating strain localization to the ECAP processed texture and grain boundary inclination angle. Interesting behavior within banded microstructure, including grain boundary sliding, is also presented. The results demonstrate the importance of these small-scale investigations to further our understanding of these advanced materials.

Chapter V covers strain rate jump tension test experiments performed on ECAP processed UFG high purity aluminum at 200 °C. These are the first experiments in which the microstructural features responsible for strain rate sensitivity are investigated through the use of DIC. Four fields of view are investigated, with strain rates alternating between 2.5 x 10^{-5} s^{-1} and 3 x 10^{-3} s^{-1}. Differences in strain localization at the low versus high strain rate are characterized, as well as differences in the macroscopic strain localization at this elevated temperature compared to room temperature. The results include details on the microstructural features most responsible for strain

rate sensitivity.

Chapter VI provides an overall summary of the findings presented in this thesis. It also gives recommendations for continued development of the SEM-DIC technique and future research in UFG materials.

CHAPTER II

Material, Sample Preparation,

and Experimental Setup

This chapter presents details on the UFG tensile specimen preparation and general test procedure. All tests presented in chapters IV and V were performed on tension specimens processed and prepared as outlined in sections 2.1 and 2.2. A Kammrath and Weiss Tensile/Compression Module, with the addition of a heating element in the elevated temperature experiments, was utilized for all testing. An overview of the test equipment and procedure is outlined in section 2.3, while details specific to each test are presented in chapters IV and V.

2.1 Material

Pure aluminum (99.99%) was purchased as 10 mm diameter x 65 mm long extruded rods from ESPI Metals (Ashland, OR) (see table 2.1 for composition). Prior to ECAP processing, the rods were annealed in air at 773 K for 1 hour [89] to achieve an initial grain size of approximately 500 µm. ECAP processing was conducted using a die with a 90° channel angle and an outer arc of curvature of 20° at the University of Southern California by Jittraporn Wongsa-Ngam under the guidance of Professor Terence G. Langdon. The billets were processed at room temperature through four

ECAP passes following route B_C at a pressing rate of ~7mm/s. Following processing, the rods were labeled to define their orientation in the final ECAP pass as shown in figure 2.1. All of the tension specimens tested in this work came from the same batch of coarse-grain billets purchased from ESPI, and ECAP processed at the same time. Room temperature tension tests discussed in chapter IV were carried out within two months of ECAP processing. Elevated temperature experiments discussed in chapter V were carried out ten months after ECAP processing. Due to the low melting temperature of aluminum, and the large number of non-equilibrium grain boundaries [124, 182], there was concern that the microstructure would recover over this time frame. To address this concern, EBSD was performed on the ten month old samples to confirm that the grain size did not deviate from the as ECAPed microstructure. Additionally, tension tests were performed on the ten month old specimens, to confirm that the mechanical properties matched those of the as-processed specimens.

Impurity	parts per million
Ca	<65
Cu	<10
Mg	2
Mn	1
Si	10
Fe	<10

Table 2.1: Impurity concentrations provided by ESPI metals for the 99.99% pure aluminum billets.

2.2   Test Sample Preparation

Following ECAP processing, flat dogbone-shaped tensile test specimens with gage cross-sections of 2 mm x 1 mm and reduced section lengths of 10 mm shown in figure 2.2 were fabricated by Electric Discharge Machining (EDM) by Cut-Rite EDM in Shelby Township, MI. Specimens were cut with the tensile direction aligned with the ECAP pressing axis. The flat faces of the specimens, on which SEM-DIC was

performed, were oriented parallel to the $x - z$ plane in figure 1.1(a).
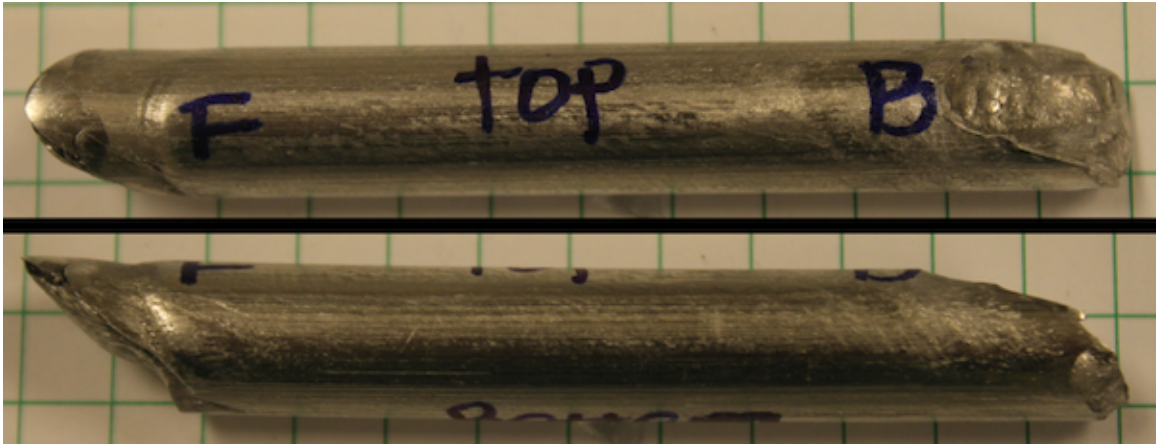
Figure 2.1: ECAP processed pure Al billets labeled to specify the orientation in the final ECAP pass. (Approximate diameter: 10 mm)
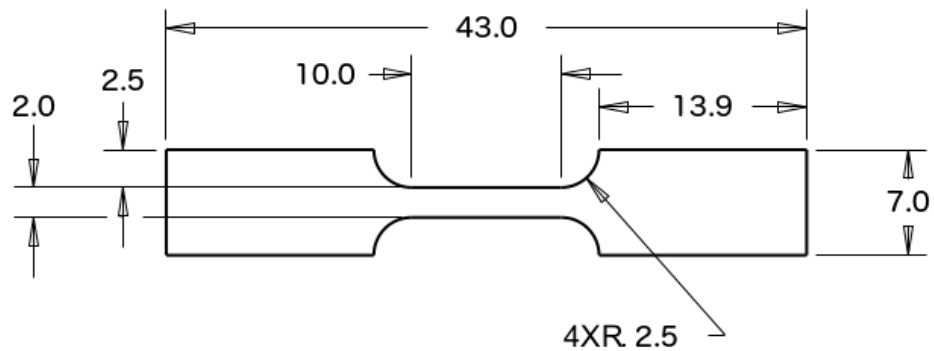
Figure 2.2: Tension specimen dimensions in mm. The original thickness was 1.38 mm, but grinding and polishing reduced the thickness to approximately 1 mm.

Prior to pattern application and testing, the specimens faces were ground and polished, alignment markers were applied, and EBSD was performed. All grinding and polishing was performed using a Buehler Eco-Met 250 grinder/polisher equipped with an Auto-Met 250 power head. Tension specimens were mounted in an epoxy puck with a specimen-shaped cutout as shown in figure 2.3. The specimens were held in place by melting Crystalbond 509 wax into the cutout prior to placing the specimen. The mounting process left the specimen face approximately level with the puck face,

allowing for the use of the automated polishing head and preventing rounding of the specimen edges. Surface preparation began with manual grinding with a base rotation speed of 150 RPM. Grinding was carried out with 320 grit silicon carbide (SiC) papers lubricated with water until the surface roughness caused by EDM was removed. 600 and 800 grit SiC paper were then used to remove the deep scratches that remained on the surface. Polishing followed, utilizing the automated head and an applied force of 10 N, a head speed of 60 RPM, base speed of 150 RPM, and complementary rotation for all diamond polishing steps. Contra rotation was utilized for colloidal silica final polishing. Polishing was started with Buehler MetaDi 9 µm and 3 µm monocrystalline diamond suspension on Mager Scientific Tru-Mol PC-300 cloths. Diamond polishing was finished with Buehler MetaDi Ultra 1 µm polycrystalline diamond paste lubricated with Buehler MetaDi fluid on a Mager Scientific Tru-Mol PC-300 cloth. Final polishing was carried out with Buehler MasterMet 2 Non-Crystallizing Colloidal Silica Suspension on a neoprene-style Mager Scientific Dura Chem PC-740 cloth. Following the final polishing step, the specimens were rinsed with DI water and placed in beakers of acetone. After soaking approximately ten minutes, the specimens were moved to fresh acetone to dissolve the remaining Crystalbond. The freed tension specimens were then transferred to beakers of methanol to remove the remaining acetone and Crystalbond residue. After approximately five minutes in methanol, the specimens were transferred to DI water for a final five minute rinse before being sprayed with a jet of DI water and dried with compressed air. The polished specimens were then stored in air.

Following polishing, platinum markers were applied with a Focused Ion Beam (FIB) to the center of the gage section to align the EBSD and SEM-DIC FOVs. Markers were applied using the FEI Quanta 200 3D SEM equipped with a FIB and Gas Injection System (GIS) in the University of Michigan's Electron Microbeam Analysis Laboratory (EMAL). Platinum markers were applied in a grid pattern in the
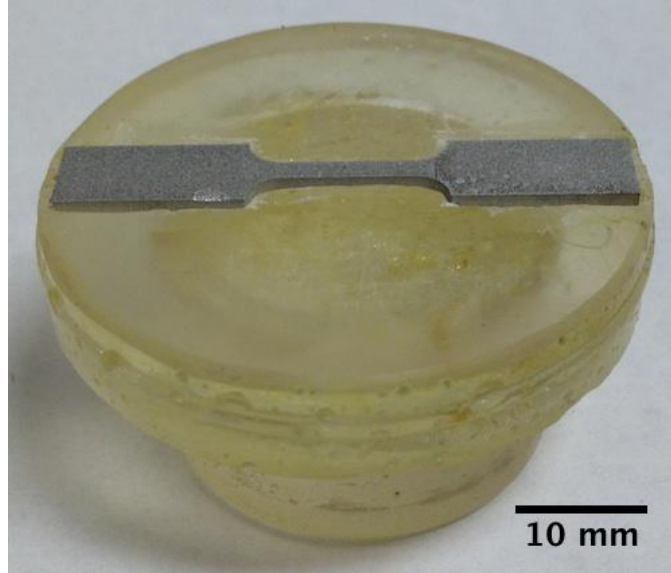
Figure 2.3: Epoxy puck used for polishing tension samples with the automated polishing head.

center of the gage section as shown in figure 2.4, or at the corners of the desired FOV. At least one additional marker as shown in the lower right of figure 2.4 was placed off-center outside of the FOV to denote test specimen orientation. FIB settings ranged from 30 kV accelerating voltage and 10 pA beam current for markers 500 nm in diameter and 500 nm in height to 30 kV accelerating voltage and 0.3 nA beam current for 5 µm x 5 µm x 1 µm markers. If necessary, the marker size can be scaled down to as small as 100 nm in diameter [140].

One can either use Pt markers or Vickers micro-indentations to mark the FOV, as there are advantages and disadvantages to each approach. In a paper by Carroll et al. [24], 25 µm wide Vickers micro-indentations were used instead of Pt markers to designate the FOV. Both methods yield durable and highly visible FOV markers. The Pt markers adhere well to the surface of test specimens and are capable of withstanding light polishing with colloidal silica as well as ultrasonic cleaning. Indentations have the advantage over Pt markers of being more permanent and having sharp corners to assist with alignment, although similar aligning features could be applied with the
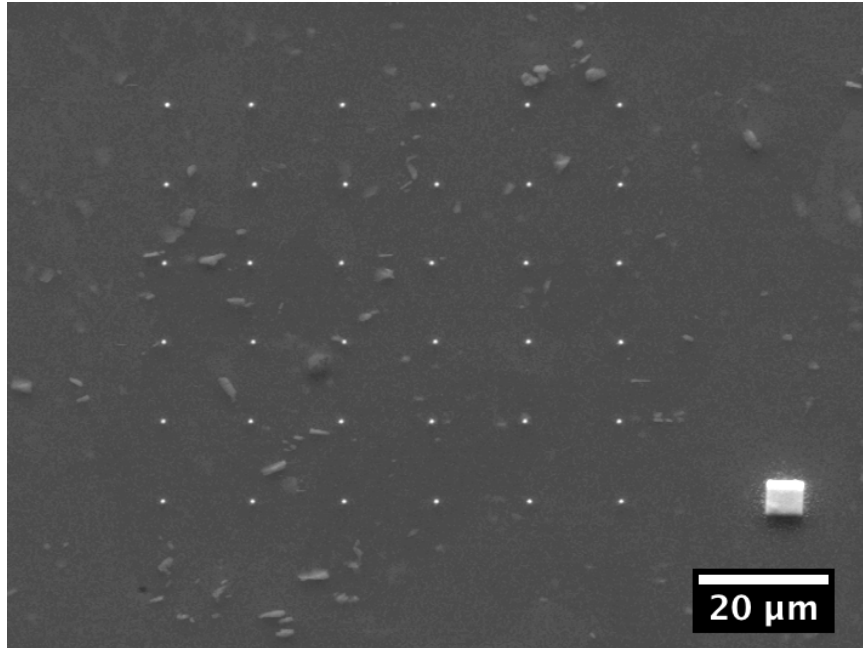
Figure 2.4: Surface of an 1100 Al tensile sample and the FIB deposited Pt markers used for EBSD and test FOV alignment. The large rectangular marker at the lower right is used to find and orient the grid. FIB settings: 30 kV, 10 pA. Marker dimensions: 500 nm diameter x 500 nm in height.

FIB. The main disadvantages of Vickers indentations are their large size and plastic deformation in the test specimen near the markers. Additionally, micro-indentations would not be applicable to thin foil samples, whereas FIB deposited Pt markers have been successfully applied by the authors to 2 µm thick metallic foils.

EBSD was performed on the polished side of the specimens in the Philips XL30 FEG SEM located in EMAL to create an accurate microstructural representation of the test FOV. A 15 kV accelerating voltage, spot size of 5, and 12 mm working distance was utilized for EBSD. A small spot size was utilized to reduce the beam interaction volume and the likelihood of diffraction occurring from two grains. Typical EBSD data collection settings were 4x4 binning, gain of 12.4, black of 39, exposure of 0.05, step size of 100 nm, and image integration of ten frames. These setting allowed for indexing approximately 20 points/second.

Hydrocarbon contamination, common in SEM chambers, caused carbon to be

deposited onto the surface of the tension specimens by the electron beam during the EBSD scan. This carbon layer interferes with patterning and must be removed. Thus, following EBSD, the specimens were cleaned in the Glenn 1000P Plasma Cleaner in the University of Michigan's Lurie Nanofabrication Facility (LNF). The most effective cleaning was realized using the pre-electroplating ashing recipe for which the chamber is pumped to 200 milli-Torr, power is set to 300 W, and oxygen and argon gas are pumped into the chamber at 100 and 12 standard cubic centimeters per minute, respectively. The oxygen-argon plasma generates vacuum ultraviolet energy which breaks the organic bonds between the carbon contamination and the aluminum test specimens [68]. Additionally, the oxygen species that exist in the plasma react with the contamination layer to create CO, CO_2, and other hydrocarbons which can be pumped out of the vacuum chamber. The argon plasma also acts to mechanically break down the contaminants so that they can be evacuated from the chamber. After subjecting the specimens to the plasma for 180 seconds, they were removed and stored in air until patterning through the use of self-assembly of AuNPs as outlined in subsection 3.1.7 and described in [88].

2.3   General Experimental Setup

Tests were performed using an *in-situ* tension-compression stage (Kammrath & Weiss Tension/Compression Module) equipped with a 1 kN load cell and mounted within the FEI Quanta 200 3D FIB/SEM chamber located in EMAL. A labeled photograph of the tension stage is shown in figure 2.5. This is a screw driven stage capable of displacement rates ranging from 0.1 µm/s to 25 µm/s and equipped with a Linear Variable Differential Transformer (LVDT) elongation gage. Deflection occurred between the grips and the LVDT, resulting in inaccurate displacement measurements from the elongation gage. As a result, unless otherwise stated, stress-strain curves and strain values in this text were calculated using the mean axial strain from the

DIC data. The tensile stage was controlled through the Kammrath and Weiss micro-processor control system, referred to as the "Deformation Device Systems" (DDS$_{32}$), or by the DDS$_{32}$ software loaded on the control computer. Following the test, this software allowed for the export of variables including displacement, load, time, and temperature.
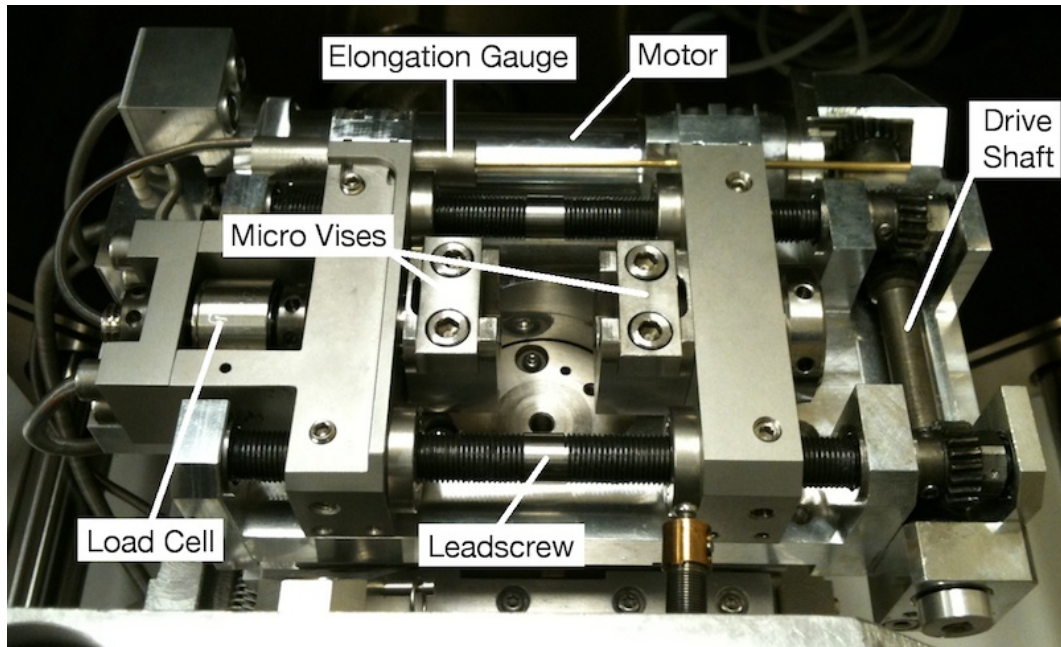
Figure 2.5: Photograph of the Kammrath and Weiss Tensile/Compression Module.

For the elevated temperature experiments presented in chapter V, an 800 °C heating element was attached to the tension specimens as shown in figure 2.6. The heater was attached to the specimen via wire clamps, and contact was made between the heater and back face of the specimen through a graphite pad. Special grips were utilized, which were connected to copper fittings through which chilled water was circulated. Chilled water was also circulated below the heater and was conducted up to the sides of the heating element through the use of copper fins. This cooling was required to prevent heating of the load cell which would both damage it and lead to inaccurate measurements. Specimen temperature was measured by a K-type thermocouple placed between the heater and the specimen, as shown in figure 2.6(b).
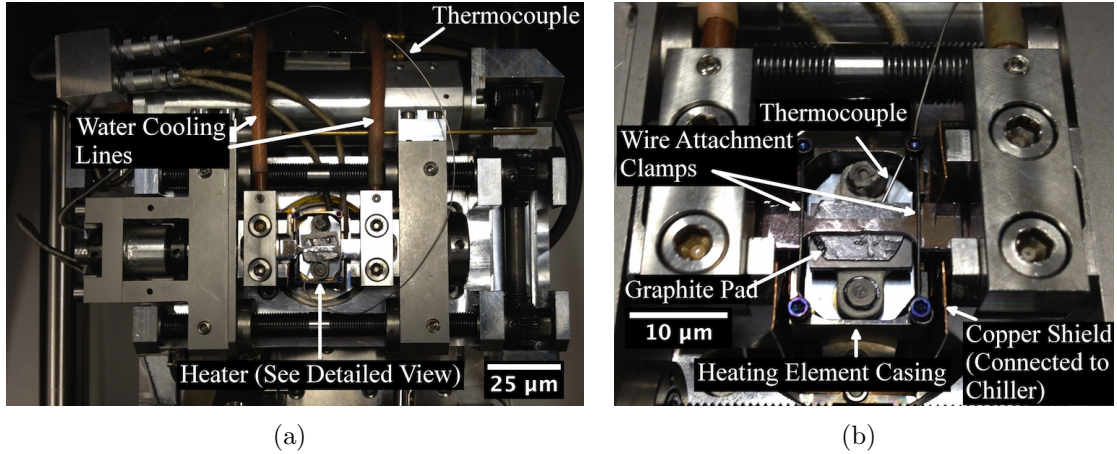
Figure 2.6: Kammrath and Weiss tensile/compression module with 800 °C heater attached. A wide view of the entire tension stage is shown in (a), while a zoomed in view showing the individual components is shown in (b). Chilled water is circulated through the grips and base of the tensile stage to prevent damage to the stage components.

Heating of the tension specimens was controlled by a Proportional Integral Derivative Controller (PID)-controller, controlled through the DDS$_{32}$ controller. Details on PID controllers can be found in [10]. The elevated temperature experiments performed in this work were carried out at 200 °C. To achieve a steady-state temperature, the experimental temperature was set to 200 °C. Through experimentation, the bias was set at a voltage of 6 Volts. The maximum temperature for this bias and the specimen geometry and experimental setup here was slightly over 200 °C. The gain, or proportional part of the PID controller, was increased until oscillations began to appear in the temperature. The gain was then reduced slightly to a final value of 2% °C. The integral value was then adjusted to a value of 100 seconds. This value was determined experimentally to provide quick correction of offsets without significant oscillation. Finally, the derivative term was set to 5 seconds to ensure temperature changes from loading were detected and quickly corrected. These settings enabled the test specimens to reach the 200 °C setpoint in approximately 10 minutes, with a maximum initial overshoot during the temperature ramp-up of 16 °C and a maximum deviation from 200 °C during the tests of +0.86 °C/-1.24 °C.

CHAPTER III

Scanning Electron Microscopy - Digital Image Correlation

Digital Image Correlation has recently been combined with Scanning Electron Microscopy [169, 170, 171], a technique referred to herein as SEM-DIC, to enable full-field displacement and strain mapping at the nano-scale. However, there are numerous challenges that must be addressed before successful application of the technique to nano-scale experimental investigations. This chapter provides details on the challenges that have been encountered and the steps taken to address them.

The first challenge to be addressed is the application of a nano-scale surface tracking pattern consisting of a random, isotropic, and high contrast pattern of speckles [172, 174]. Generating a surface pattern suitable for DIC at the small FOVs that are achievable using SEM is challenging. Subsection 3.1 will address work that has been performed to develop new nanoscale surface patterning techniques. The most successful patterning technique we have developed is self-assembly of AuNPs presented in subsection 3.1.7, which achieves even surface coverage of nanoscale, high-contrast markers on a variety of substrates [88]. This self-assembly technique is capable of creating patterns composed of markers smaller than those produced by all previous techniques.

Image distortion consisting of a time-varying drift distortion and spatial distor-

tion is an additional challenge that must be addressed in SEM-DIC. Drift distortion, discussed in subsection 3.2.3, dominates at high magnifications while spatial distortion, subsection 3.2.5, dominates at low magnifications. Drift distortion can cause magnification-dependent pixel drifts as high as 0.34 pixels/minute at an image resolution of 29 nm/pixel as observed by the authors during the calibration phase of a tensile test on 1100 Al. Magnification dependent spatial distortions as high as 1.6 pixels at an image resolution of 730 nm/pixel can occur, as observed by the authors in a tensile test on pure Al at a global strain of 2%. The distortions can result in largely inaccurate strain and displacement data, and it is critical that they are correctly accounted for when running SEM-DIC experiments. To complicate matters, stress relaxation of the test specimen can interfere with distortion correction and must be accounted for as discussed in subsection 3.2.4. Additionally, SEM imaging parameters must be carefully selected as discussed in section 3.3 to reduce image noise.

3.1 Surface Patterning

All DIC applications require the surface of the test specimen to have a random, isotropic, and high contrast surface pattern ("speckle pattern") as shown in figure 1.3. Pattern application methods used in macro-scale tests, such as airbrushing and sprinkling of toner powder, are not suitable for the small-scale patterning needed for SEM-DIC. The speckles created with these methods allow for a minimum image resolution of approximately 1 µm/pixel (assuming a toner particle size of 8 µm), while SEM-DIC experiments typically require image resolutions in the tens of nanometers/pixel. Note that for an airbrushed pattern, the minimum speckle size is even larger, at approximately 10 µm in diameter. There have been a limited number of papers on the application of small-scale patterns suitable for SEM-DIC [13, 33, 109, 153, 172, 177]. Therefore, a full survey of patterning methods has been performed to determine the benefits and disadvantages of various patterning techniques.

3.1.1 Chemical Vapor Thin Film Rearrangement

Chemical vapor thin film rearrangement was investigated following a method first described by Scrivens et al. in 2007 [153]. In that work, a polished Al substrate that had been sputter coated with a thin gold film was held in water vapor for 9 hours, during which time the gold film rearranged into a high-density dispersion of random nano-scale islands. In an attempt to duplicate this method, a 15 nm thick gold film was evaporated onto the surfaces of polished 2024 Al test specimens using an Enerjet Evaporator in the LNF. The specimens were then held in 95°C water vapor for 9 hours. Although several attempts were made using processing parameters identical to those used by Scrivens et al. and by varying parameters such as film thickness, vapor temperature, substrate material, and specimen surface roughness, repeatability was a significant issue. Small areas of the film broke up into islands as desired, but the islands were non-uniformly dispersed and the majority of the film remained intact. Because of the difficulties obtaining repeatable patterns, this technique was deemed unsuitable for SEM-DIC and other methods were investigated.

3.1.2 Focused Ion Beam Patterning

FIB patterning is a highly repeatable patterning technique capable of generating a desired pattern exactly as it is drawn in the user interface. A FIB milled DIC pattern was previously used by Sabaté et al. [143] in 2007. While this destructive patterning technique would interfere with EBSD and create stress concentrations in tension tests, it was acceptable for Sabaté's work because they were utilizing the pattern to measure stress relief around a milled trench and thus EBSD data was not collected and a load was not applied. In our work, instead of milling the surface, we instead created a random tracking pattern by depositing Pt markers onto the surfaces of a 6061-T6 Al test specimens using a FIB equipped with a GIS. The approximately 20 µm x 40 µm pattern shown in figure 3.1 was created by first drawing an approximately

10 µm x 10 µm random block pattern in the FEI Quanta 200 3D SEM FIB user interface in EMAL and translating and rotating this block to tile the specimen's surface. One shortcoming of FIB patterning is the surface damage that results from Ga+ ion implantation, which can be avoided by using the electron beam instead of the ion beam for deposition. However, using the electron beam in place of the ion beam increased processing time by a factor of five in the tungsten filament SEM used for these experiments. FIB patterning is also expensive and time consuming, taking nominally twenty minutes to generate the 10 µm x 10 µm pattern. Additionally, FIB deposition is only capable of creating feature sizes down to 100 nm in width, which is only suitable for HFWs down to nominally 35 µms. Generating a FIB pattern to cover a 35 µm x 35 µm FOV with the SEM would take approximately four hours and require continuous user interaction on most FIBs. Although the FIB is not time efficient when a pattern is required over an entire FOV, it has potential for tests requiring only a very small area of the FOV to be speckle patterned, such as when measuring strain localization around a specific microstructural feature. In these cases, FIB patterning would be capable of generating a suitable DIC pattern on a wide variety of conducting substrates.
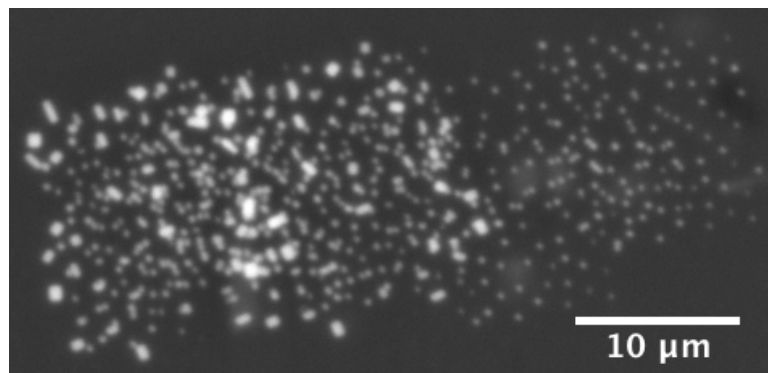
Figure 3.1: Pt speckles deposited by focused ion beam onto a 6061-T6 aluminum substrate. The pattern is highly repeatable and customizable, but expensive, time consuming, and only valid down to fields of view of approximately 35 µm x 35 µm.

3.1.3 Template Patterning

Evaporating metal through Transmission Electron Microscope (TEM) grids has been successfully used to apply a regular grid pattern to the surface of a test specimen for deformation tracking [16, 17, 25, 80]. In an effort to use a similar technique to generate a random pattern, alumina and polycarbonate filter membranes were used as templates for the evaporation of Au onto Al substrates. The alumina filters utilized were 13 mm diameter, 65 μm thick Whatman Anopore membrane filters with 100 nm and 200 nm diameter pores. The polycarbonate filters were 13 mm and 25 mm diameter, 6 – 10 μm thick SPI-Pore polycarbonate membrane filters with 0.1 μm, 0.4 μm, and 2 μm diameter pores. The first step of the patterning procedure was to apply a droplet of isopropyl alcohol (IPA) to the face of the test specimen and place the filter on top of this drop. As the IPA evaporated, the membrane was pulled to the surface, creating an even contact between the membrane and the specimen surface without any wrinkling or curling of the membrane edges. The membrane edges were then secured to the specimen with 3M polyimide film tape. With the filter membrane securely attached to the specimen surface, 5 nm of Cr followed by 50 nm of Au was evaporated onto the surface using an Enerjet Evaporator. Dome rotation in the evaporator was turned off to promote metal flow through the filter pores. Cr was deposited first because it bonds well with oxygen and remains metallic in the vacuum chamber. Thus Au, which forms strong bonds with metals but weak bonds with oxygen, adheres better on oxidized or hydroxide substrate surfaces following a Cr adhesion layer [52, 97].

The ability to generate a pattern with the filters was strongly affected by the ratio of filter thickness to pore diameter, where high filter thickness to pore diameter ratios resulted in poor or failed patterns. Additionally, any gap between the filter and the substrate resulted in a hazy speckle or no speckle at all. SEM imaging of the template patterned specimen revealed that the alumina filter did not yield a pattern, which

can be attributed to the large filter thickness to pore diameter ratios of 325:1 (200 nm pore filter) and 650:1 (100 nm pore filter). The polycarbonate filters have a lower filter thickness to pore diameter ratio of 5:1 (2 µm pore filter), 25:1 (0.4 µm pore filter), and 60:1 (0.1 µm pore filter). SEM observations revealed that the metal was able to flow through only the 0.4 and 2 µm filters to the surface of the test specimen as shown in figure 3.2(a) and 3.2(b). The pattern created with these stock filters was not dense and would require numerous applications to achieve the necessary speckle density. Figure 3.2(c) demonstrates the pattern that resulted from a 2 µm pore filter when it was not affixed tightly to the specimen surface. If filter pore density can be improved, this method shows promise for larger FOV tests. This is an inexpensive patterning method, with polycarbonate filters costing approximately $.65 apiece.

| (a) | (b) | (c) |
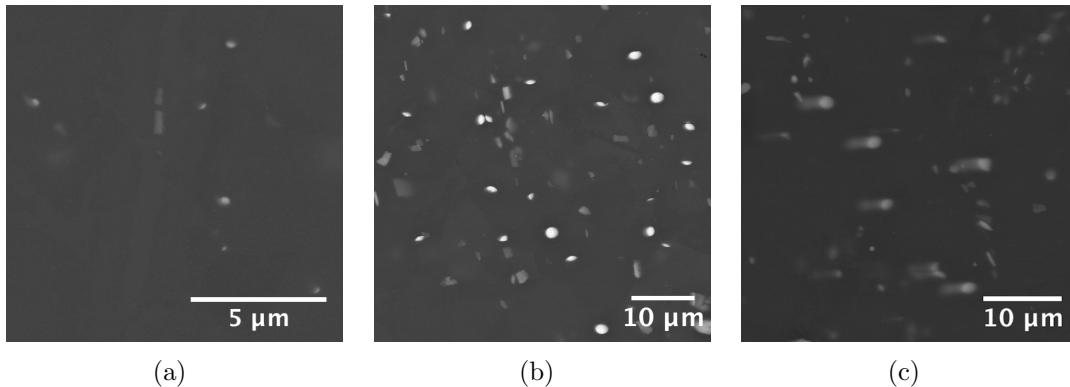
Figure 3.2: Cr-Au pattern evaporated onto an Al specimen through a polycarbonate filter with (a) 0.4 µm pores and (b) 2 µm pores. If the filter is not securely attached to the substrate, hazy speckles like those shown in (c) for a 2 µm pore filter will result. This patterning technique is dependent on the filter thickness to pore diameter ratio. Patterns were only achieved when this ratio was 25:1 or less.

3.1.4 Electron Beam Lithography Patterning

Surface patterning with electron-beam (e-beam) lithography, a well-known process for prototyping integrated circuits and photo-masks [59, 121], was investigated due to the precise control over the pattern that this technique allows. E-beam lithography is capable of generating consistently high quality patterns suitable for tests with

image resolutions as fine as 8 nm/pixel. A pattern exposure is typically limited to a 100 µm x 100 µm writefield, however larger patterns can be generated by stitching pattern areas together in multiple exposures. E-beam lithography is also capable of generating patterns appropriate for high temperature tests by evaporating high temperature materials such as alumina onto the substrate. The disadvantages of e-beam lithography are its high cost, and its limited applicability to non-flat substrates due to the method's sensitivity to working distance. Additionally, while the time to expose the pattern in the e-beam system may be as short as an hour, the time from the start of specimen preparation (spin coating the resist) to end (lifting it off to reveal the pattern) can take over a day and requires significant user interaction.

In this work, e-beam lithography was performed with a Raith-150 e-beam system in the LNF. To use e-beam lithography to create a small-scale DIC pattern, a surface speckle pattern was first drawn in the Raith software's computer aided design (CAD) editor (Version 3.0 SP 9). This pattern contained rectangles of varying aspect ratios distributed in a random and isotropic manner, as shown in the resulting surface pattern in figure 3.3. The pattern can be readily scaled up or down to accommodate DIC at various magnifications.

The e-beam lithography process consists of spin-coating resist onto the prepared substrate surface, exposing the resist with the electron beam, developing the pattern to remove the exposed resist, depositing the desired pattern material, and finally, removing the remaining resist. In this work, a thin layer of polymethyl methacrylate (MicroChem 950 PMMA A2) resist was spin-coated on the substrate surface at 2000 rpm for 30 seconds. These spin coating settings yielded a resist film thickness of approximately 100 nm. The resist was then pre-baked on a hotplate at 180°C for 60 seconds. Using the Raith 150, the pattern was exposed into the resist layer utilizing a working distance of 7 mm, an accelerating voltage of 20 kV, beam current of 0.3 nA, and 30 µm aperture. In addition to the pattern, a large marking feature was drawn
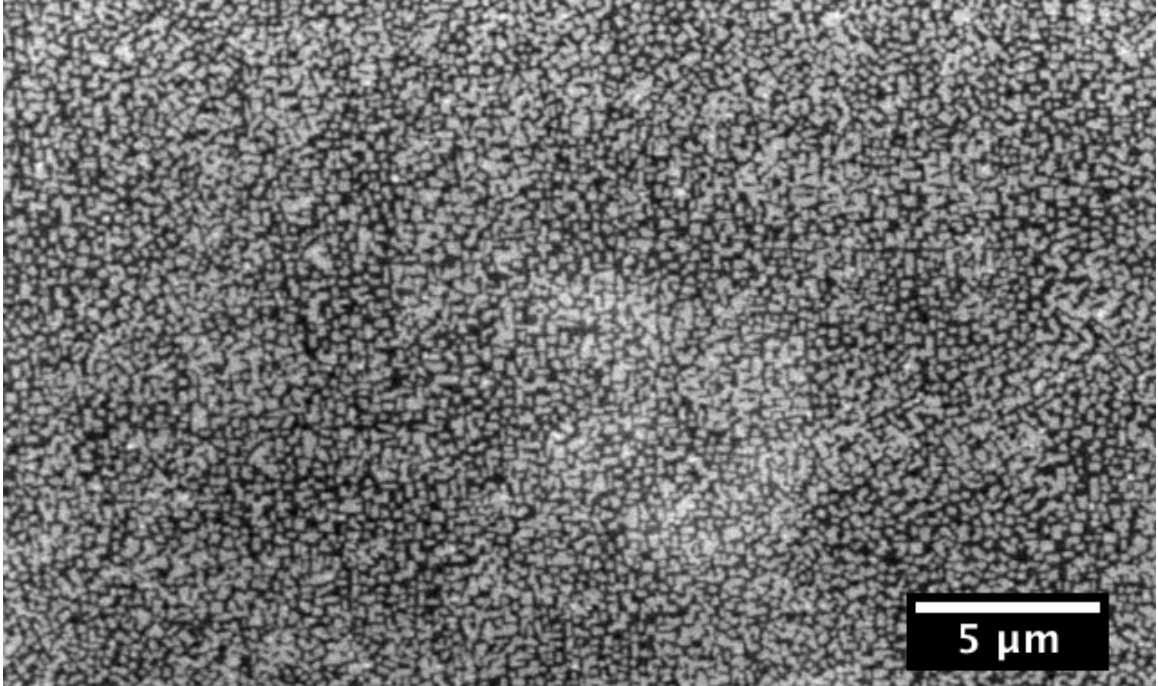
Figure 3.3: Electron-beam lithography pattern on a high-purity (99.99%) aluminum substrate. The pattern consists of a 5 nm thick chromium adhesion layer and 25 nm thick gold layer and contains speckles ranging in size from 200 nm to 1 µm.

next to the speckle pattern to assist in locating the patterned area during SEM imaging. During the exposure process, the PMMA at the speckle pattern locations came into direct contact with the e-beam and was broken up into fragments that could be easily dissolved by developer. Following exposure, the PMMA was developed in a solution of methyl isobutyl ketone (MIBK) and IPA (proportions of 1:3 by volume respectively) for 30 seconds. The developing process dissolved the exposed areas of PMMA, leaving behind bare substrate. The developed pattern was then rinsed with IPA for 60 seconds to stop the development process, rinsed with DI water for 2 minutes, and dried with nitrogen. Using the Enerjet Evaporator in the LNF, a 5 nm adhesion layer of Cr was then evaporated onto the specimen, followed by 15 nm of Au. The PMMA film was then removed by holding the specimen in acetone, leaving behind only the Cr/Au layer that was deposited on the specimen surface. The specimen can be placed in an ultrasonic cleaner to expedite the lift-off process.

Successful exposure of a pattern using e-beam lithography requires establishing an accurate measurement of the working distance between the e-beam and substrate in the patterning region. A change in the surface height between the focusing feature and the pattern area as small as 10 µm has resulted in a failed exposure. To ensure proper focus, a feature(s) used for focusing should be located as close to the desired pattern area as possible. In our work, nickel nano-beads applied with a small foam-tipped applicator, or FIB deposited Pt markers, were used as focusing features. As added security, multiple focusing features surrounding the desired pattern area were used so that an average working distance could be calculated for pattern exposure.

Determination of the appropriate e-beam dose is also critical, and a dose test as shown in figure 3.4 should be performed before attempting to expose a speckle pattern for DIC. The thickness of the PMMA layer determines the dose of the e-beam, with thicker layers requiring a higher e-beam dose to expose the PMMA layer down to the substrate. If the layer is too thin, material evaporated onto the developed PMMA may form a continuous film instead of discrete disconnects at the speckle pattern features. Here, a film thickness of 100 nm allowed for a dose of 275 µC/cm^2 at 20 kV and ensured that a 15 nm Au layer evaporated onto the exposed area was discontinuous at the pattern features.

3.1.5   Drop-Cast Nanoparticle Patterning

This subsection and subsection 3.1.7 discuss surface patterning with AuNPs. Drop-cast AuNPs, discussed here, adhere well to most substrates, allow for control over the pattern feature size, and have good contrast when imaged with the secondary or backscatter electron detectors as shown in figure 3.5, making them promising patterning candidates for SEM-DIC experiments. Drop-cast AuNP patterning is a simple means of creating a suitable tracking pattern for SEM-DIC experiments with image resolutions as fine as 100 nm/pixel. It is cost effective, costing only $56/20 mL from
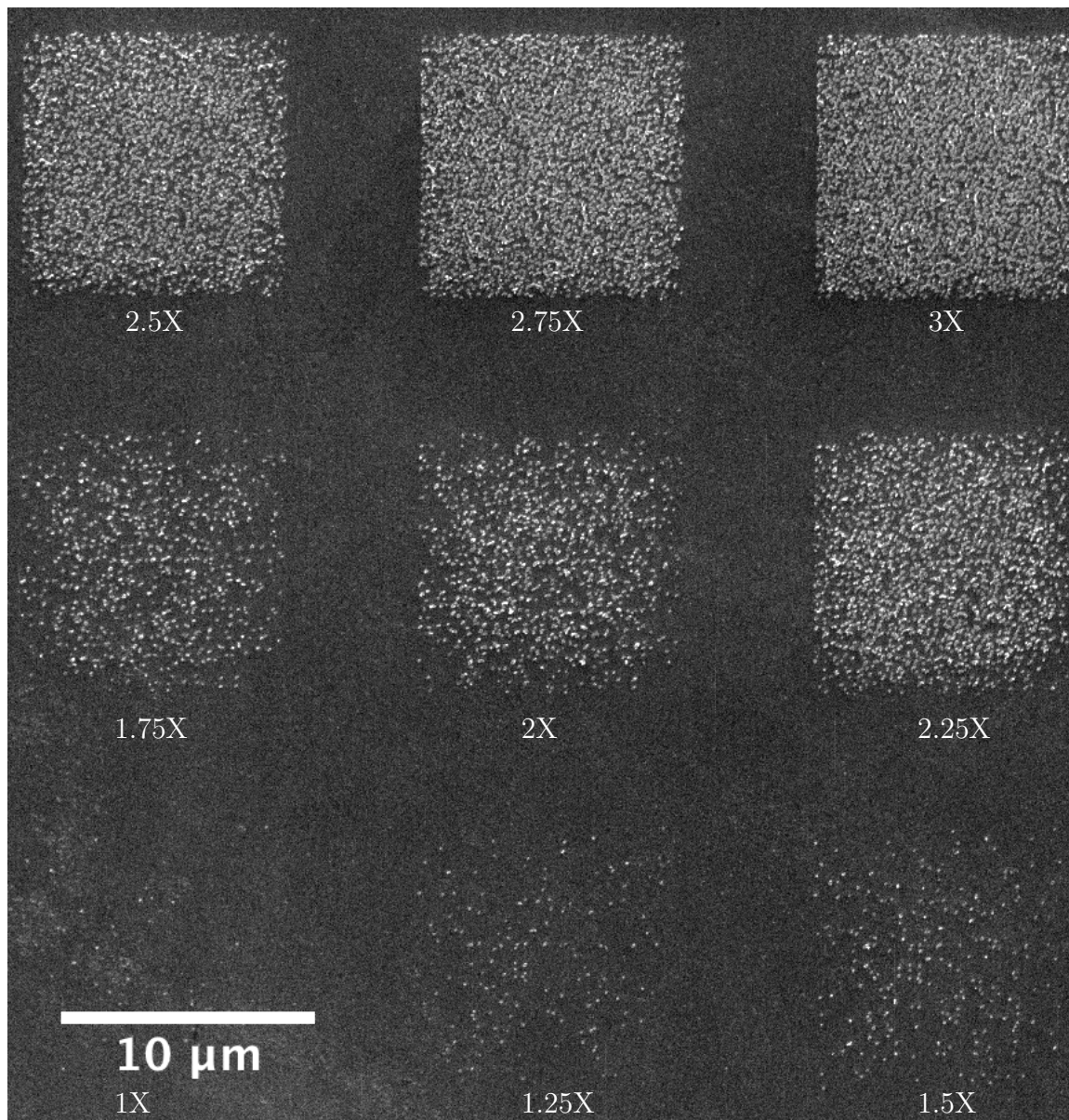
Figure 3.4: 10 µm x 10 µm Au speckle patterns on a 6061-T6 Al substrate exposed at several e-beam dose levels (base dose was 100 µC cm⁻²). A dose of 2.75X provides the best result, as it fills the entire pattern area and does not result in over-exposure.

Ted Pella, or under $1/20 mL for particles synthesized using the procedure outlined by Frens [54]. Drop-casting is a fast patterning process and yields a pattern containing a broad distribution of speckle sizes in minutes. The largest shortcomings with this method are the difficulty in preventing large agglomerates and in controlling pattern location. These shortcomings have been addressed with self-assembly of AuNPs and will be discussed in the subsection 3.1.7.
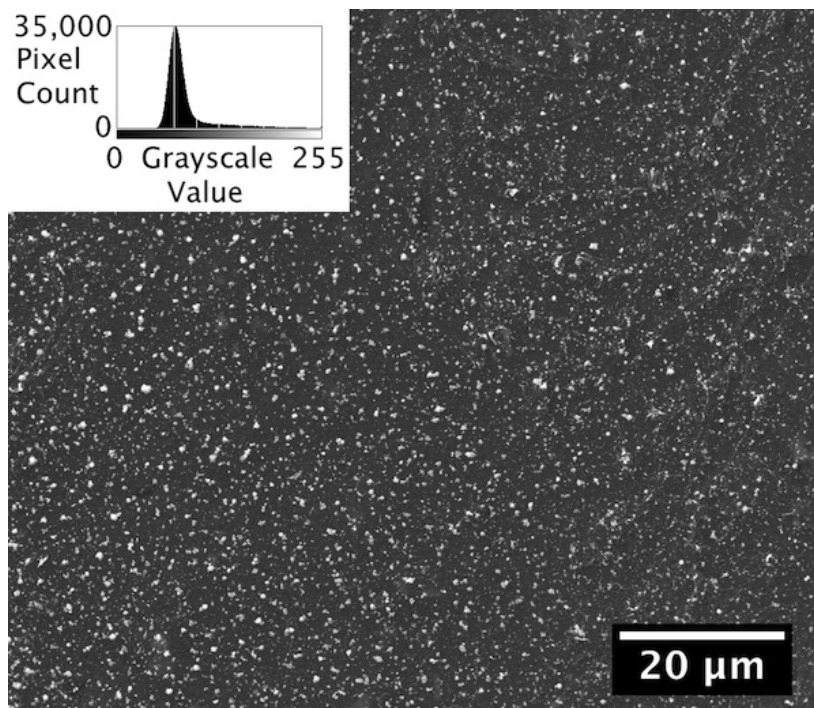
Figure 3.5: DIC appropriate 100 µm HFW SEM image of a 100 nm diameter AuNP drop-cast pattern on a polished 6061-T6 Al specimen. The histogram in the top left shows the distribution of grayscale values over all of the image pixels. Drop-cast AuNP patterning is fast and inexpensive, but substrate dependent and lacks some repeatability in pattern location.

AuNPs purchased from Ted Pella and synthesized in our lab were utilized in this work. Ted Pella purchased AuNPs in diameters of 2 – 250 nm have a net negative charge and are suspended in DI water. AuNPs were synthesized following the procedure outlined by Frens [54], yielding citrate stabilized AuNPs of approximately 13 – 150 nm diameter. Gold (III) chloride trihydrate ($HAuCl_4 \cdot 3H_2O$) and trisodium

citrate dihydrate ($C_6H_5Na_3O_7 \cdot 2H_2O$) purchased from Sigma Aldrich were used to make stock solutions of 10 mM $HAuCl_4$ and 38.8 mM Na_3-citrate. To synthesize the AuNPs, 100 mL of 1mM $HAuCl_4$ (diluted from 10mM stock solution) was added to a beaker and brought to a boil while stirred with a magnetic stirring rod. Between 1.3 mL and 10 mL of 38.8 mM Na_3-citrate was then added to the boiling solution to produce AuNPs with various diameters, as measured with TEM and SEM. After synthesis, the AuNPs were stored in dark glass bottles until use to protect them from UV rays that would reduce any remaining $HAuCl_4$. Details on AuNP synthesis are provided in appendix A.

The first step when utilizing Ted Pella purchased AuNPs was to concentrate them by allowing them to precipitate out of solution or by evaporating the solvent in which they were suspended. Utilizing these methods, AuNPs were concentrated to up to 28x the stock concentration supplied by Ted Pella. The optimal method of AuNP solution concentration depends on the particle size; AuNPs 200 nm in diameter and greater naturally precipitate out of the solution in hours, while AuNPs near 100 nm in diameter can take days. Spinning the solution in a centrifuge to force the AuNPs to precipitate is another method that could be used, but was not investigated in this work. After precipitation, a dropper or micropipette was used to remove DI water and increase the concentration of the remaining solution. By using this method, 200 nm and 100 nm diameter NPs were concentrated to 28x (1.96×10^{10} NP mL^{-1}) and 12x (6.72×10^{10} NP mL^{-1}) the supplied stock concentrations respectively. AuNPs under 100 nm in diameter do not readily precipitate, and alternative concentration methods must be utilized. Placing the AuNP solution in a desiccant chamber successfully evaporated the DI water, but unfortunately also concentrated any stabilizing agents or trace chemicals. These chemicals appeared as dendrite formations in the resulting pattern, as shown in the SEM micrograph in figure 3.6(a). Rinsing the specimen with DI water successfully removed the dendrites without removing AuNPs, as shown in

figure 3.6(b). However, the effect of the presence of these concentrated chemicals on the clumping of the AuNPs has not been determined. Concentration of lab synthesized AuNPs is not necessary as the concentration can be controlled during synthesis.
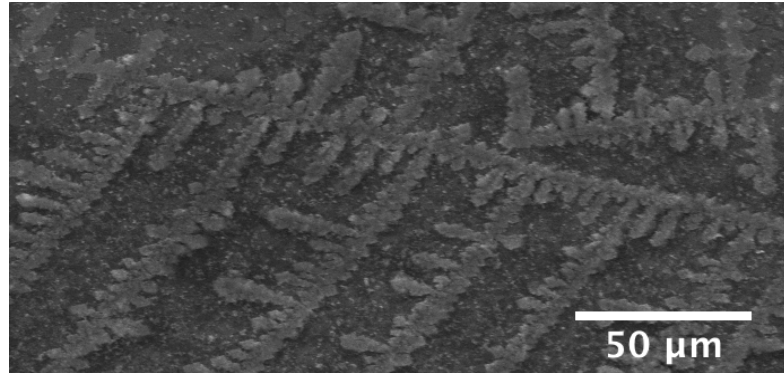
(a)
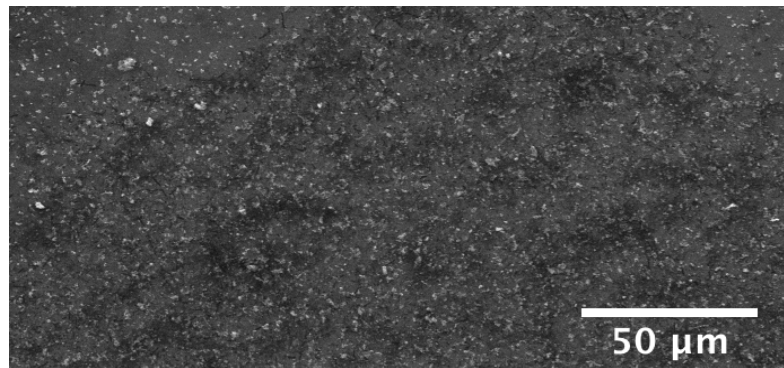
(b)

Figure 3.6: A high concentration of stabilizing agents results in dendrites in patterns created by drop-casting AuNPs that were concentrated by evaporating the DI water in which they are suspended. (a) Dendrites visible on the surface of a 99.99% pure Al test specimen after applying concentrated 50 nm AuNPs. (b) The same area of the specimen after being rinsed in DI water to remove the dendrites. Dendrites need to be removed as they reduce the pattern contrast and darken over time which can interfere with image correlation.

When the AuNP solution was allowed to sit undisturbed, AuNPs often aggregated into large clumps that needed to be broken up prior to application. To break up agglomerates, the AuNP solution was held in an ultrasonic cleaner for a minimum of 15 minutes immediately prior to drop casting. In addition to breaking up agglomerates, ultrasonic agitation also promoted a uniform particle dispersion in the solution.

Faster drying of the AuNP droplet greatly increased the quality of the speckle pattern, and numerous techniques (heating, angling the specimen, spin-coating, and layering) were investigated to decrease drying time. Long drying times provided the AuNPs with time to re-agglomerate, resulting in a non-homogeneous dispersion with the majority of AuNPs settled at the contact line of the evaporating droplet, a phenomenon known as the coffee ring effect. Ring formation is attributed to capillary fluid flow within the drying droplet carrying solute such as AuNPs to the contact line, which itself is pinned to the substrate. Higher concentrations of solute result in wider rings [37]. Heating was investigated as a means to increase pattern quality, wherein a AuNP droplet on a pure Al specimen was heated on a hotplate (model Corning PC-420D). However, heating the specimen to temperatures that promoted faster drying resulted in an increase in ring formation. Angling the specimen as the AuNP solution dried assisted in controlling the final pattern location upon evaporation, but also resulted in large agglomerates preferentially depositing at the lower-lying edge of the droplet. Spin-coating AuNPs onto the specimen reduced the coffee ring effect, with the resulting pattern appearing similar to the pattern observed in the center of a drop cast AuNP pattern but covering a larger area. Depositing carbon over a AuNP layer using an SPI Module Carbon Coater and a 2 mm diameter carbon fiber held the first layer in place and allowed a second AuNP droplet to better wet the surface of the specimen, resulting in a thinner droplet and faster drying. However, the carbon layer broke up following application of the second droplet, forming areas with a dense distribution of particles separated by regions of substrate with a very diffuse covering of particles as shown in figure 3.7. While numerous techniques for drop-cast AuNP patterning were investigated, the authors had the most success drop-casting a small AuNP droplet onto the surface of the polished Al test specimen with a micropipette or dropper and allowing it to air-dry while covered with a TEM grid mesh to prevent contamination from dust.

47
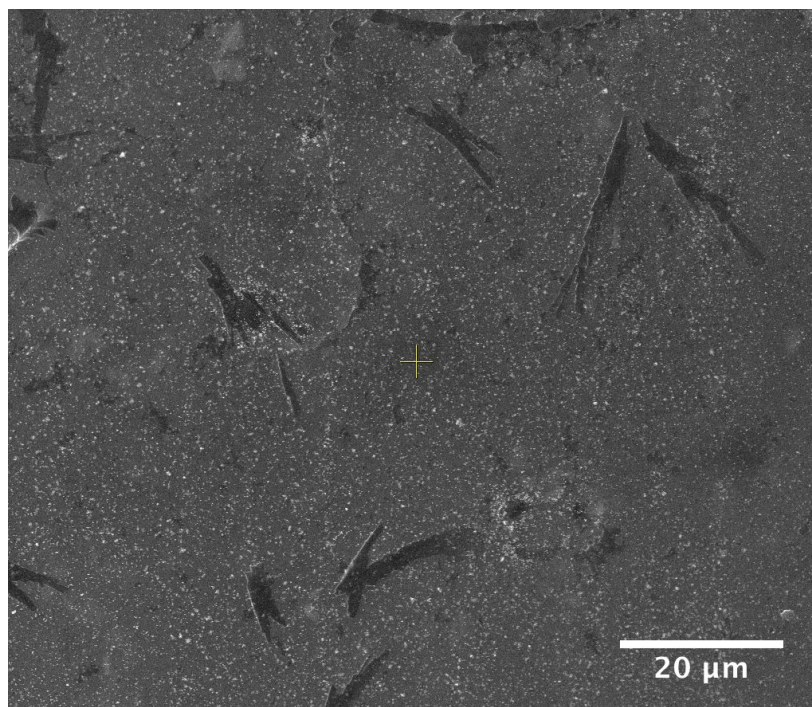
Figure 3.7: Two drop cast layers of AuNPs applied to a 99.99% Al specimen. A carbon layer sputtered from a 2 mm diameter carbon fiber was applied between AuNP layers to hold the first layer in place and speed drying of the top layer. The dark lines are cracks in the carbon layer that occurred after the second AuNP droplet was applied.

AuNP patterning is highly dependent on the substrate surface energy, with better patterns being achieved on substrates with a high surface energy. A droplet of AuNPs applied to a surface with high surface energy had a small contact angle and dried quickly relative to a droplet applied to a low surface energy surface, which had a large contact angle. For pure Al and its alloys, a barrier oxide film with a thickness of approximately 1 nm forms immediately upon exposure of the polished surface to air [36]. The initial surface energy of this oxide film is high, and an AuNP droplet wets the surface in a thin layer that dries quickly from the outer edge to the center. Drying in this manner reduces the amount of clumping observed in the AuNPs and evenly distributed them in the center of the droplet resulting in a good DIC pattern. Over time, the oxide layer adsorbs polar water molecules from the atmosphere, which results

in a drop in the surface energy (by as much as 75% for θ-alumina) [113, 149, 200]. With the drop in surface energy, the contact angle between the Al substrate and the AuNP droplet increases, which results in longer drying times. Also, instead of drying from the edge of the drop to the center, the droplet now dries to a thin layer before the meniscus breaks, at which point the remaining fluid dries at the edge of the original droplet. Following this drying scheme, a large ring of AuNPs accumulates at the edge of the droplet and few AuNPs are observed in the droplet center. It is therefore suggested that all test specimens be stored with desiccant to slow the adsorption of water at the oxide surface and prevent heterogeneous dispersion. On Al specimens with low surface energy, some success was achieved using the tip of a plastic dropper or micropipette to drag the edges of the droplet out and decrease the contact angle. This encouraged the droplet to dry in a method similar to that seen on specimens with high surface energies.

3.1.6   EBSD Assisted Drop-Cast Nanoparticle Patterning

In SEM-DIC experiments combined with EBSD, a surface pattern is often desired directly over the EBSD area. In this work, 200 nm diameter AuNPs applied to the specimen surface following an EBSD analysis displayed a preferred arrangement within the EBSD scan area. This preferred arrangement was observed on both pure Al and Al alloys. The surface of a 99.99% pure Al test specimen following EBSD with a beam voltage of 25 kV, an aperture of 3, and spot size of 6 is shown in figure 3.8(a). A hexagonal grid of dark hydrocarbon contamination spots representing the EBSD scan locations is visible on the surface. Immediately after removal of the test specimen from the SEM, 200 nm diameter AuNPs were applied over the EBSD area. Figure 3.8(b) shows the surface of the specimen following the application of the AuNPs, with a random arrangement of AuNP agglomerates visible in the area where no EBSD was performed. In the EBSD affected area, the AuNPs collected in pools shown by the

yellow ovals in figure 3.8(b), in the areas surrounding the hydrocarbon contamination points. The preferred pooling of AuNPs could be exploited to produce patterns in the exact area that the EBSD analysis was performed. Similar results were seen with smaller AuNPs when a smaller EBSD step size was utilized, thus reducing the size of the hydrocarbon contamination spots and the spacing between them.

(a)   (b)
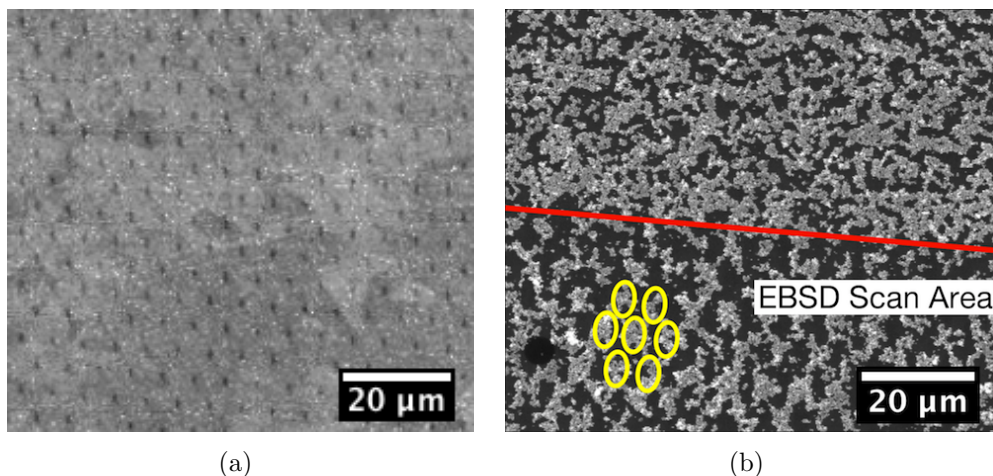
Figure 3.8: (a) Periodic hydrocarbon contamination spot grid pattern visible on a 99.99% pure Al test specimen post EBSD. A 25 kV accelerating voltage and spot size of 6 was used for the EBSD analysis. (b) 200 nm diameter AuNPs preferentially pool between grid points. The area below the line was analyzed by EBSD and shows a preferred arrangement of AuNP agglomerates while the area above the line was not analyzed by EBSD and shows a random distribution of AuNP agglomerates.

In addition to the tendency of AuNPs to order themselves in an EBSD analyzed area, it has been observed that AuNPs do not adhere to an Al surface near the Pt FIB markers, as shown in figure 3.9. The repulsion of AuNPs in the area around the Pt markers occurred regardless of whether the markers were deposited with an electron or ion beam. The area free of AuNPs extended slightly beyond the Pt halo surrounding the markers, but could be reduced by reducing the Pt marker size. The rings surrounding the Pt markers resulted from two phenomena. First, only a partial amount of the Pt gas interacts with the ion beam. An amount of the Pt gas that avoids the ion beam impacts the surface and deposits itself. Second, the ion beam scatters as it approaches the surface and deposits Pt outside of the desired area. The

halo surrounding the Pt markers scaled with the size of the marker, and could be reduced by using smaller Pt markers as shown in figure 3.10.
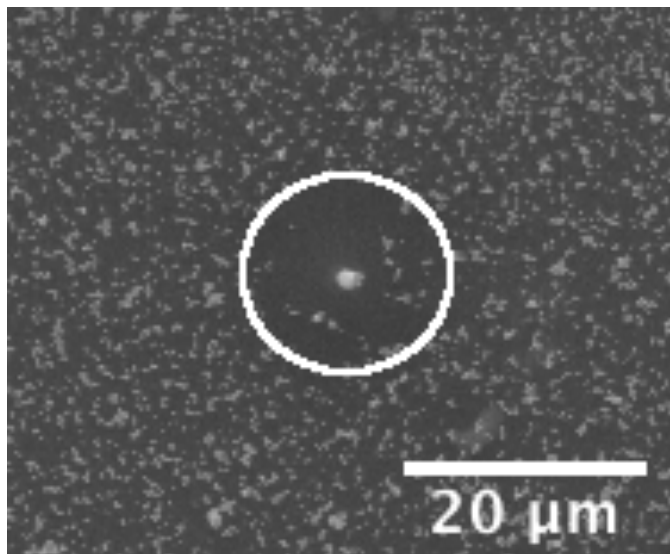
Figure 3.9: Image of an Al substrate with a 1 µm diameter FIB-deposited Pt marker at the center. While the majority of the surface is covered by 200 nm diameter AuNPs, the area around the Pt marker is free of AuNPs. The size of the AuNP free area scales with the marker size.

3.1.7 Self-Assembled Gold Nanoparticle Patterning

Self-assembly of AuNPs yields patterns that cover the entire substrate with features smaller than those produced by any existing technique. Self-assembled AuNP two-dimensional arrays were first investigated in the 1990s as a technique to produce surface-enhanced Raman scattering (SERS) substrates [53, 63, 64]. Here, the technique is adapted for digital image correlation to enable experimental investigations using SEM-DIC at unprecedented length scales. This process is an excellent candidate for the surface patterning required by SEM-DIC experiments, providing dense coverage (as seen in figure 3.11), strong bonding of the AuNPs to the surface, and a controllable feature size. Additionally, it is an inexpensive and fast patterning technique that does not require cleanroom access or specialized lithography equipment.
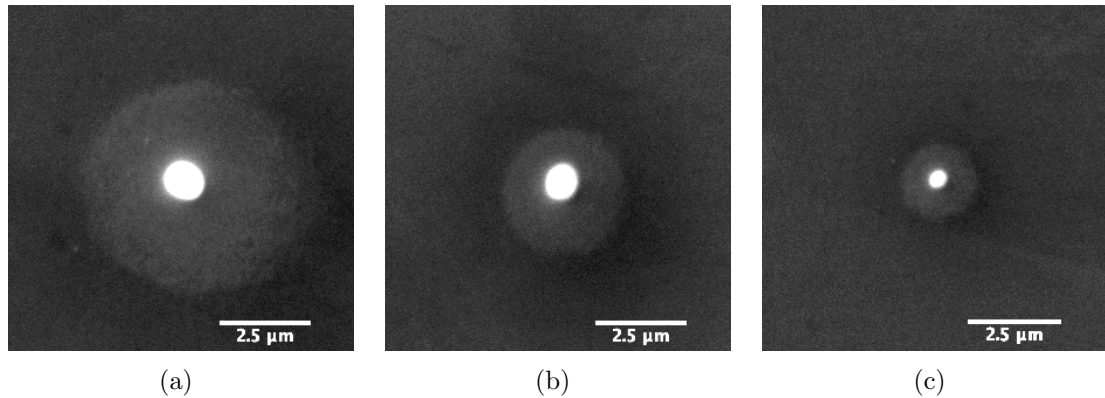
Figure 3.10: Pt markers deposited on the surface of a pure Al specimen. The Pt halo surrounding the markers scales with the marker size. The markers are 1 µm in diameter (a), 800 nm in diameter (b) and 400 nm in diameter (c).

Since the specimens only need to be soaked to achieve the pattern, the patterns can be applied to curved substrates and delicate test specimens. Finally, surface roughness does not appear to affect pattern quality. Dense coverage following the procedures outlined in this article has been achieved on polished aluminum, as well as rolled aluminum and wire EDM cut aluminum surfaces with root-mean-squared (Sq) surface roughness values of 0.38 µm and 3.07 µm respectively (measured with an Olympus LEXT OLS4000 3D Laser Measuring Microscope). In terms of modifying this approach to deposit other materials, successful self-assembly with silver nanoparticles [53, 64, 47] and monolayers of AuNPs with platinum and palladium shells [132] has been achieved. It is probable that a suitable linking molecule could be found to attach other materials, including Ti or Ta, to the surface as well, but the authors are currently unaware of any literature that discusses attaching any colloids other than Au and Ag by using a molecular linkage between the substrate and colloid.

Patterns were created with suspensions of citrate stabilized AuNPs of 13-150 nm diameter produced following the procedure outlined by Frens [54] and detailed in appendix A. The AuNPs attach to the substrate surface by organosilane molecules that possess a pendant functional group with a strong affinity for gold. As discussed in work by Freeman [53] and Grabar [64], when substrates that possess reactive ox-
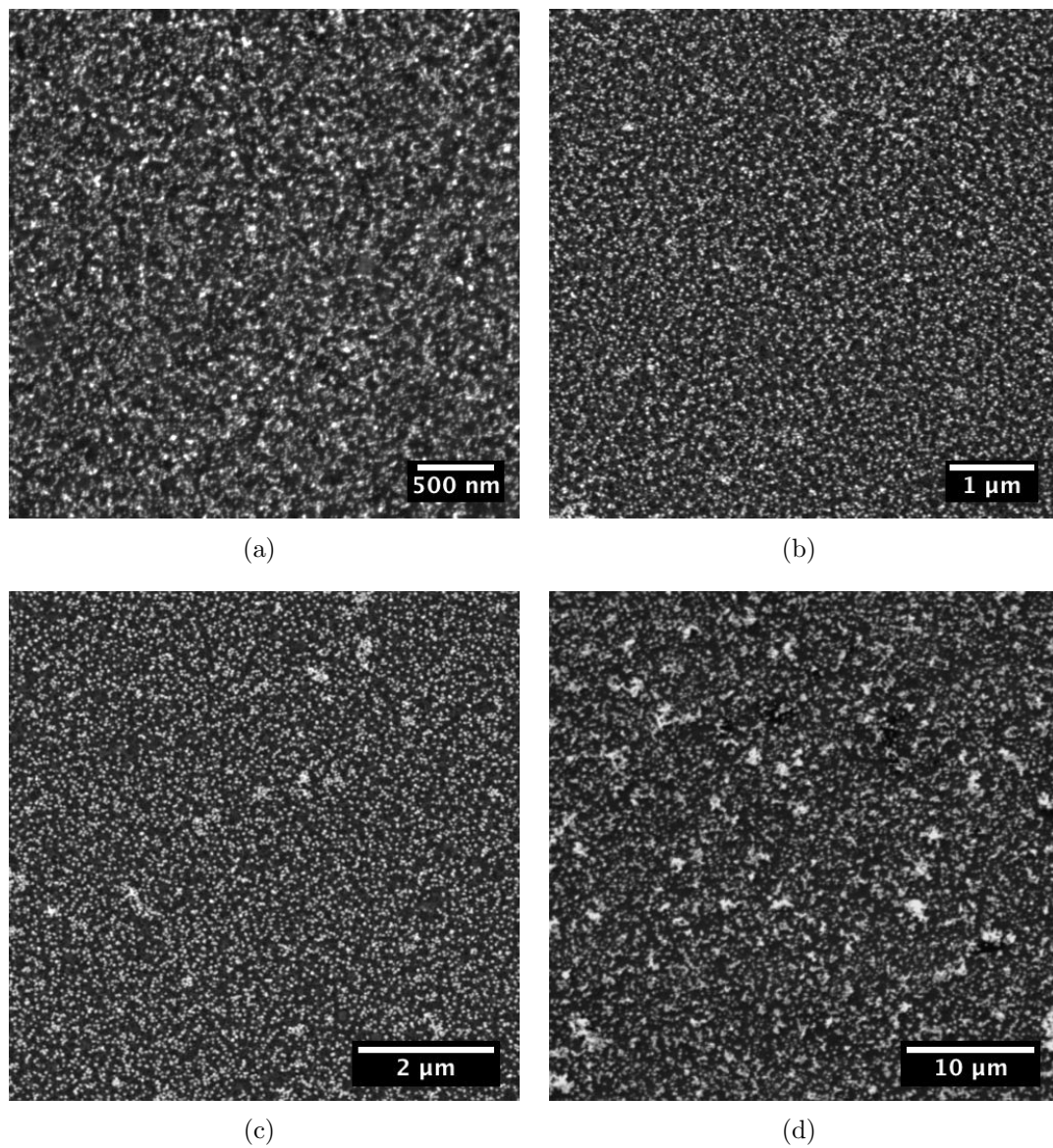
Figure 3.11: AuNPs immobilized with MPMDMS on the surface of a 99.99% Al substrate. The patterns were created by soaking the substrates in (a) 15 nm diameter AuNPs for 5 days, (b) 32 nm diameter AuNPs for 3 days, (c) 48 nm diameter AuNPs for 1 day, and (d) 136 nm diameter AuNPs for 1 day. The histogram at the lower left of each image shows the grayscale distribution of the image.

ide/hydroxyl groups on their surface are immersed in a dilute organosilane solution, the silane molecules covalently bond to the substrate surface. The bound molecules are oriented so that the pendant functional group extends from the substrate surface, causing AuNPs to self-assemble onto the surface upon immersion into the AuNP solution. In this work, the organosilanes (3-aminopropyl)trimethoxysilane (APTMS) and (3-mercaptopropyl)methyl)dimethoxysilane (MPMDMS) (Sigma-Aldrich) were tested. APTMS and MPMDMS yielded similar pattern results and were used interchangeably.

Patterns were tested on substrates of 99.99% aluminum, 1100 aluminum, a nickel-chromium superalloy, and silicon carbide with similar success. Aluminum will be discussed as a model material in order to describe the pattern application process, which was similar for all tested substrates with the exception of differences in mechanical polishing and hydroxylation prior to patterning. The Al specimens utilized for self-assembly of AuNPs were prepared following the procedure outlined in chapter II. Note that the optimal polishing procedure will vary depending on the substrate under consideration, however all substrates should undergo plasma cleaning as outlined in chapter II.

Oxide/hydroxyl groups already exist on the surface of many metals and non-metals, but the number of hydroxyl groups on the substrate surface must be maximized in order to achieve a dense AuNP surface coverage. For glass slides in work by Grabar and Freeman, the surfaces were hydroxylated by soaking them in Piranha solution. There are numerous methods to generate hydroxyl groups on the surface of aluminum. The highest density of hydroxyl groups exist after Al is placed in boiling water to create a thick pseudoboehmite layer [38, 39, 112, 188]. However, this pseudoboehmite layer is not suitable for SEM-DIC experiments as it is very brittle and was found to crack at around 2% strain. The second highest number of hydroxyl groups is created by an alkaline clean treatment that has minimal effect on the thick-

ness of the oxide layer [188]. The resulting high density of hydroxyl groups on the surface enables the formation of strong bonds between the silane Si end group and substrate surface [50, 51, 84, 189]. In this work, Al substrates were alkaline cleaned in a stirred solution of 200mL of DI water containing 4.4 grams each of Na_3PO_4 and Na_2CO_3 (pH of 10) held at 75°C for 60 seconds as outlined in reference [122]. After removal from the cleaner, the substrates were rinsed with DI water and dried with compressed air. This treatment was performed immediately prior to patterning and resulted in a reproducible hydrophilic surface for pattern application.

After hydroxylation, the substrates were silanized by soaking them in vials filled with one part APTMS or MPMDMS to four parts methanol [64] for 24 hours. After this time, the substrates were removed and immediately immersed in a beaker filled with 100mL of methanol. The methanol was stirred with a magnetic stirrer such that it flowed over the surface of the substrates for 30 minutes. The substrates were then transferred to a beaker of fresh methanol and rinsed for an additional 30 minutes. Following the methanol rinse, the substrates were rinsed with DI water and placed into vials that were subsequently filled with AuNPs of the desired diameter. To prevent agglomerates from collecting in the FOVs, the substrates were placed in the vials with the FOVs angled downward.

Darkening of the AuNP solution when added to the substrate vial is an indication that the AuNPs are flocculating, or coming out of suspension. Citrate stabilized AuNPs have a negative surface charge [93] that repels them from each other and prevents aggregation in solution. One potential cause of aggregation could be unbound silane molecules detaching from the substrate surface and bonding to the AuNPs. Once bound to the AuNPs, the silane molecules can neutralize the particle charge [40] and lead to aggregation. Unbound silane molecules can also lead to bridging flocculation [40, 73] where the tails of the silane molecules stick out from the surface of the AuNPs and bind to other AuNPs when they come in contact. If darkening

of the AuNP solution does occur with the addition of the substrate, the substrate should be promptly removed, thoroughly rinsed, and placed into a new vial to which new AuNPs are added. If the new AuNP solution still darkens it could be due to the substrate itself. Electrolytes will neutralize the AuNP surface charge [73] and thus substrates that leach electrolytes into the AuNP solution cannot be patterned with this technique. The same is true for substrates that leach polymer molecules as this will lead to bridging flocculation. In this work, the glue used to attach rubber seals to the lids of the glass vials (Ted Pella prod. #12730) used for patterning caused flocculation, most likely due to bridging flocculation. The authors recommend test patterning a small piece of the substrate material before attempting to pattern an actual test specimen.

The substrates were soaked in the AuNP solution for between one and five days, with larger AuNPs requiring less soaking time in order to achieve a dense surface pattern that would yield accurate DIC results. After soaking for the specified time, the substrates were removed, rinsed with DI water, and placed in a shallow tray filled with DI water. Substrates were allowed to dry after verification by optical microscopy that the surface was not covered by large AuNP aggregates. If large aggregates were observed on the surface, a jet of water was used to remove them before drying. However, small aggregates were allowed to remain on the surface to be used as a tracking pattern for lower spatial resolution investigations over a larger FOV. This is shown in figure 3.12 where 50 nm diameter AuNPs have self assembled onto a 99.99% pure Al substrate. The individual particles result in a pattern suitable for a HFW of 10 µm while the aggregates are suitable for a HFW of to 500 µm.

The AuNPs strongly adhere to the substrate surfaces, which is a necessary condition for accurate displacement measurements using DIC. The strong adhesion arises from hundreds of linkages between each particle and the substrate surface [64]. Strong adhesion was confirmed by placing the patterned substrates in methanol and acetone
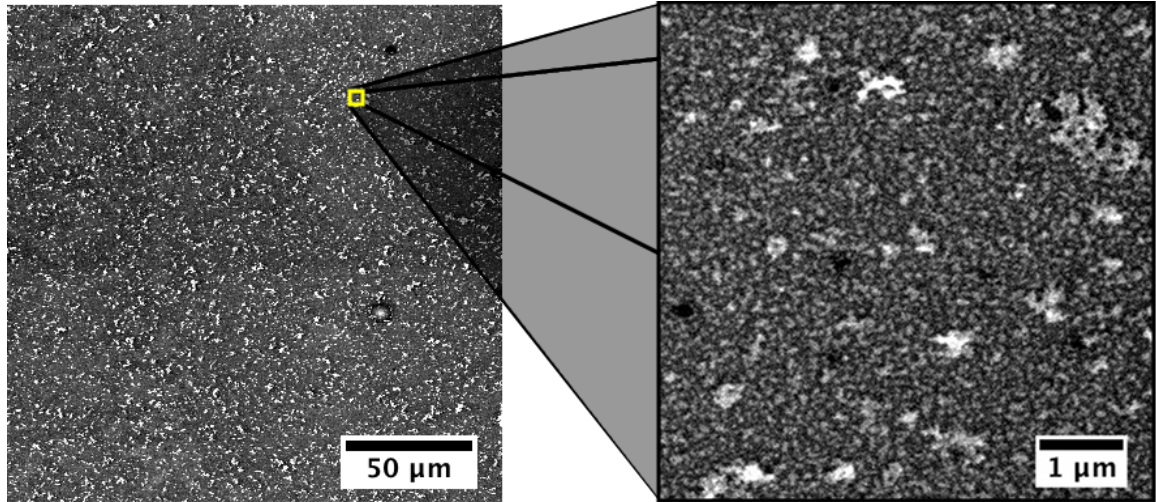
Figure 3.12: Multi-scale self-assembled AuNP pattern on a 99.99% pure Al substrate. By placing the substrate face up in the AuNP solution, small aggregates attached to the surface. This pattern would be suitable for tests utilizing HFWs of 10 µm to 500 µm.

in an ultrasonic cleaner for 30 minutes. No change in the pattern quality was observed. Additionally, tensile tests were performed on specimens patterned with this technique and areas that underwent large surface deformation due to shear bands were observed. Even in areas where these shear bands created ledges in the surface, the relative location of neighboring particles did not indicate particle motion due to the AuNPs becoming detached from the surface.

Often in SEM-DIC experiments, it is necessary to remove the pattern after the test in order to perform EBSD. While AuNP surface patterns (both drop cast and self-assembled) are significantly easier to remove than e-beam lithography patterns following large surface deformation, they are still challenging to remove without affecting the underlying substrate. In this work, AuNPs were removed from the surface with one of the following techniques. The first method utilized gentle polishing with Buehler MasterMet 2 colloidal silica suspension. This suspension is slightly basic and chemo-mechanically polishes the surface. To remove the surface pattern, the polishing suspension was applied to a Mager Scientific Dura-Chem polishing cloth and the sub-

strate was placed face down into the suspension. Using minimal but sufficient force to bring the substrate in contact with the polishing cloth, the substrate was polished in a circular motion for approximately 10 seconds. The substrate was then rinsed and checked in an optical microscope to determine if the AuNPs had been removed. This procedure may need to be repeated multiple times if the surface has deep surface deformation. The second method was to repeat the plasma and alkaline cleaning steps on the deformed specimen. This proved capable of removing the AuNPs from the surface for post-test EBSD and, unlike additional polishing, did not further damage the surface. In contrast, removal of e-beam lithography patterns required polishing with 1 µm diamond suspension prior to polishing with colloidal silica. This removed the specimen surface at a substantially faster rate, which is generally not desirable for deformation studies.

3.2   Distortion Correction

The electromagnetic focusing and scanning systems of a SEM lead to complex image distortions, resulting in inaccurate DIC displacement data if left uncorrected. SEM micrographs suffer from two types of distortion – (1) drift distortion, which varies over time; and (2) spatial distortion, which is similar to the distortion present in optical lenses and can vary from test to test. This section will begin by addressing SEM image distortion utilizing a modified version of a distortion correction framework first developed by Sutton et al. [169, 170, 171]. It has been adapted to correct for the effects of stress relaxation that occurs during the image scan and can be particularly detrimental to drift distortion correction. If stress relaxation is present and the drift distortion corrections do not account for it, it can contaminate the drift correction functions and lead to worse distortions than if the data was left uncorrected. In subsection 3.2.4, two methods for removing stress relaxation from calibration data are presented. The techniques described in this section can be scaled up to larger

FOVs, or down to smaller FOVs, as need dictates.

3.2.1 Pre-Test Calibration Phase

To correct for both spatial and temporal distortions, nominally eighteen micrographs of a speckle-patterned calibration specimen were captured during a pre-test calibration phase [171]. A timer was started when the first image was captured, and the time at which every subsequent image was captured was recorded. The images were captured in pairs, with the specimen remaining stationary within each pair. Between image pairs during this pre-test calibration phase, the specimen was translated a known distance in the horizontal and vertical directions, as shown in figure 3.13. Four horizontal and vertical translations were performed to get an accurate measurement of spatial distortion and minimize the length of the calibration phase. The total x and y translations should be approximately 1/4 of the FOV. For example, in a 200 µm wide image, the total x and y translations would both be 50 µm and would be performed in 12.5 µm steps. Note that diagonal translations can also be made and used as a post-correction check to ensure that the sum of the horizontal and vertical spatial distortion surfaces account for the distortion seen in the diagonal translations. The stationary image pairs taken during pre-test calibration were used to correct for drift distortion, and the orthogonally translated images were used to correct for spatial distortion.

3.2.2 Test Calibration Phase

The duration of SEM-DIC tests can be on the order of several hours to a day, and although spatial distortion remains nominally constant, the drift distortion correction image pairs captured during the pre-test calibration phase may not accurately predict the drift distortion that occurs throughout the test. Thus, stationary calibration image pairs continue to be captured during the test phase. This required that the

chamber remained pumped at vacuum and the source energized following the calibration phase to avoid any effect on drift distortion from drops in chamber pressure or cooling of the source.
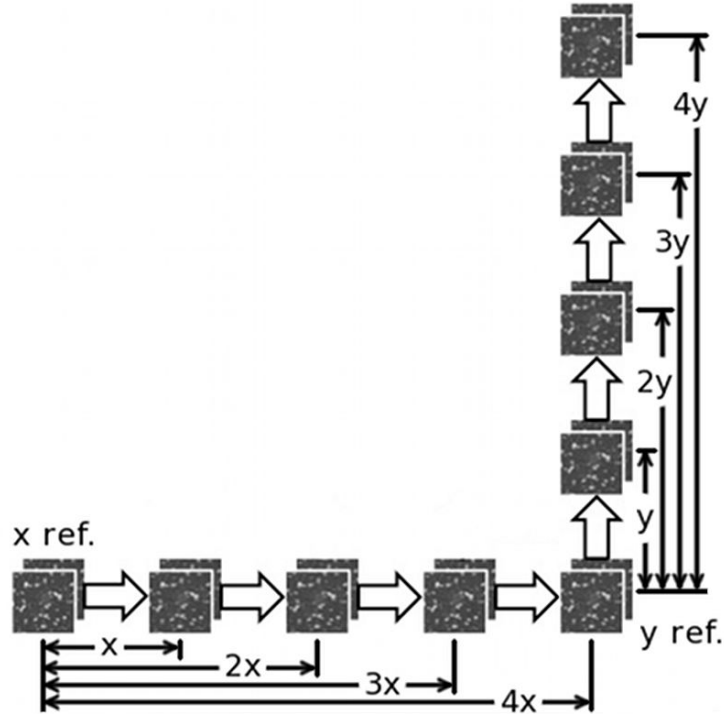
Figure 3.13: Diagram of the translation sequence used for distortion correction. Images are captured in pairs with translations occurring between stationary image pairs. The total x and y translation should be approximately 1/4 of the FOV.

The effects of stress relaxation, if significant, become apparent in test phase calibration images captured of the loaded test specimen surface. One method to remove stress relaxation from the test-phase calibration images, applicable at any image resolution, is through the use of an unloaded pattern (instead of the standard method of using the test specimen pattern). If this is not possible, a relationship between load and relaxation can be determined and used for correction at image resolutions from 30 nm/pixel to 300 nm/pixel (verified in experiments). If stress relaxation is present and is unaccounted for, the distortion-corrected data can actually have a greater amount

of distortion than the uncorrected data. More details on stress relaxation will be discussed in detail in the subsection 3.2.4.

3.2.3 Drift Distortions

Drift distortion (also known as pixel drift) can lead to significant errors over the typical duration of a SEM-DIC experiment. Drift distortion can result from motion of the SEM stage, heating of components in the electron column or the specimen itself, charging of contamination on beam deflectors and apertures, charging of the SEM stage or specimen, and interference from magnetic fields [9, 27, 62, 101, 127, 164]. The first step in drift distortion correction is correlating the stationary image pairs captured during the calibration phase and the test. In this work, image correlation (pre-correction) was performed using a commercial software package [190]. Since the time at which each image was captured was recorded, the DIC displacement fields from these stationary image pairs could be converted into drift velocities. This provided drift velocity measurements throughout the test and at every data point, as shown by the circle data points in figure 3.14. The horizontal and vertical drift velocities at each data point were then plotted versus test time and fit with a polynomial curve (in this work, a quadratic function was used to reduce the effects of noise) to relate drift velocity to time. After these polynomial equations were generated, they were integrated from the time the specified pixel location was scanned in the reference image to when it was scanned in the deformed image to provide the total drift that occurred between these scans. The drift displacements were subtracted from the displacement data to correct for drift distortion.

It is important to note that pixel drift is not constant within the image. At low magnifications with image resolutions coarser than approximately 750 nm/pixel, it will commonly appear as a vertical gradient in the displacement fields, while at higher magnification such as in the experiments in chapters IV and V, it can have
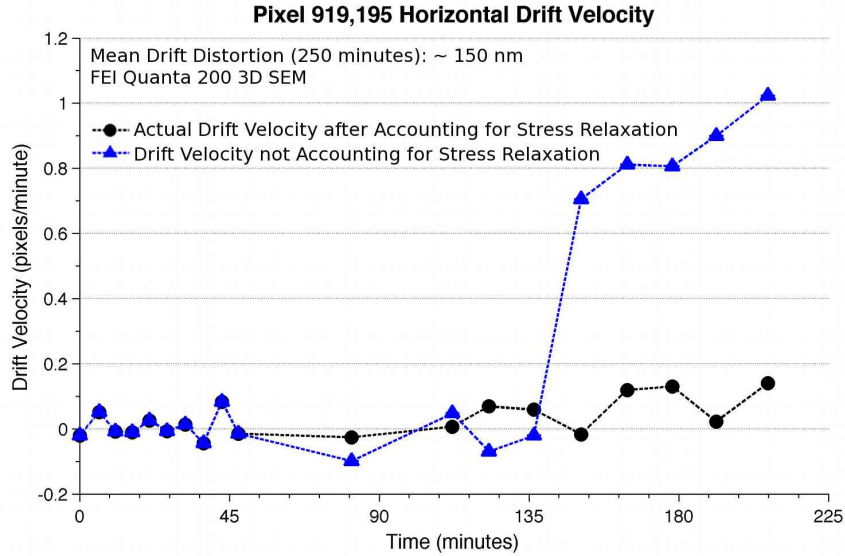
Figure 3.14: Trend in drift velocity at a specified pixel location throughout a test previously performed on 6061-T6 Al. Stress relaxation erroneously affects drift velocity and if not accounted for, will result in an overcorrection of the drift distortion. This test was performed at an image resolution of 68 nm/pixel (70 µm HFW) and a horizontal tensile axis.

complex curvature similar to that shown in figure 3.15. Drift distortion is related to the image resolution, and is more problematic in high spatial resolution experiments, as shown in figure 3.16. To generate figure 3.16, the magnitude of the mean drift velocity was calculated for each calibration phase stationary image pair in each test, and the largest magnitude value from each test was plotted. While the drift in pixels/minute increases at finer image resolutions, when converted to physical drift, the maximum drift velocity is near 10 nm/minute for all image resolutions. Thus, the effect of pixel drift increases with magnification; for example, after one minute in a 1 mm HFW, a pixel will have drifted nominally 10 nm or 0.001% of the HFW. However, after one minute in a 10 µm HFW, a pixel will have drifted 10 nm, or 0.1% of the HFW. These drifts can add up over the typical duration of a SEM-DIC experiment. In a previous test with an image resolution of 29 nm/pixel (30 µm HFW), drift velocities as high as 0.34 and 0.28 pixels/minute in the horizontal and vertical directions respectively were observed, which resulted in up to 14 (horizontal) and 68

62

(vertical) pixels of distortion in the final test images of the 4.5-hour experiment. Note that larger distortion was observed in the vertical direction for that test, because the vertical drift velocity remained nominally constant, whereas the horizontal distortion was initially high and then settled near zero (an occurrence specific to this test). In that previous test, the difference in vertical drift displacement over the entire final test image was approximately 13 pixels. If uncorrected, these 13 pixels constitute a significant displacement error which would have resulted in a vertical strain error of up to 0.014.
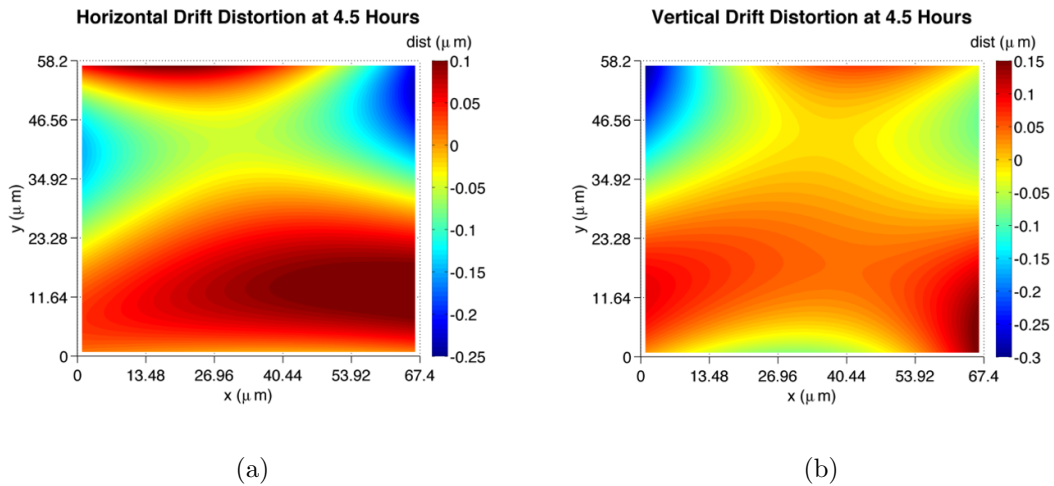
Figure 3.15: Horizontal (a) and vertical (b) drift distortion surfaces at the end of a 4.5 hour test performed on 1100 Al. These surfaces need to be subtracted from the horizontal and vertical displacement fields to correct for drift distortion.

3.2.4   Drift Distortion: Accounting for Stress Relaxation

If the material being studied undergoes significant stress relaxation, drift distortion corrections performed without accounting for it can lead to greater distortions than if the images had been left uncorrected. Stress relaxation [105, 126, 142] exists in calibration image data captured during the test phase because SEM image capture proceeds by scanning an electron beam over the surface of a test specimen, capturing each pixel sequentially (rather than simultaneously as with an optical camera). Long
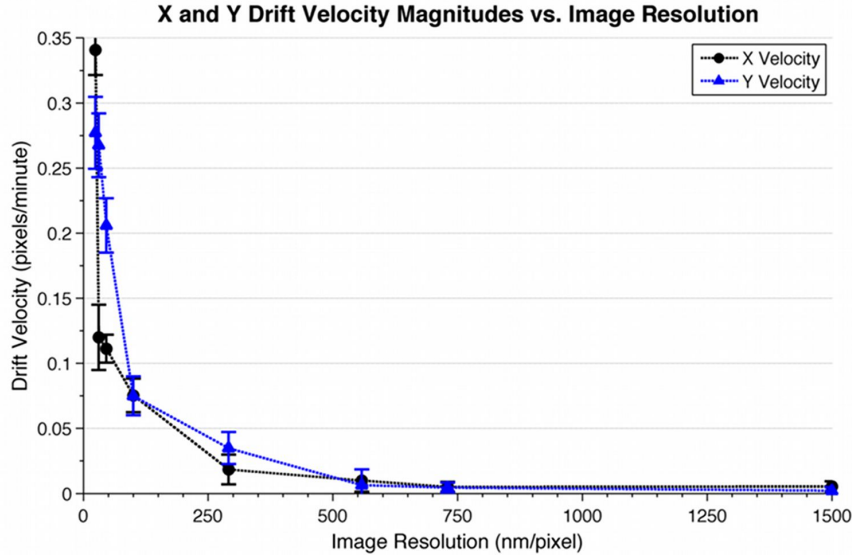
Figure 3.16: Drift velocity (in pixels/min) decreases at coarse image resolutions (larger nm/pixel values), leveling out for image resolutions coarser than nominally 750 nm/pixel. When converting to physical drift, the max drift velocity at every image resolution is less than 10 nm/min. Error bars represent the standard deviation.

image scans are required in SEM-DIC to increase the signal to noise ratio, but can capture stress relaxation that occurs while the displacement is held constant for image acquisition. The triangle data points in figure 3.14 are the calculated drift velocities, affected by stress relaxation, at one specific (x, y) position in the calibration images from a tensile test on 6061-T6 Al (horizontal tensile axis) at an image resolution of 68 nm/pixel (70 μm HFW). Note that the first 50 minutes represent the calibration phase, when the specimen was under zero applied load and the drift velocity remained nominally centered around zero. After plastic deformation occurred at 135 minutes, the effect of stress relaxation on the displacement field became immediately apparent and the drift velocity appeared to rapidly increased. The actual drift velocity, where stress relaxation was accounted for through the use of an unloaded calibration pattern, is shown by the circular data points in figure 3.14 and remained nominally constant as loading proceeded. This nominally constant drift velocity was confirmed in additional tests with image resolutions ranging from 29 to 1500 nm/pixel. Thus,

the use of drift correction displacement fields affected by stress relaxation would lead to gross over-correction of drift distortion, increasing the overall distortion.

Large stress relaxation induced displacements in stationary calibration image pair data were observed in aluminum tensile specimens when the load drop between image scans exceeded 1 N. Consider as an illustrative example the load vs. time plot for a 6061-T6 Al test specimen tested at an image resolution of 68 nm/pixel (70 µm HFW) with a horizontal tensile axis, shown in figure 3.17. The stress relaxation occurring in the dashed box in figure 3.17, at nominally 9000 seconds, is clearly evident as a vertical gradient in the horizontal displacement field of the stationary calibration image pair captured during this time, shown in figure 3.18. Note, figure 3.18 has not been corrected for image distortion; however, drift and spatial distortion were very small over the short period of time that passed and the small displacements that occurred between image capture. The relaxation rate was largest directly after loading stopped, and subsequently leveled as the displacement was held constant for image acquisition. This relaxation led to the top of the image in figure 3.18 shifting 180 nm to the right and the bottom of the image shifting by 60 nm. The horizontal displacements shown in figure 3.18 were much greater than those in the calibration phase stationary image pairs, which averaged 15 nm, thus leading to increased distortion if this data was used for distortion correction.

Two techniques to remove stress relaxation effects, if observed in calibration image pairs captured during the test phase, are described below. The first technique (used in the experiments presented in chapters IV and V) removes stress relaxation from distortion corrected data by utilizing an unloaded pattern on a separate substrate for calibration images. The unloaded calibration pattern was applied to an Inconel sheet and placed next to the tensile specimen through the use of an ancillary positioning device as shown in figure 3.19. Inconel's resistance to creep and low coefficient of thermal expansion are particularly important for high temperature SEM-DIC testing.
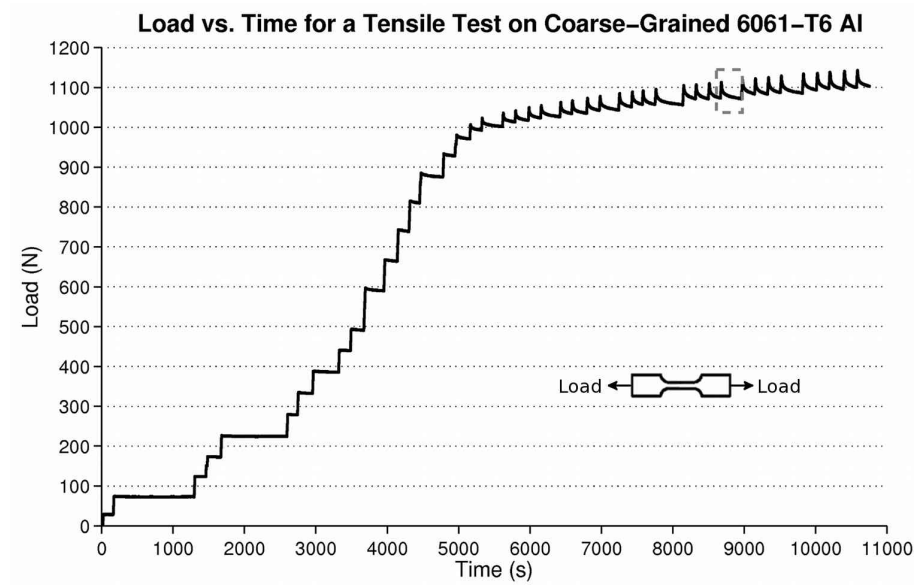
Figure 3.17: Load vs. time for a test on coarse-grained 6061-T6 Al. In the elastic regime, the load remains nearly constant during image capture. After plastic deformation occurs at 5,000 seconds, larger load drops during image capture are apparent. This test was carried out at a strain rate of 10^{-4} s^{-1}.
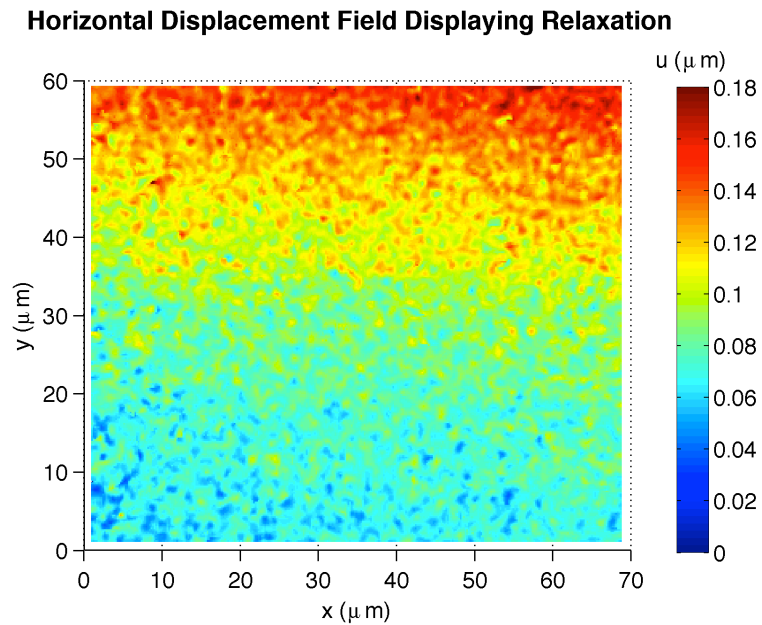
Figure 3.18: Horizontal (u) displacement field from the stationary image pair captured during the time period highlighted by the dotted box in figure 3.17. Stress relaxation of the 6061-T6 Al tensile specimen occurred throughout the entire image scan, but at a greater rate initially than at the end.

66

For convenience, the pattern does not need to be directly applied to the Inconel if the test is conducted at nominally ambient temperatures. Instead, the pattern can be applied to a small piece of the test material attached to the top of the Inconel, allowing imaging of the tensile specimen and the calibration pattern without adjusting contrast and brightness. The position of the calibration pattern is adjusted with the ancillary positioning device controlled through the use of the SEMs external positioning knobs, using z-control to locate the pattern at the exact working distance of the tensile specimen and rotation control to locate the pattern away from the heating element used in high temperature tests as further protection against creep. The ancillary positioning device is mounted directly to the tensile stage so that when calibration images are needed, the x and y stage positioning knobs can be used to translate from the tensile specimen to the calibration pattern. Note that the test specimen pattern can be used during the (unloaded) calibration phase, but the unloaded pattern should be used after loading of the specimen begins.
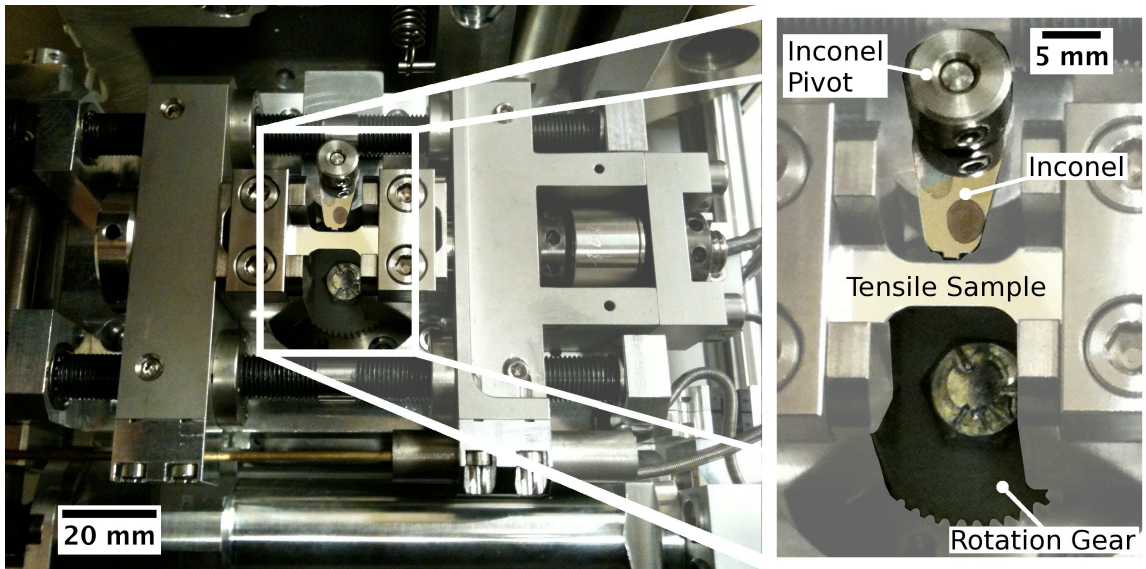
Figure 3.19: Grip section of the *in-situ* tensile stage, showing the aluminum tensile specimen and Inconel sheet with a nanoparticle speckle pattern for specimen-independent calibration, which improves distortion correction accuracy.

If stress relaxation is apparent and hardware modifications cannot be made to the

SEM or tensile stage for use of an unloaded pattern, a second technique linking the relaxation-induced displacement to the load drop that occurs during the calibration image scans can be used. This technique has been validated with experiments at image resolutions from 30 to 300 nm/pixel. Figure 3.20 shows the load drop that occurred due to stress relaxation during the capture of the stationary calibration image pair in the highlighted area of figure 3.17. The top curve shows the load profile for the first image scan and the lower curve shows the load profile for the second image scan. Since the time each pixel was scanned is known, surfaces were created consisting of the load at each pixel in each scan. The surface from the second scan was then subtracted from that of the first in order to reveal the change in load that occurred at every pixel between the first and second image, as shown in figure 3.21. As expected, the load drop surface in figure 3.21 shows a similar gradient as the horizontal displacement field in figure 3.18. (Note that if the relaxation was to the left, causing the displacement to be initially negative and increase over the scan, the load data could be flipped so that both load and displacement data increased over the scan). The load drop surfaces were then converted to displacement surfaces and aligned with the horizontal (u) displacement fields through the application of a conversion factor. The conversion factor was determined by finding the value that, when multiplied by the load surface, minimized the difference between all of the u displacement fields and their associated load surfaces. For the 6061-T6 Al test and specimen geometry considered here, the conversion factor was found to be 0.024 µm/N. The conversion factor was applied to the load surfaces, and the converted surfaces were subtracted from the u displacement fields. The displacement field from figure 3.18 is shown in figure 3.22 after relaxation was removed. The remaining curvature of the displacement field is due to drift and spatial distortions and can now be removed with subsequent distortion correction. This technique was initially developed for single image scans but has also been applied to integrated image scans,

in which image integration is used to further reduce data noise. To correct integrated images, the load drop that occurred over each image scan was calculated and then averaged. In the integrated images, relaxation was still observed in the horizontal displacement fields for a horizontal tensile axis, but the magnitude was reduced. This technique can also be applied to images in which the tensile axis is vertical. Then relaxation will be observed in the vertical displacement field with a vertical gradient similar to that shown in figure 3.18.
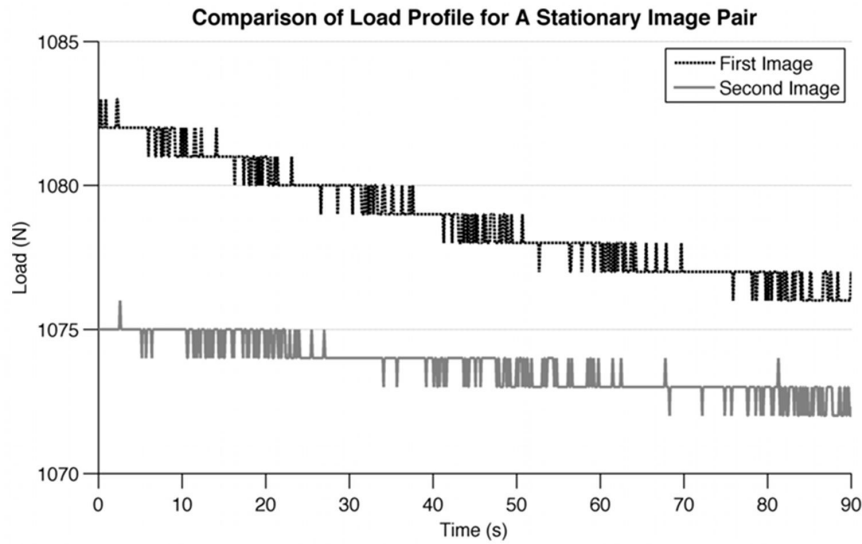
Figure 3.20: Load drop that occurred for the stationary image pair captured of the 6061-T6 Al tensile specimen during the highlighted period shown in figure 3.17.

Both of the approaches discussed above effectively remove the effects of stress relaxation from calibration image data, and the user must decide which technique to implement. An unloaded pattern can be used at any image resolution and is the easiest to implement if it is possible to make minor modifications to the SEM or tensile/compression stage. Since the unloaded pattern calibration images do not suffer from stress relaxation, their DIC data can be used as-is for distortion correction. Relating relaxation displacements to the load drop allows for quantification of the stress relaxation, but adds the additional step of correcting the calibration data for relaxation prior to using it for distortion correction. However, since the relationship
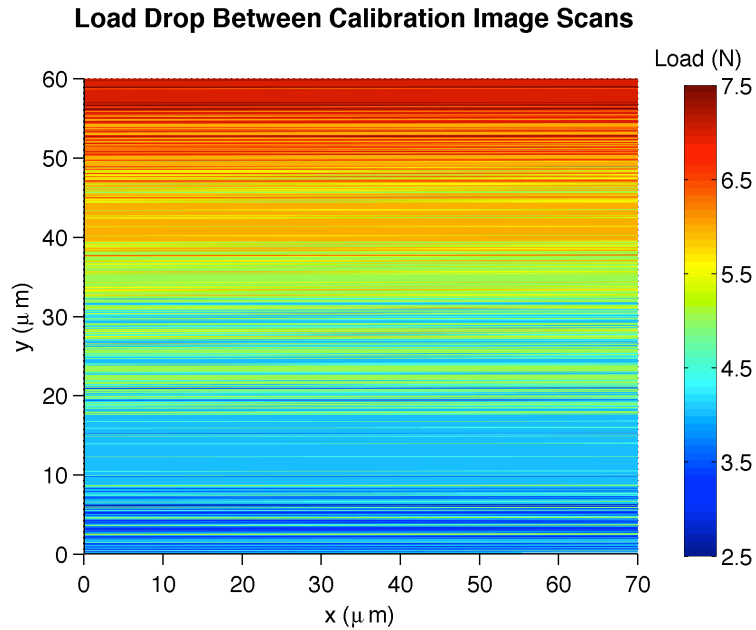
Figure 3.21: Surface representation of the load drop that occurred between the first and second image captured of the 6061-T6 Al tensile specimen during the highlighted period shown in figure 3.17.
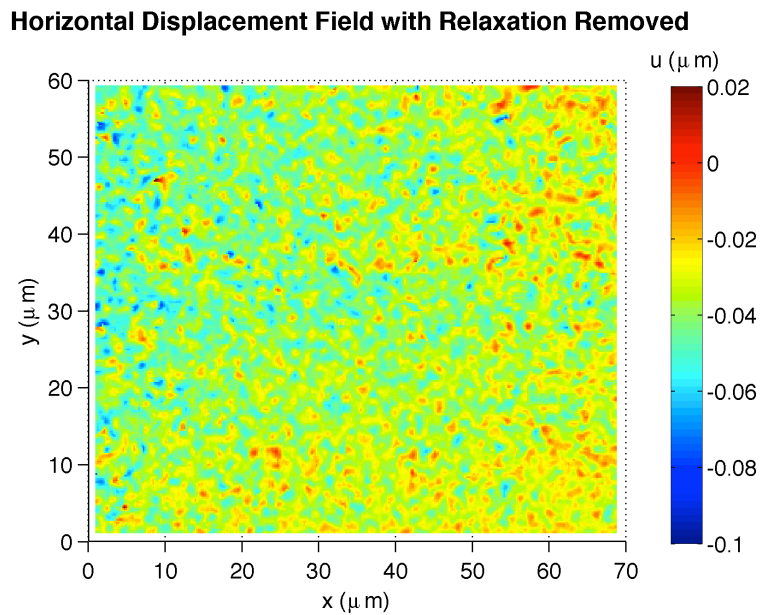
Figure 3.22: Displacement field of the 6061-T6 Al tensile specimen from figure 3.18 after displacements due to relaxation have been removed. The remaining curvature of the displacement field is due to drift and spatial distortions and can now be removed with subsequent distortion correction.

between load drop and stress relaxation displacements is known, application of this technique does allow for the removal of stress relaxation from test image data. This technique has only been validated in experiments from 30 to 300 nm/pixel. At image resolutions coarser than 300 nm/pixel, stress relaxation displacements are of very small magnitude and have not been detected. Additionally, note that the conversion factor changes with material, specimen geometry, and number of image integrations. For example, in tests performed on ultrafine-grained pure Al using four image integrations at an image resolution of 31 nm/pixel (110 µm HFW), the conversion factor was found to be 0.06 µm/N versus 0.024 µm/N for the single scans of 6061-T6 Al presented here. Variations in the relaxing displacement fields at areas of strain localization could not be observed. Additionally, stress relaxation was not observed in 1100-O Al tensile tests at image resolutions of 29 and 33 nm/pixel where the load drop between test-phase calibration image pairs never exceeded 1 N. Unless the user desires to quantify stress relaxation, the use of an unloaded pattern is recommended for ease of implementation and simplicity.

3.2.5 Spatial Distortions

Spatial distortions can cause large errors in the calculated displacement fields, particularly in high strain or large displacement tests. For example, spatial distortions of 1.60 pixels (in the tensile direction) were observed in pure aluminum specimens at a strain of 0.2 for an image resolution of 700 nm/pixel (720 µm HFW). Spatial distortion is similar to the distortion present in optical lenses, but it cannot be corrected with classical parametric distortion models due to the complex electromagnetic focusing and scanning processes utilized in an SEM. While spatial distortion remains nominally constant throughout a test, it has been observed to change between tests due to filament replacement, gun or aperture alignments, or other service performed on the electron column. In this work, it has been observed that spatial distortion

decreases as magnification increases.

Spatial distortion is itself a function of displacement, and thus can be quantified from translated image pairs captured during the calibration phase. As mentioned previously and as outlined in [171], during the calibration phase the specimen was translated by known amounts in x (u displacement) and y (v displacement). These displacements were sized so that the total translation in each direction was greater than that expected during the test. In this work, a total translation of approximately 1/4 of the FOV size was used. Using the image just prior to the first translation in each direction as a reference (x ref and y ref in figure 3.13), digital image correlation was performed on the first image captured after each translation. This resulted in data sets composed of displacement fields for pure u and v displacements of varying magnitude ($x, 2x, 3x, 4x$ and $y, 2y, 3y, 4y$ as shown in figure 3.13).

Prior to being used for spatial distortion correction, the translated DIC data was corrected for drift distortion using the functions generated from the stationary image pairs. Next, the input rigid body displacements were subtracted from each data set. If undistorted, the resulting u and v displacement fields would be centered at zero. Therefore any nonzero displacement data points are a result of spatial distortion (and image noise, which must be minimized). The spatially distorted u and v displacement fields were then fit with biquintic surfaces, as shown in figure 3.23 for a test on 1100-O Al at an image resolution of 33 nm/pixel (67.4 µm HFW). Figure 3.23(a) (3.23(b)) represents the u (v) spatial distortion for a 10 µm displacement in only the x (y) direction. Figure 3.23(c) (3.23(d)) shows the u (v) spatial distortion for a 10 µm displacement in only the y (x) direction. If the specimen was translated 10 µm in both the x and y directions, the u (v) spatial distortion would be the sum of figure 3.23(a) and 3.23(d) (figure 3.23(b) and 3.23(c)) as shown in figure 3.23(e) (3.23(f)). Surfaces similar to those shown in figure 3.23 exist for each input translation. A trend in the curvature of these surfaces with the input rigid body translation was apparent

and was used in the following steps to correct for spatial distortion.

A linear relationship between spatial distortion and input translation was evident at all data points. After obtaining the spatial distortion surfaces for each rigid body translation, the spatial distortion at each individual data point was plotted against the input translation value, as shown in figure 3.24. At each data point, this yielded four linear functions unique to that data point (u and v distortions for displacements in the x direction, and u and v distortions for displacements in the y direction). Figure 3.24 shows the u distortion and v distortion data and linear best-fit curves for a series of translations in the x direction.

Once these four functions were determined for every data point, the spatial distortion in each test image was removed by entering the u and v displacement at each data point into the spatial distortion linear functions for that specific point. The linear functions yielded unique u and v spatial distortion fields that were subtracted from the drift distortion corrected displacement fields to remove spatial distortion.

Distortion in the displacement fields can have a large effect on the strain field error. Figure 3.25 shows the distortion in the strain field from the test possessing the drift distortion shown in figure 3.15 and spatial distortion similar to that shown in figure 3.23. Note that the actual displacements in the final test image represented in figure 3.25 ranged from -1 µm to 4 µm horizontally and -0.5 µm to 3 µm vertically. Thus the spatial distortion surfaces were less than half the magnitude of those shown in figure 3.23, yet the drift and spatial distortion combined still resulted in up to 1% strain error. This error, if not removed, would have yielded inaccurate results and could have hidden true strain localization. The results of this example demonstrate the importance of distortion correction.
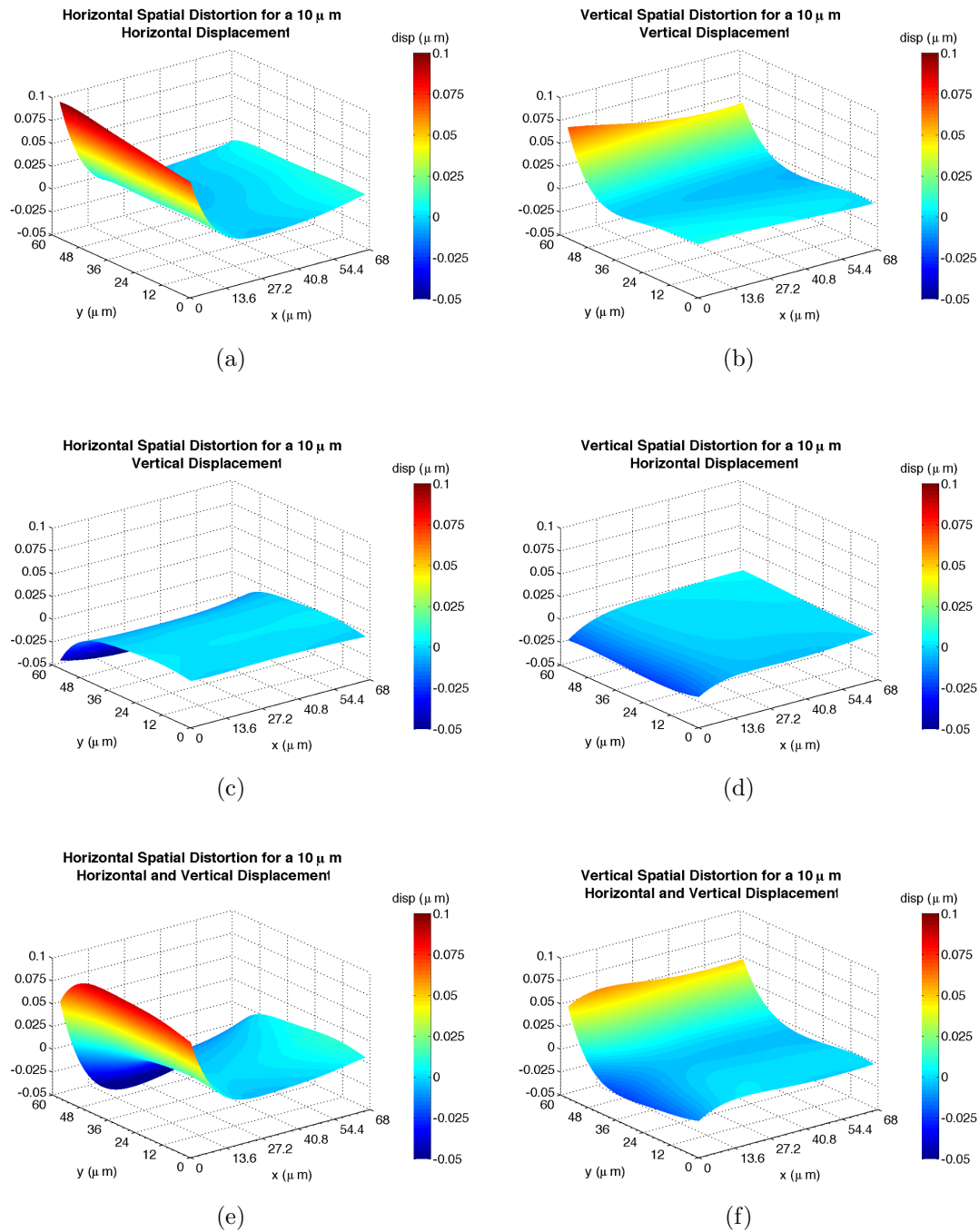
Figure 3.23: Spatial distortion surfaces for 10 μm horizontal and vertical displacements. These surfaces were obtained from a test on 1100-O Al at an image resolution of 33 nm/pixel (67.4 μm HFW). Note that these surfaces scale with input translation.
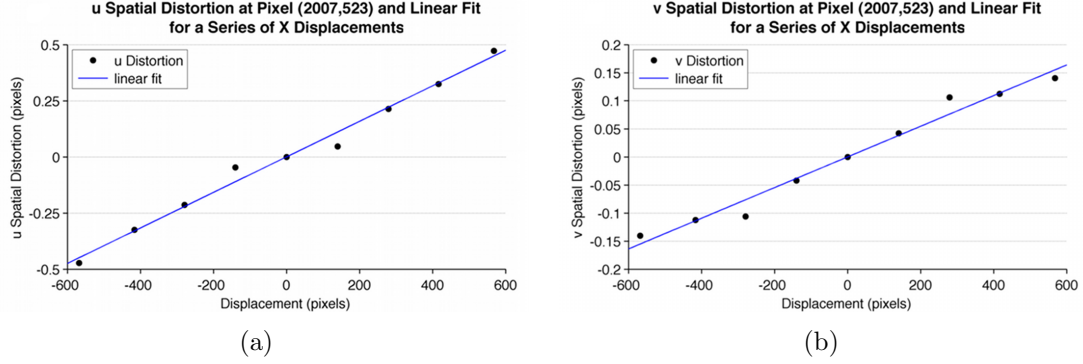
Figure 3.24: (a) horizontal and (b) vertical spatial distortion at pixel location (2007,523) and linear curve fit for a series of translations in the x direction for the 33 nm/pixel image resolution (67.4 μm HFW) experiment on 1100-O Al also shown in figure 3.23.

3.3 Noise Reduction

SEM images can suffer from substantially more noise than optical images [34, 170], which limits the minimum discernible displacement measurements. The noise comes from the statistical nature of the electron production from the gun and the interactions of these electrons with the specimen, and thus is different for every pixel. In addition, the secondary or backscatter electron detector can generate noise and the circuitry within the SEM can then amplify this noise [85].

In this section, guidelines for improving the signal to noise ratio in SEM-DIC will be described. SEM imaging parameters must be carefully selected to obtain micrographs with low levels of noise, a particularly important consideration when handling brittle materials or examining low strain phenomena. Drift and spatial distortion corrections have minimal effect on the amount of random, SEM-introduced noise inherent in the displacement fields. A general guideline for minimizing SEM image noise is to use a long dwell time and high beam current. Image integration, in which multiple images are captured and the grayscale value at every pixel is averaged over all of the images, is also effective in reducing image noise [170]. This comes from the fact that the noise distribution is random and thus will not be at the same
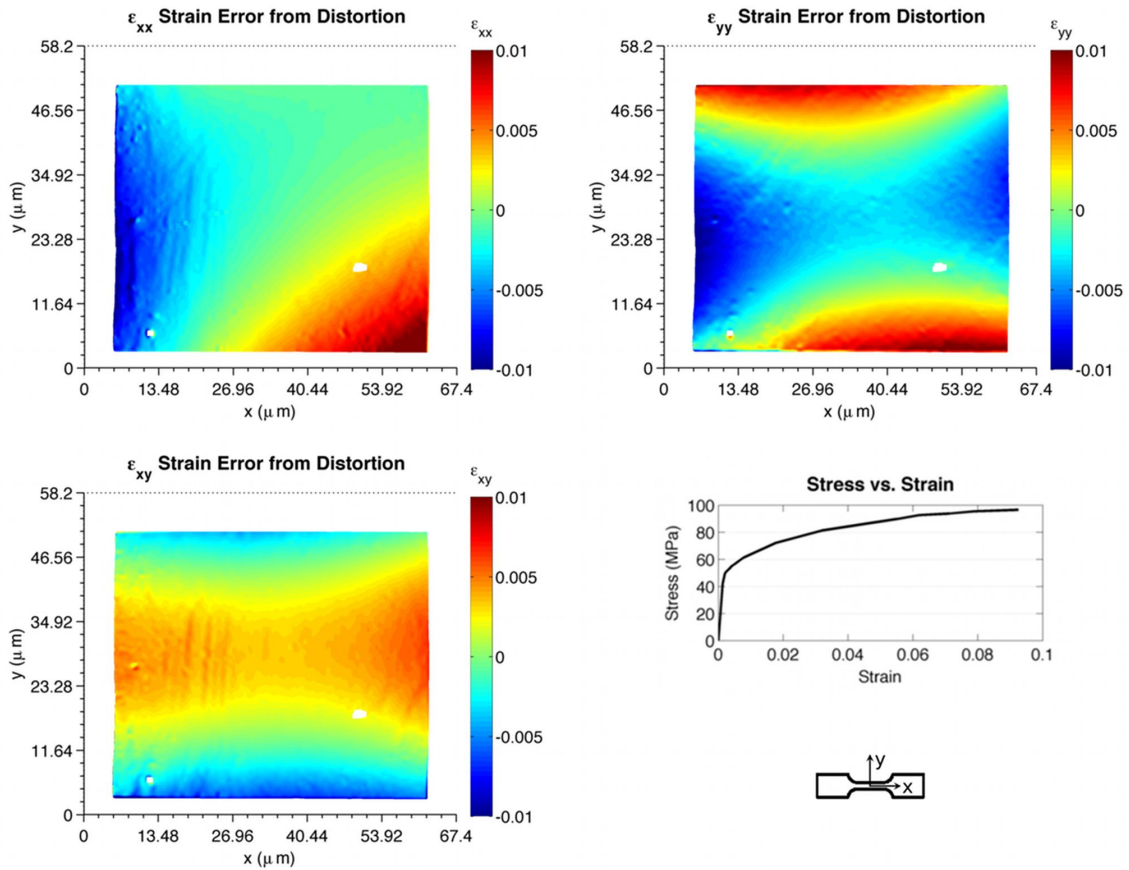
Figure 3.25: Strain field distortion from the experiment possessing the drift and spatial distortion fields shown in 3.15 and 3.23. This strain error of 1% would have resulted in inaccurate results and could have hidden true strain localization.

location in each scan, causing it to be of a reduced magnitude in the final averaged image. However, care must be taken when using image integration to avoid capturing images when stress relaxation is causing the load to drop rapidly, as specimen motion can cause blurring of the resulting image and reduced correlation accuracy. Noise reduction through image integration is also possible with optical Charge-Coupled Device (CCD)s, but is often not utilized since it would require loading to be paused and thus is not included in this comparison.

Noise in SEM-DIC data can be quite large and has a strong dependence on imaging parameters, but with careful experimentation it is possible to reduce SEM noise greatly, to levels below those observed in a Point Grey Grasshopper, Model 50S5M/C-C CCD, commonly used for optical DIC. Figure 3.26 compares standard deviations in the SEM-DIC displacement field across a wide range of different imaging parameters. The SEM images in this plot were captured with the secondary electron detector in a FEI QUANTA 200 3D SEM with a tungsten filament, working distance of 16 mm, and an image resolution of 500 nm/pixel (500 µm HFW). The pattern was created with drop-cast gold AuNPs and a 15 x 15 pixel subset (subset size selected to contain on average nine speckles) and a 3 pixel step size were used for correlation. For the purposes of this comparison, a low magnification was used to avoid the image shifts commonly observed at higher magnifications in single image scans [170]. These image shifts appear at HFWs smaller than approximately 100 µm as horizontal bands of abrupt changes in displacement in both the u and v displacement fields. Since the location and width of these bands change from scan to scan, image integration is effective at removing them and must be used at smaller HFWs. It is important to note that CCD images do not suffer from these image shifts.

The displacement noise for a commonly used optical CCD (Point Grey Grasshopper, Model 50S5M/C-C, 2448 x 2048 pixel resolution) was calculated as a comparison to the data presented in figure 3.26. The speckle pattern for the optical DIC data was
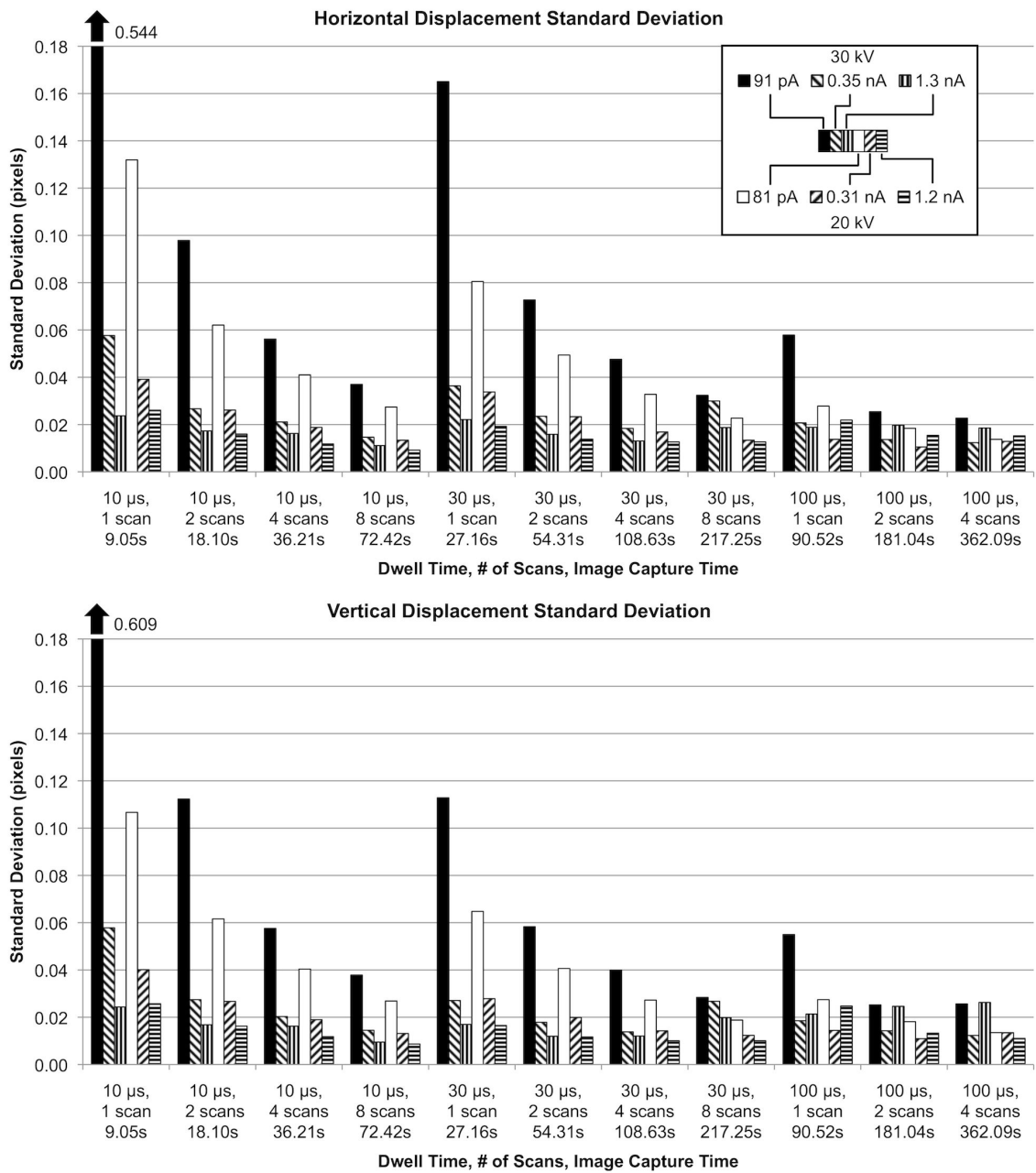
Figure 3.26: Standard deviations in the SEM-DIC displacement fields for different imaging parameters. Noise is minimized by using a 1.2/1.3 nA beam current, 10 micosecond dwell time, and 8 image scans for a total image scan time of 72.42 seconds. In general, increasing beam current and dwell time reduces image noise. (81/91 pA=spot size 3, 0.31/0.35 nA=spot size 4, and 1.2/1.3 nA=spot size 5).

created by coating the specimen with Golden Airbrush Titanium White paint #8380 and then overspraying it with Golden Airbrush Carbon Black paint #8040 from an airbrush (model Iwata Custom Micron B). DIC was performed using a subset size of 21 x 21 pixels and step size of 3 pixels (subset size selected to contain on average nine speckles). Prior to comparison, both the SEM and CCD images were trimmed so that 80,000 data points were analyzed.

As apparent in figure 3.26, SEM image noise is reduced with a larger spot size, longer dwell time, and more image integrations. The smallest standard deviations of 0.0092 pixels in the horizontal direction and 0.0087 pixels in the vertical direction were achieved at a 20 kV accelerating voltage, 1.2 nA beam current, and 10 microsecond dwell with 8 image integrations. These images took 72.42 seconds to capture and had less noise than images that took over twice the time to capture. These SEM noise levels are both smaller than those of the Grasshopper CCD with horizontal and vertical standard deviations of 0.0126 and 0.0099 pixels respectively. While the data presented in figure 3.26 is from a tungsten filament SEM, displacement noise from images captured in a Philips XL30 FEG-SEM was also minimized with low voltage, high beam current, long dwell time, and image integration. Typically, noise levels in a FEG-SEM will be lower than those in a tungsten filament SEM due to the higher brightness and lower energy spread of the field emission source compared to the tungsten filament. The reader should note that the noise characteristics of the Point Grey Grasshopper CCD do not necessarily represent the noise present in other optical imaging systems. Optical noise levels lower than the SEM noise stated here may be achieved with different CCD or CMOS systems through cooling of the chip and/or image integration.

At low strain values, noise in the displacement and strain fields can hide true displacement and strain localization. In these cases, a local averaging filter is useful to make areas of localization apparent. Application of the filter will blend the strain

values so they will be of a reduced magnitude; therefore, this approach is not appropriate for obtaining quantitative values of small strains, but rather as a method to pinpoint initial localization. The averaging filter box should be sized to contain both the high value (peak) and neighboring low value (valley) of noise to effectively cancel them out. If the size of the filter box is too small to capture at least one noise peak and valley, the data will not be smoothed. Conversely, an oversized filter box containing numerous peaks and valleys may smooth the data more than desired. Figure 3.27(a) shows an axial strain field from the test on 1100-O Al where high levels of noise, 3.27(b), make strain localization difficult to discern. It also shows the noise observed in the axial strain field from stationary image pairs captured during this test. This "noise threshold" peaks at strains of 0.030 while the axial strain field peaks at only 0.050, making it difficult to identify strain localization. Figure 3.27(c) shows the same strain and noise fields, 3.27(d), after a 95 x 95 pixel (3.13 x 3.13 μm) averaging filter represented by the box at the top left of the strain field in figure 3.27(a) has been applied to the data. After application of the averaging filter, the noise peaks are now 0.004 while the peaks from the actual strain field are 0.012, making it easier to identify strain localization. This technique is useful for identifying the relationship between initial strain localization and specific areas of the microstructure.

SEM-DIC data also experiences an interpolation bias [174, 151] that shows up as regular vertical (horizontal) lines in the horizontal (vertical) displacement and strain fields. These lines can disguise actual displacement and strain data at low strain values, but can be reduced by using higher order interpolation filters [151]. Additionally, a smooth transition from black to white in the speckle pattern or the application of a low-pass filter to DIC images will reduce interpolation bias [151]. This interpolation bias is often easy to recognize and does not interfere with the identification of strain localization.
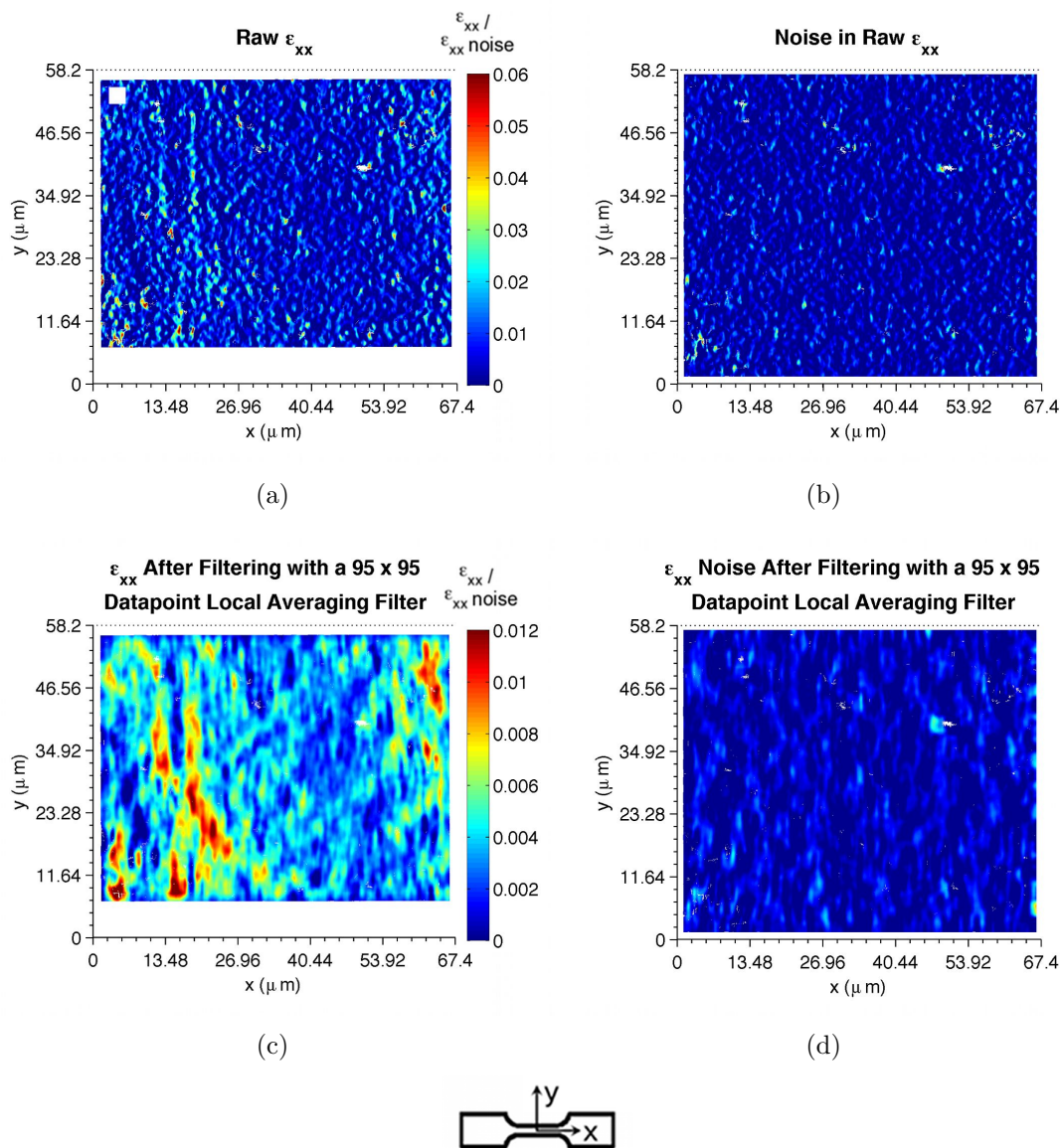
Figure 3.27: Axial strain fields at a globally applied strain of 0.004 for the tensile test on 1100-O Al. (a) shows the raw axial strain field and (b) shows the axial strain noise field observed in stationary calibration image pairs. The high noise level makes identifying strain localization a challenge. (c) shows the same strain field and (d) shows the same noise field after the application of a 95 x 95 pixel averaging filter denoted by the white box in the axial strain field in (a). Strain localization now stands out from the noise. Note that (a) and (b) share the color bar shown in (a) and (c) and (d) share the color bar shown in (c).

3.4 Conclusions

Scanning electron microscopy combined with digital image correlation is a powerful new experimental technique that enables displacements and strains to be measured with nanometer spatial resolution. This chapter has detailed the work that has been performed in the development of this technique, including tracking pattern application, image distortion correction, and noise reduction. In this chapter, it has been demonstrated that:

1. FIB patterning can produce a pattern with speckle diameters down to 100 nm. However, it is a time consuming technique and is not an efficient way to pattern a large area. FIB patterning has potential in tests where a highly controlled pattern is only required in a specific area of the FOV, thus requiring a short time to pattern.

2. Template patterning through stock polycarbonate membrane filters can produce patterns with 0.4 µm speckle diameters and is a quick process, requiring only the time to pump down the evaporator/sputter-coater chamber and deposit the metal film. However, the filter pores are not dense, and evaporation through multiple filters would be required.

3. E-beam lithography has the greatest repeatability of any of the analyzed patterning methods. An e-beam SEM-DIC pattern can easily be scaled up or down, was successfully applied to both ceramic and Al substrates, and can be used to create a pattern for high temperature testing. The greatest shortcoming of e-beam patterning is the cost related to the e-beam usage. E-beam lithography also does not create a truly random pattern and pattern contrast is not as good as that in AuNP patterns.

4. Drop-cast AuNP patterning has been used successfully to generate patterns

with speckle diameters down to approximately 300 nm. While smaller diameter AuNPs can be purchased, the minimum speckle size is limited by clumping. The greatest shortcoming of drop-cast AuNP patterning is controlling the location of the area with a suitable DIC-quality pattern. The preferential arrangement of 200 nm diameter AuNPs on an Al surface following EBSD can be used for tests with FOVs of approximately 300 µm x 260 µm.

5. We found self-assembly of AuNPs to be the best small-scale patterning option. Self-assembly of AuNPs can be utilized to pattern both metallic and non-metallic substrates, complex geometries, and delicate test specimens. This patterning technique is capable of producing speckles smaller than any other technique developed and also enables multi-scale experimental investigations.

6. SEM image distortions can introduce significant error into SEM-DIC displacement fields. Drift distortion velocity as high as 0.34 pixels/minute for an image resolution of 29 nm/pixel and spatial distortion of 1.6 pixels for an image resolution of 730 nm/pixel at a strain of 0.2 were observed in this work. Drift distortion is more problematic at high magnification while spatial distortion dominates at low magnification.

7. Performing drift distortion corrections without accounting for stress relaxation can result in larger errors than if the data was left uncorrected. Stress relaxation can be removed through the use of an unloaded calibration pattern or by relating the load drop that occurs during image capture to the stress relaxation displacements.

8. In a typical SEM-DIC test, image distortions have resulted in strain errors as high as 1% if left uncorrected.

9. As a general guideline, high beam current (large spot size), long dwell time, and

image integration should be utilized to reduce image noise.

10. The location of early strain localization can be correctly determined by the application of an appropriate averaging filter to minimize noise inherent to the SEM imaging process. This results in averaged strain values and does not provide quantitative early strain measures.

CHAPTER IV

Room Temperature Experiments

This chapter presents results from room temperature *in-situ* tension tests of ECAP processed ultrafine-grained aluminum dogbone tension specimens. Section 4.1 begins by detailing the microstructures investigated. Different size FOVs were utilized to probe strain localization at high spatial resolution and also to get a broader overview of the overall material behavior. The tests follow the general experimental procedure outlined in section 2.3; however, specifics for each test are provided in section 4.2. Different strain rates were utilized in an attempt to probe strain rate sensitivity at the microstructural length scale. The results are presented in section 4.3, starting with general observations and comparisons between the macroscopic response of the material in this work and in previous works. Subsection 4.3.1 provides results and analysis related to observations of intragranular and intergranular strain localization. Subsection 4.3.2 covers the relationship between strain localization and the grain boundary trace angle and slip system angles resulting from ECAP processing. Subsection 4.3.3 presents results on the strain localization behavior and deformation mechanisms active at the boundaries separating microstructure bands. This banded microstructure is unique to ECAP processed materials and leads to interesting micro-scale behavior. Analysis of these experiments yields new information on the deformation mechanisms active in ultrafine-grained Al and the relationship between strain localization and mi-

crostructural features.

4.1 Microstructures Investigated

FOVs were chosen to contain different distinct microstructures that are common in ECAP processed UFG Al. Inverse pole figure (IPF) maps of each FOV are shown in figure 4.1, and the FOV characteristics in tabular form are presented in table 4.1. Each FOV came from a separate tension specimen, although the microstructures present in the individual FOVs existed in all specimens and all billets. These FOVs provide a good reflection of the overall UFG microstructure and demonstrate that ECAP processing typically does not yield equiaxed ultrafine-grains separated by predominately HAGBs as previously demonstrated [42, 75, 89, 180, 181, 186]. The distribution of grain boundary misorientations is presented in figure 4.2, showing that approximately 60% of the grain boundaries in the FOVs investigated had misorientations below 15°. LAGBs were very common in the ECAP processed microstructure and were prevalent in supergrain areas of microstructure. In addition to the supergrain microstructure, experiments in this work also focused on banded microstructures and conventional ultrafine-grained microstructures.

Microstructure Identifier	FOV Size µm	Average Grain Size	% HAGBs	Mode of Grain Boundary Trace Angle
UFG-1	60 x 51.8	2.1	34	33.5 +/- 29.9
UFG-2	51.2 x 44.2	3.1	50	20.5 +/- 20.8
UFG-3	24.4 x 21	1.2	53	32.5 +/- 26.6
UFG-4	25.6 x 22.1	2.6	26	39.5 +/- 27.4
UFG-5	51.2 x 44.2	1.9	36	21.5 +/- 19.2
UFG-6	164 x 141.6	2.5	25	41.5 +/- 40.8
UFG-7	110 x 95	3.2	37	52.5 +/- 41.5
UFG-8	50 x 43.2	2.9	49	59.5 +/- 41.9

Table 4.1: Microstructural characteristics for the eight fields of view investigated.

UFG-2 and UFG-5, in figure 4.1(b) and 4.2(e) respectively, consisted of microstructure bands separated by very HAGBs and composed of grains with orientations near
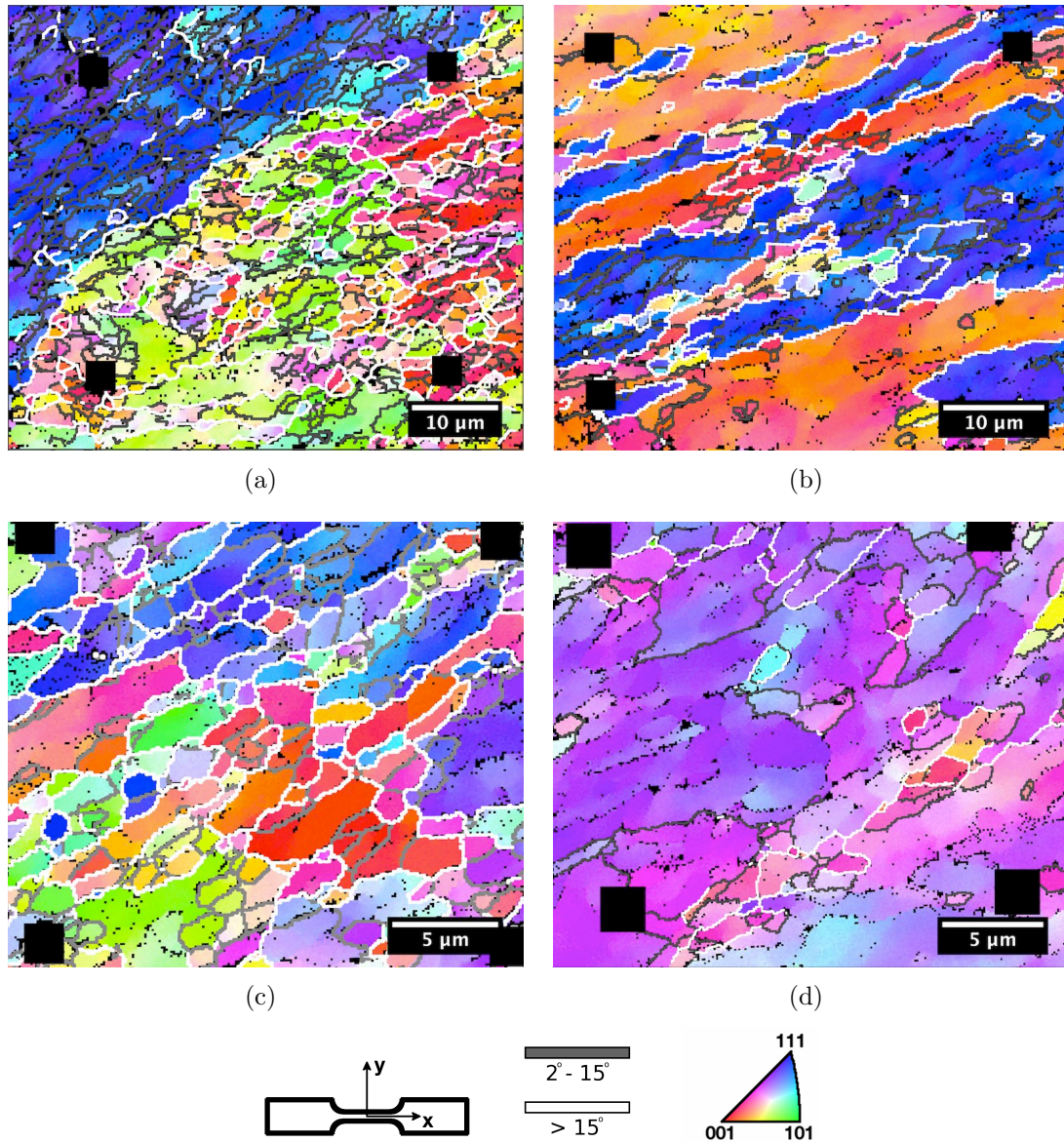
Figure 4.1: Inverse pole figure maps of the fields of view investigated in the room temperature experiments. (a) UFG-1, (b) UFG-2, (c) UFG-3, (d) UFG-4, (e) UFG-5, (f) UFG-6, (g) UFG-7, and (h) UFG-8.

(e)

(f)

(g)

(h)
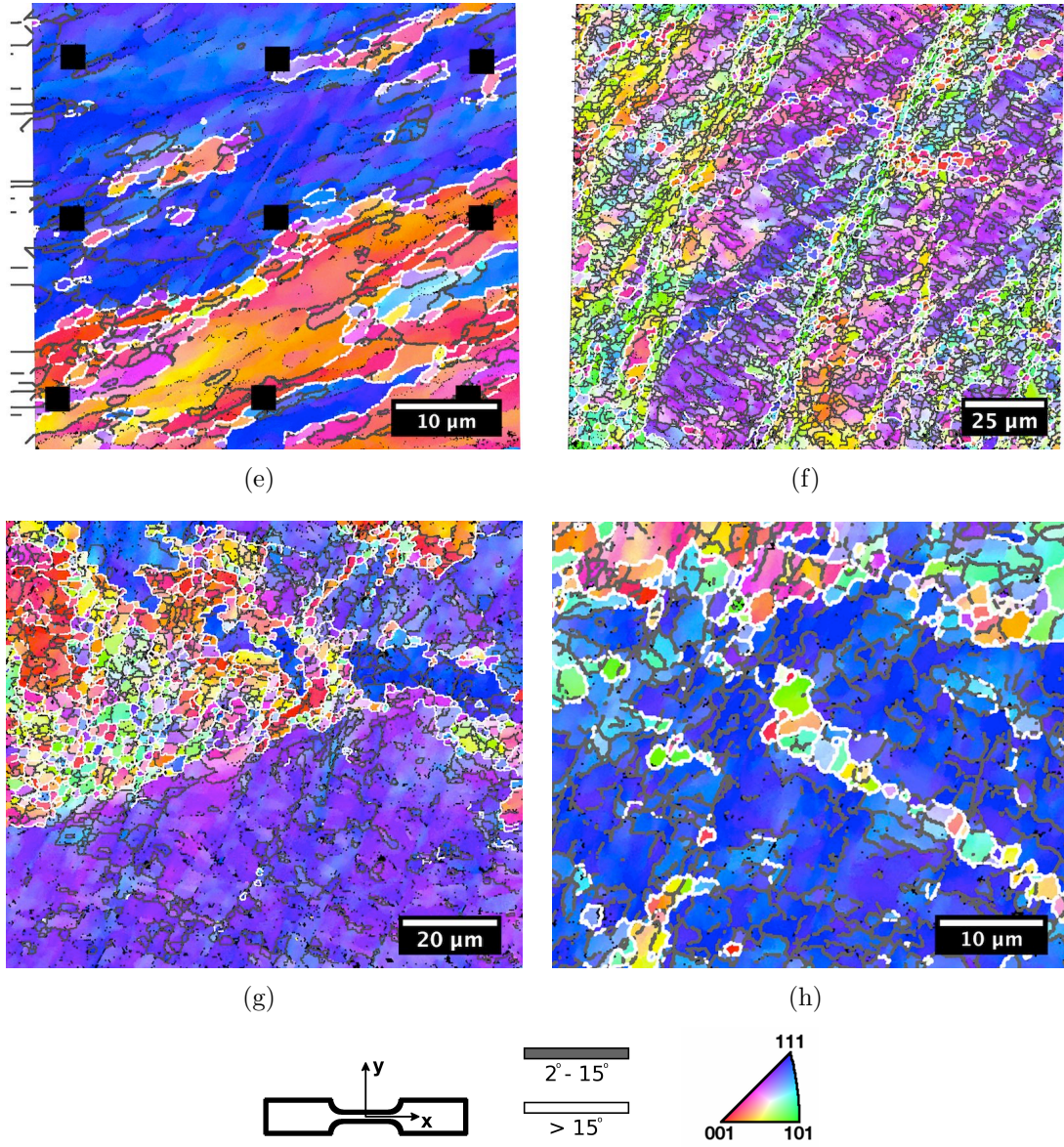
Figure 4.1 (continued)
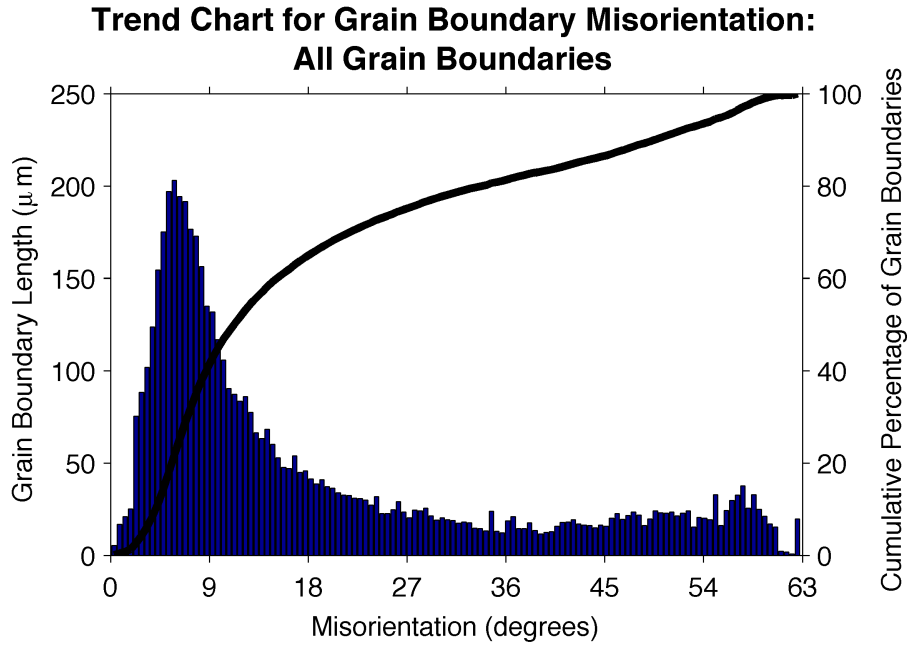
Figure 4.2: Histogram showing the distribution of grain boundary misorientation and corresponding cumulative percentage of grain boundaries for all grain boundaries.

either $\{111\}\langle\bar{2}11\rangle$ or $\{001\}\langle110\rangle$. The grain boundaries separating microstructure bands had an average misorientation of 55.26° +/- 2.62° in UFG-2 and 48.77° +/- 5.39° in UFG-5. This microstructure led to a bimodal grain boundary misorientation distribution consisting of the very high misorientation HAGBs separating microstructure bands and the LAGBs separating grains within microstructure bands. These microstructure bands are a common feature in ECAP processed Al and have been noted in many prior publications [55, 128, 204]. In all prior work, the microstructure bands had similar orientations and grain boundary misorientations separating bands to those in this work.

While ECAP processing is supposed to develop HAGBs, supergrains are very common and made up a large portion of the FOVs investigated. The microstructure bands in UFG-2 and UFG-5 were considered supergrains. Supergrains were also present in UFG-1, UFG-4, UFG-6, UFG-7, and UFG-8 and were typically composed of grains with a crystalline orientation near $\{111\}\langle\bar{2}11\rangle$ (appearing as purple in the inverse pole

figure maps). An inverse pole figure of the parent coarse-grained microstructure is shown in figure 4.3 and does not show a preference for this orientation. Thus it is a result of the 45° theoretical shear plane in the ECAP die leading to the $\{111\}\langle 0\bar{1}1\rangle$ slip system being angled at approximately 45° to the positive x-axis and perpendicular to the sample face.
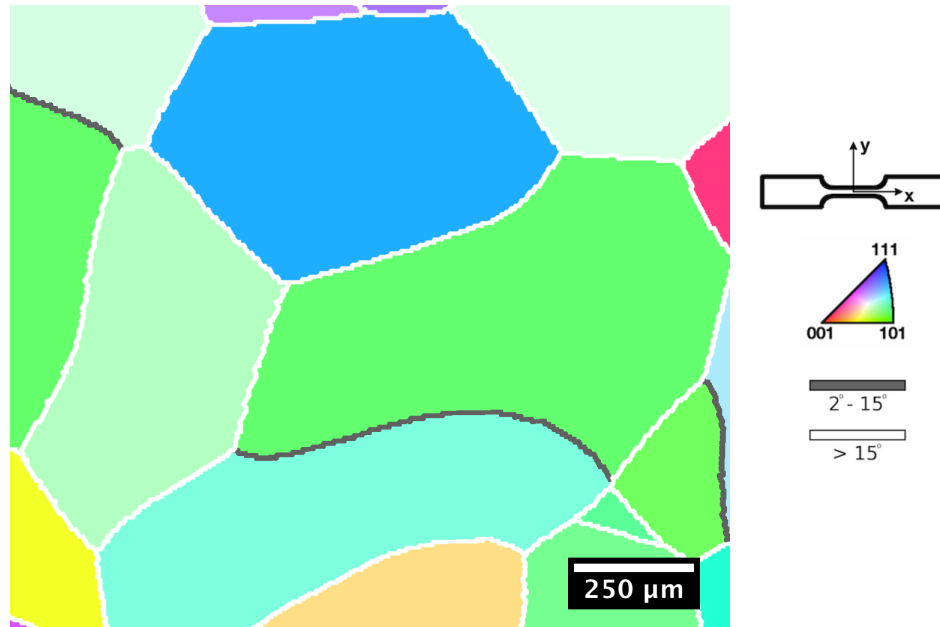
Figure 4.3: Inverse pole figure map of a coarse grained 99.99 % pure Al billet from the same lot as those that were ECAP processed. The crystalline orientation is much different than that in the ECAP processed material.

Contiguous areas of ultrafine grains separated by primarily HAGBs were apparent in every FOV, with the exception of UFG-4. UFG-4 was composed of two supergrains and several ultrafine grains at the boundary between supergrains and at the edges of the FOV. In contrast, UFG-3 was nearly completely composed of ultrafine grains separated by HAGBs resulting from the parent coarse grains being aligned favorably for successful grain refinement.

While the microstructures studied had different mean grain sizes and grain boundary misorientations, they shared numerous similarities that led to similar strain localization behavior. All of the microstructures analyzed had mean surface grain

boundary trace angles near the theoretical grain boundary inclination angle of 26.6°
predicted for a cubic element passed through a single ECAP pass [75, 206]. This
is demonstrated in figure 4.4, which shows a histogram for the distribution of grain
boundary trace angles in all of the fields of view investigated. This preferential grain
inclination angle should not exist after four passes utilizing route B_C, but is prevalent
in the microstructures investigated. As apparent in table 4.1, the grain boundaries in
UFG-7 and UFG-8 were angled at much steeper angles; however, these microstruc-
tures display a bimodal trace angle distribution with a lesser peak near 26.6°. In
addition to a common grain boundary trace angle, all of the microstructures had
high Schmid factors, with 98.7% of the surface area analyzed possessing a Schmid
factor greater than 0.4. As previously mentioned, this results from the 45° theoretical
shear plane in the ECAP die leading to the $\{111\}\langle 0\bar{1}1 \rangle$ slip system being angled near
the plane of maximum resolved shear stress in tension.
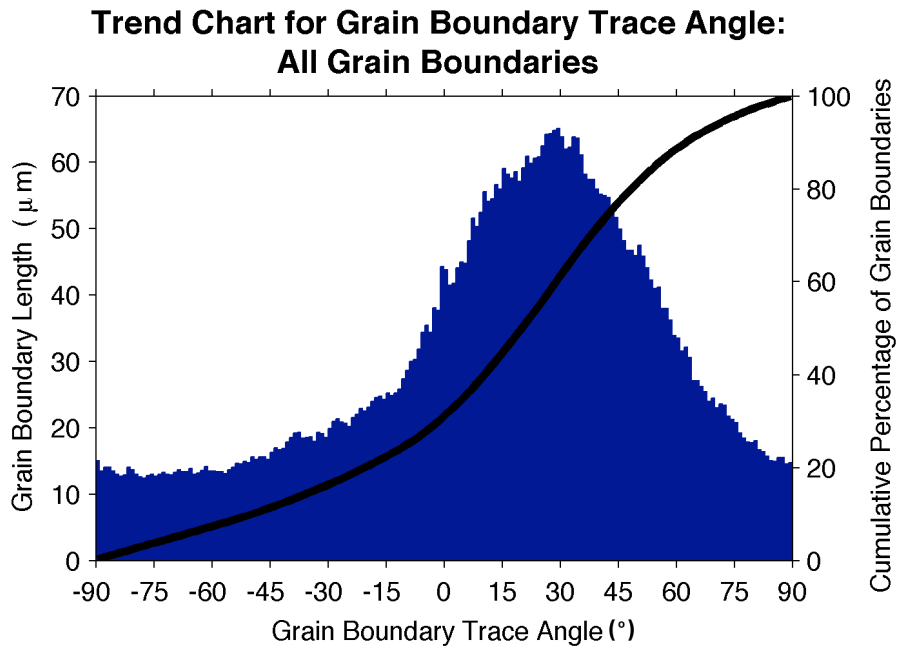
Figure 4.4: Histogram showing the distribution of grain boundary surface trace
angles and corresponding cumulative percentage of grain boundaries for all grain
boundaries.

4.2　Experimental Procedure

Room temperature experiments were performed at both variable strain rates (to probe strain rate sensitivity at the microstructural length scale) and constant strain rates. Tests on UFG-1 and UFG-2 were performed at strain rates of 1.25×10^{-5} s^{-1}, 1×10^{-4} s^{-1}, 1×10^{-3} s^{-1}, and 3.125×10^{-3} s^{-1} in strain steps of 0.5%. Strain rate sensitivity was visible in the stress-strain curves generated by the load cell data and LVDT displacement data shown in figure 4.5 for UFG-1, but not in the SEM-DIC strain fields, where it would have appeared as changes in strain intensity or location. In a second attempt to observe room-temperature strain rate sensitivity, UFG-5 was strained at strain rates alternating between 1.25×10^{-5} s^{-1} and 3×10^{-3} s^{-1} in strain steps of 2.5%. Even at these large strain steps, strain rate sensitivity was not observed in the resulting strain fields due to the fact that a narrow neck formed in the material shortly after plastic deformation, leading to low strains in the FOV. These low incremental strains achieved during the individual small displacement steps were too small to be captured by SEM-DIC because they were below the noise-induced strain error of up to 0.24%. At higher strains this noise was quickly overwhelmed and did not hide strain localization in the strain fields calculated by correlating each deformed image to the sole unloaded reference image.

UFG-3, UFG-4, UFG-6, UFG-7, and UFG-8 were all tested at the constant strain rate of 1×10^{-4} s^{-1} with strain step ranging from 0.125% to 0.5%. The smallest strain steps were utilized prior to and around the macroscopic yield stress of the material to capture initial strain localization. After localization had occurred, larger load steps were utilized to achieve high strain levels in the limited time available to perform the experiments.

Due to performance issues with the FEI Quanta 200 3D SEM used in these experiments, primarily involving variability in image quality and noise due to filament lifetime and alignment, image capture settings differed between experiments. Imaging
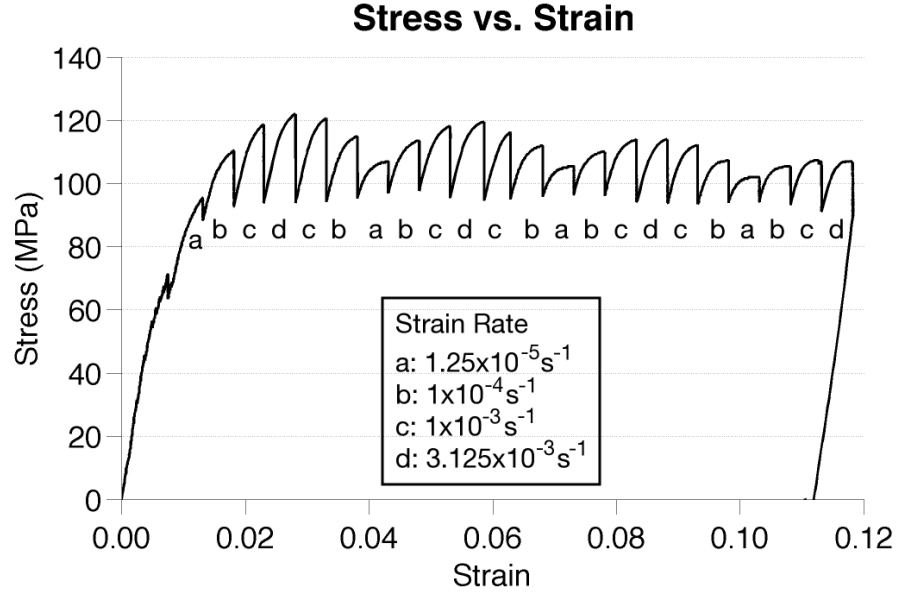
Figure 4.5: Macroscopic stress-strain curve calculated from grip displacement displaying strain rate sensitivity.

settings for each experiment are outlined in table 4.2. These settings were chosen to improve the signal to noise ratio and do not affect the accuracy of the SEM-DIC data. A pause of six minutes between the end of loading and image capture was utilized to reduce image blurring.

Microstructure Identifier	Accelerating Voltage (kV)	Beam Current	dwell time (µs)	# of image integrations
UFG-1	30	0.35 nA	10	4
UFG-2	30	0.35 nA	10	4
UFG-3	30	0.35 nA	100	1
UFG-4	20	0.31 nA	100	1
UFG-5	20	0.6 nA	30	1
UFG-6	30	0.35 nA	10	4
UFG-7	30	0.35 nA	10	4
UFG-8	30	0.35 nA	10	4

Table 4.2: SEM image capture settings for room temperature experiments.

SEM-DIC was performed on the captured micrographs utilizing a step size of one pixel and a subset size selected to contain between 3 x 3 speckles and 5 x 5 speckles on average. Following distortion correction, strain was calculated by fitting

93

the displacement data in 15 x 15 data point subsets with local bi-quadratic surfaces. The coefficients of these surfaces populated the deformation gradient tensor ($\mathbf{F}$) for each 15 x 15 subset, which was then used to calculate the Lagrangian finite strain tensor, $\mathbf{E} = (1/2)[\mathbf{F^T F} - \mathbf{I}]$, where $\mathbf{I}$ is the identity matrix. 15 x 15 data points were chosen to generate the bi-quadratic surfaces to reduce the effect of noise on the resulting strain field and match the strain fields calculated from the commercial DIC software for undistorted displacement data. More details on the strain calculation procedure are provided in Appendix B.

4.3 Experimental Results and Discussion

Results from these tests yielded extensive new data linking strain localization and active deformation mechanisms to the UFG microstructure. As discussed in section 1.2.4, ECAP processed materials have been extensively studied in numerous tension/compression and micro-indentation tests. Many of these previous works lacked details on the underlying microstructure and treated the gage section as possessing a homogeneous microstructure. The experiments presented in subsections 4.3.1 and 4.3.2 relate quantitative measures of strain to the underlying grain boundary misorientation and surface trace angle. Experimental investigations by others found dislocation slip and grain boundary sliding to be active through post-test surface analysis or activation volume calculations. Here, utilizing SEM-DIC combined with EBSD, dislocation slip was found to be most active on slip systems well aligned with the ECAP theoretical shear plane in the final pass. Grain boundary sliding was found to only be active in regions of the microstructure containing microstructure bands as discussed in subsection 4.3.3.

The macroscopic response of the material tested in this work was very close to that of the material tested by others. One measure of this similarity is the macroscopic yield strength of the material tested. Here, the yield strength was measured to be 93.0

+/- 11.2 MPa, which is close to the measurements of 117 MPa in work by Ivanov et al. [74]. Their higher yield strength may be explained by the differences in the ECAP die utilized to process the material. Additionally, Ivanov used a strain rate of 8.6 x 10^{-3} s^{-1} as opposed to 1 x 10^{-4} s^{-1} in the experiments from which the yield strength was calculated in our work. Even with these differences, our material, which has a heterogeneous microstructure, still has a similar yield strength to theirs which was presented as having a more homogeneous microstructure. It is unclear whether their entire microstructure was truly homogeneous or if homogeneity was only achieved in small areas as in our material.

The macroscopic strain rate sensitivity calculated from these tests is also similar to that measured in previous works. Strain rate sensitivity was visible in the macroscopic stress-strain curves generated from the load cell load data and grip displacement for UFG-1, UFG-2, and UFG-5 which were subjected to strain rate jumps. This strain rate sensitivity is apparent as jumps/drops in stress with changing strain rate as shown in figure 4.5 for UFG-1. From the load cell data and strain rate, the strain rate sensitivity,

$$m = \delta \ln \sigma / \delta \ln \dot{\epsilon} \qquad (4.1)$$

was calculated from all three tests as 0.018 +/- 0.002, which is within the values of 0.013 - 0.026 obtained by others for UFG pure and commercial purity Al [69, 119, 120, 144, 168]. Although the material tested here did display macroscopic strain rate sensitivity, it was too small to be measured in the DIC strain fields. This macroscopic strain rate sensitivity was approximately four times greater than the strain rate sensitivity for coarse-grained 99.99 % pure Al ($m = 0.0048$) [168].

Figures 4.6, 4.7, 4.8, and 4.9 show the strain fields for each FOV in the final test

image. In all constant strain rate tests, initial strain localization occurred at HAGBs (localization was already prevalent at the time of the first image capture in the strain rate jump experiments). To study the relationship between strain localization and the underlying microstructure, the microstructure characteristics of grain size, grain boundary misorientation, grain boundary trace angle, Schmid factor, angle between adjacent highest Schmid factor slip directions, angle between adjacent highest Schmid factor slip plane normals, crystalline orientation, difference between adjacent grain sizes, and difference between adjacent Schmid factors were investigated. Of these characteristics, grain boundary misorientation, grain boundary trace angle, and the geometric compatibility factor, m', for active slip systems in adjacent grains had the largest effect on strain localization. The geometric compatibility factor m' [15, 116] is defined as

$$m' = \cos\psi\cos\kappa, \tag{4.2}$$

where ψ is the angle between the adjacent grains' active slip plane normals and κ is the angle between adjacent grains' active slip directions. A m' value of 1 means that the slip systems in adjacent grains are perfectly aligned, while an m' value of 0 means that either the slip plane normals, slip directions, or both are angled at 90° to each other. Therefore, a low m' value denotes a grain boundary where damage nucleation is likely. Details of the full-field strain localization and active deformation mechanisms, as they relate to the underlying microstructure, will be discussed in the following subsections.
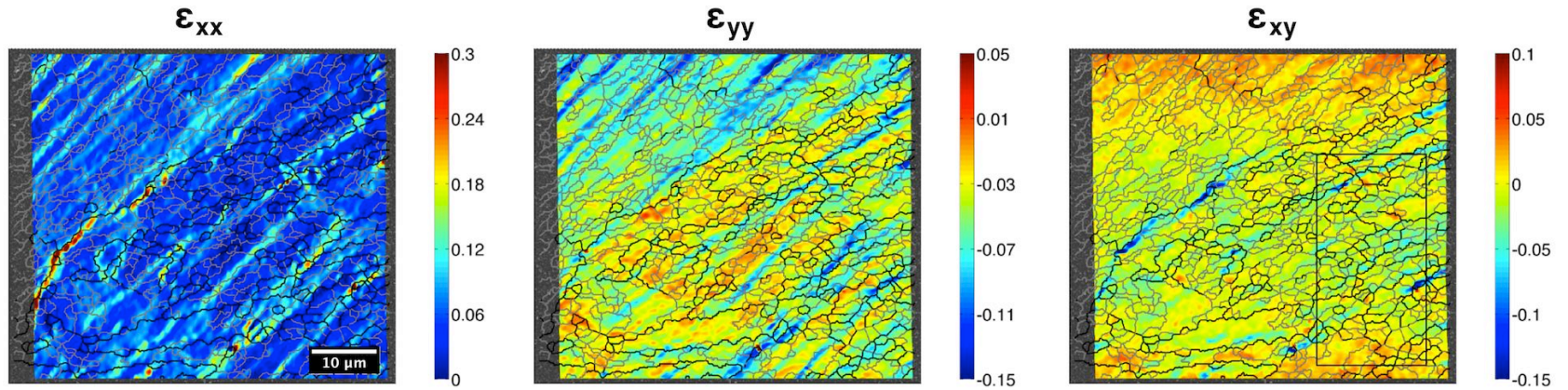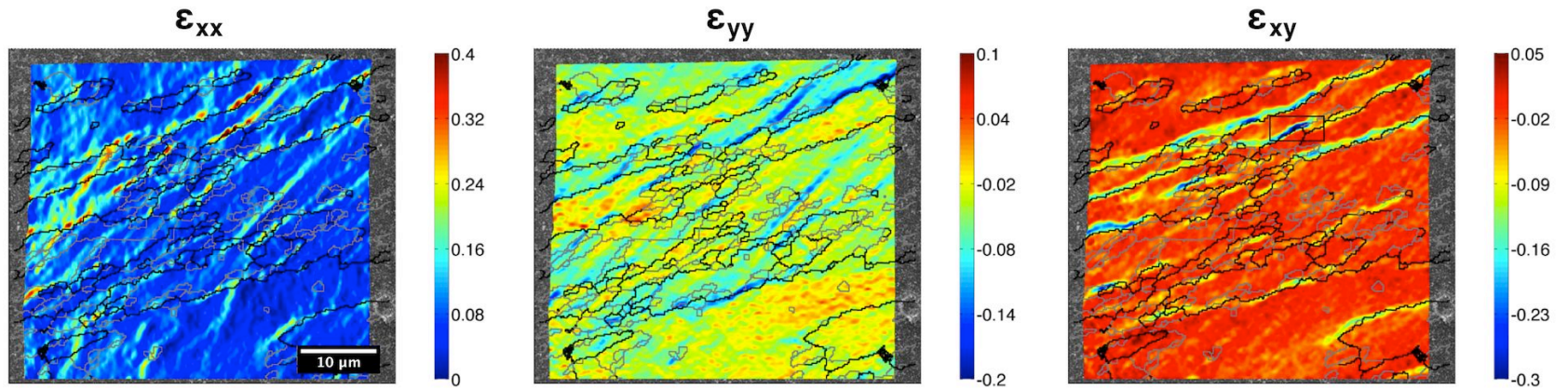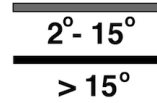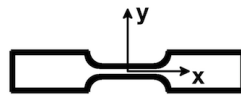
Figure 4.6: Strain fields for UFG-1 (a) at a macroscopic strain of 9.0% and UFG-2 (b) at a macroscopic strain of 9.0%.
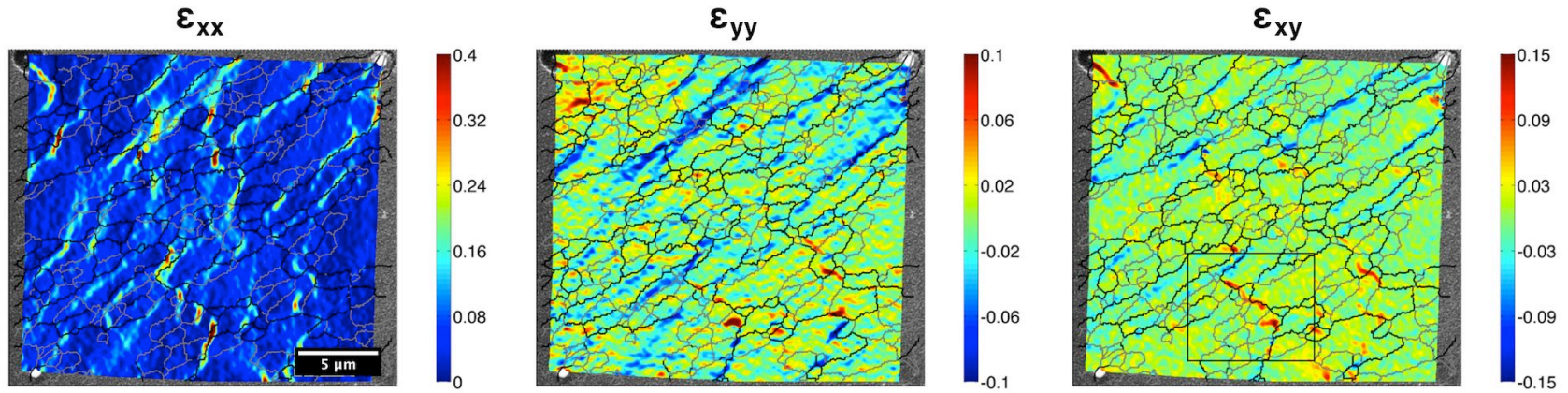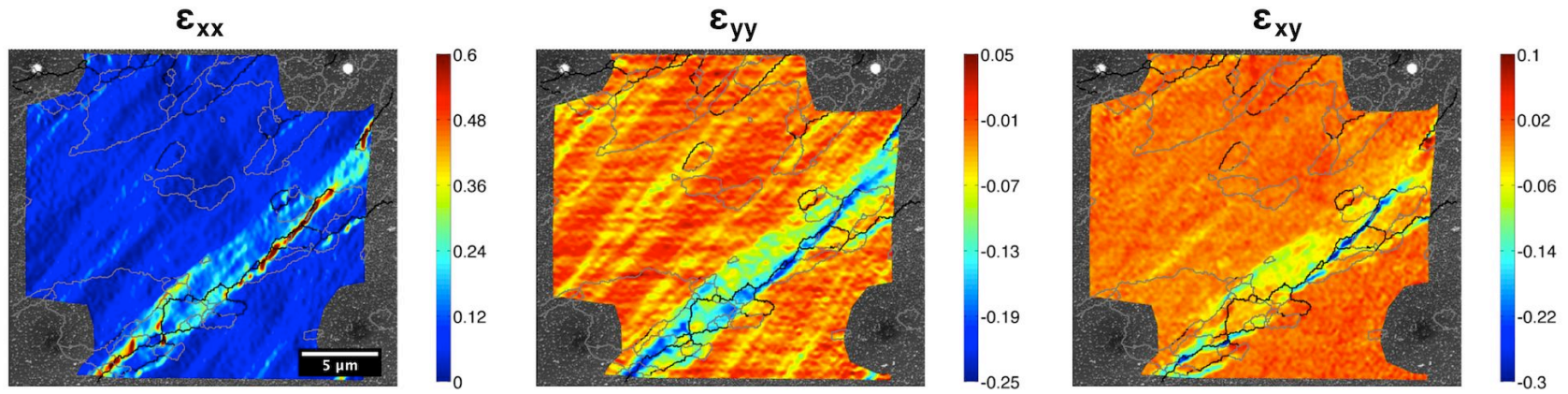
Figure 4.7: Strain fields for UFG-3 (a) at a macroscopic strain of 5.2% and UFG-4 (b) at a macroscopic strain of 5.9%.
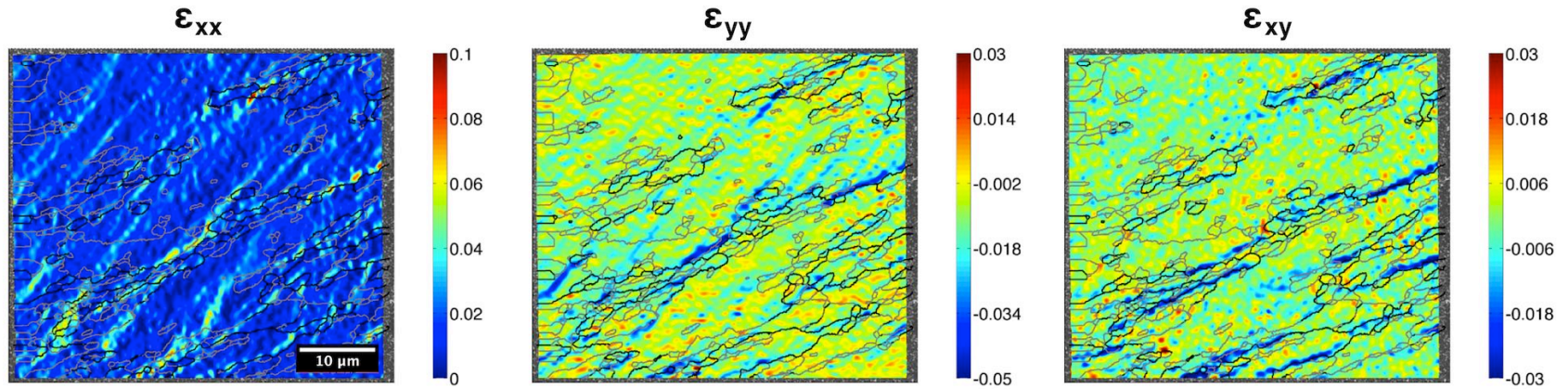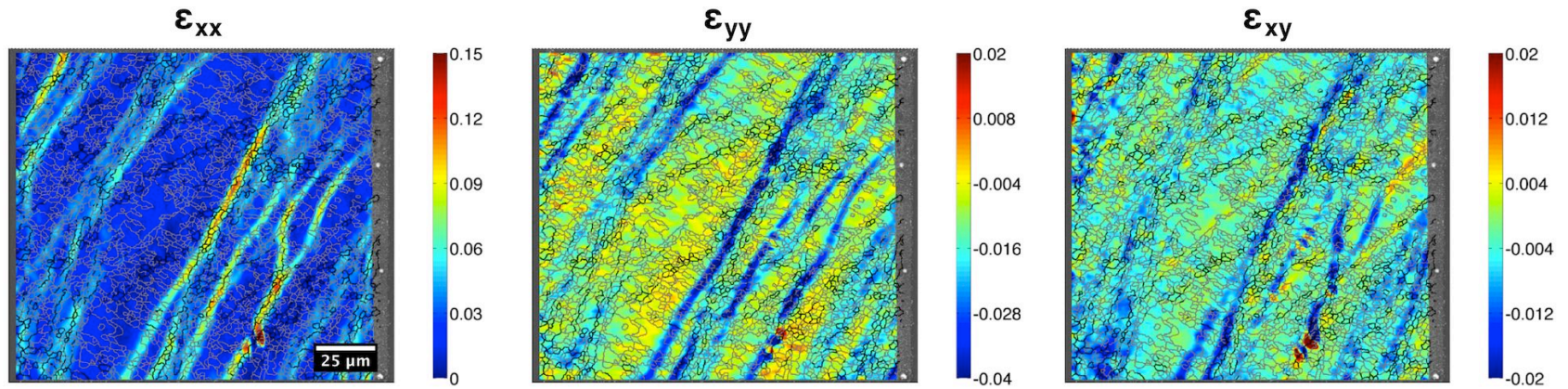
Figure 4.8: Strain fields for UFG-5 (a) at a macroscopic strain of 14% and UFG-6 (b) at a macroscopic strain of 6.0%.
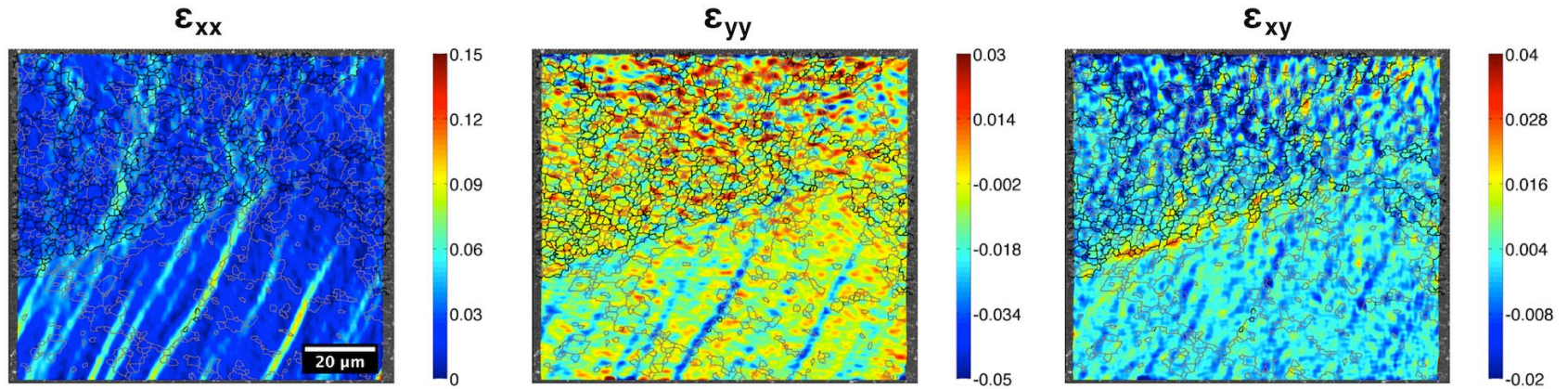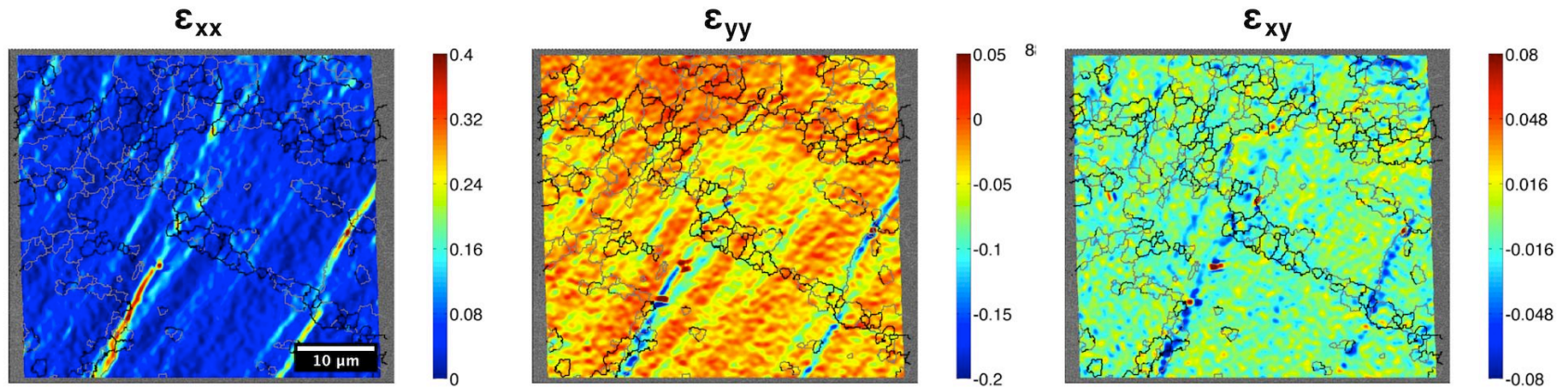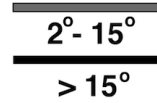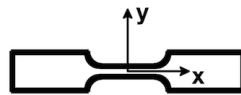
Figure 4.9: Strain fields for UFG-7 (a) at a macroscopic strain of 7.0% and UFG-8 (b) at a macroscopic strain of 3.0%.

4.3.1 Intragranular vs. Intergranular Strain Localization

Dislocation slip was particularly active in the supergrain microstructures present in every test except UFG-3, where ECAP processing led to the highest Schmid factor slip system being well aligned with the ECAP theoretical shear plane. In the supergrains, the average Schmid factor was 0.47 +/- 0.02, enabling dislocations to easily pass through the LAGBs. In each supergrain microstructure, slip occurred on planes whose mean surface trace was angled at 52.06° +/- 5.88° which is in good agreement with the angle of the theoretical ECAP shear plane of 45°. Orientations near $\{111\}\langle\overline{2}11\rangle$ were common in these supergrains and made up one band of the banded microstructures presented in UFG-2 and UFG-5. In these banded microstructures, both bands had similar Schmid factors, with the $\{001\}\langle110\rangle$ band having a slightly higher Schmid factor than the $\{111\}\langle\overline{2}11\rangle$ band (0.4868 +/- 0.0155 vs. 0.4562 +/- 0.0177). Yet slip was more active in the $\{111\}\langle\overline{2}11\rangle$ band. An explanation for this behavior is that the active slip system in this band was better aligned with the theoretical shear plane in the final ECAP pass, with a disorientation of 23.24° +/- 3.68° to this plane versus 39.79° +/- 5.94° for the active slip system in the $\{001\}\langle110\rangle$ bands. These results indicate that, even though the surrounding microstructure is different, slip systems well aligned with the theoretical shear plane in the last ECAP pass are very active in tension.

In many tests, dislocation slip occurring in supergrains and within microstructure bands intersected HAGBs as demonstrated in figures 4.6(a), 4.6(b), 4.7(b), 4.8(a), 4.9(a), and 4.9(b). At these points, dislocation pile-up occurred, resulting in high strain localization. Thus, these supergrains behaved similar to coarse-grained Al microstructures, where plastic deformation occurred primarily from dislocation slip and dislocation pile-up took place at HAGBs separating grains with poorly aligned slip systems.

In areas consisting of the classic ultrafine-grained microstructure composed of

ultrafine grains separated by primarily HAGBs, strain localization occurred almost exclusively at the HAGBs. The best example of this was in UFG-3. This microstructure was composed of small grains with an average grain size of 1.2 µm and the highest percentage of HAGBs of any of the microstructures investigated at 53%. While strain localization aligned with {111} plane traces did occur within some of the large grains in this FOV, that localization was lower in magnitude than the strain localization at grain boundaries. Even at the grain boundaries, much of the strain localization progressed in bands angled at near the ECAP theoretical shear plane. However, there are instances of shear strain localizing at grain boundaries perpendicular to the ECAP theoretical shear plane as shown in as shown in 4.10 for UFG-1 and UFG-3. In both microstructures, the grains at one side of the shear localization had a {001} plane parallel to the tension specimen face. This common orientation, as well as post-test surface observations with an optical microscope suggested that these boundaries represented the jagged boundaries between two original coarse parent grains. Thus, even in this ultrafine-grained microstructure, the orientation of initial parent coarse-grains still plays a role in strain localization.

In all tests, strain preferentially localized at HAGBs with surface trace angles near 26.6°. Although only 40% of the grain boundaries in all test FOVs were HAGB, HAGBs accounted for 66%, 58%, and 76% of the grain boundaries (by length) where strain localized in ϵ_{xx}, ϵ_{yy}, and ϵ_{xy} respectively (localization is defined as data points in the top 10% of each strain field). These grain boundaries with strain localization were also primarily angled near the predicted grain inclination angle of 26.6°. For all grain boundaries, the trace angle mode after application of a smoothing spline was 27.90° with an average absolute deviation from the mode of 31.40°. Strain localized primarily at these boundaries as well, except there was less spread in the data, with a trace angle mode after smoothing of 26.10°, 24.30°, and 24.31° and an average absolute deviation from the mode of 28.70°, 29.70°, and 26.80° for ϵ_{xx}, ϵ_{yy}, and ϵ_{xy} respectively.
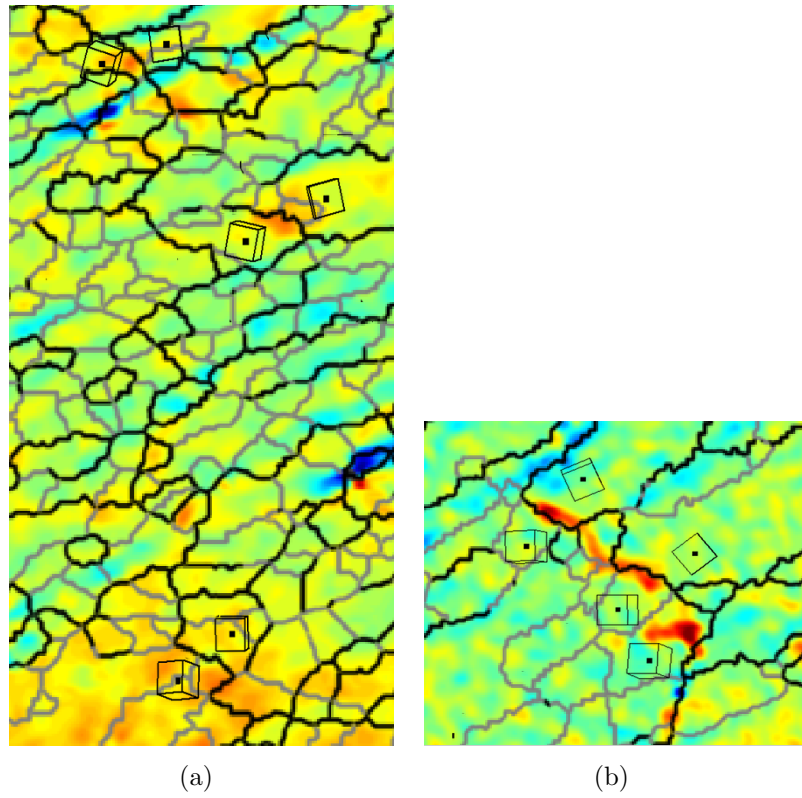
Figure 4.10: Diagrams of the crystalline orientation adjacent to high shear strain localization at HAGBs perpendicular to the grain elongation angle. The boxed region of UFG-1 in figure 4.6(a) is shown in (a) and the boxed region of UFG-3 in 4.7(a) is shown in (b). As demonstrated by the unit cell schematic, in each microstructure, crystalline orientations with a (001) plane parallel to the face of the tension sample are present on one side of the grain boundaries with the shear strain localization.

The mean strain in each test at HAGBs, LAGBs, and in grain interiors is presented in figure 4.11. As this figure demonstrates, the greatest axial strain occurred at HAGBs. In many of the tests, this is the result of incompatible slip systems in neighboring grains. In the banded microstructures of UFG-2 and UFG-5, this is due to the high strain localization that occurs at the HAGBs due to grain boundary sliding as discussed in subsection 4.3.3.

In four of the eight tests (UFG-2, UFG-4, UFG-5, and UFG-6), the largest magnitude transverse strain occurred at HAGBs. All of these tests contained continuous HAGBs that crossed the entire FOV and were angled close to the ECAP theoretical shear plane in the final pass. Noise may also contribute to this relationship not being observed in UFG-7 and UFG-8. Due to the low applied strain, low levels of strain localization occurred which allowed noise in the strain field to be at a similar magnitude to true strain localization.

In six of the eight tests, the largest magnitude shear strain occurred at the HAGBs, and in seven of these tests, the mean shear strain was negative. In UFG-6, UFG-7, and UFG-8, the mean shear strain was similar in grain interiors, LAGBs, and HAGBs due to the low levels of localization that occurred. In every strain component, UFG-4 exhibited the largest difference between strain localization at HAGBs versus LAGBs and grain interiors. This was a result of UFG-4 being primarily composed of two supergrains in which weak strain localization from dislocation slip occurred. These two supergrains were separated by a HAGB that bridged the FOV and at which strain primarily localized. As visible in figure 4.7(b) in the ϵ_{yy} strain field, the active slip system in the lower supergrain was angled to intersect this elongated HAGB. Thus significant dislocation pile-up occurred at this boundary and led to the high strain localization.
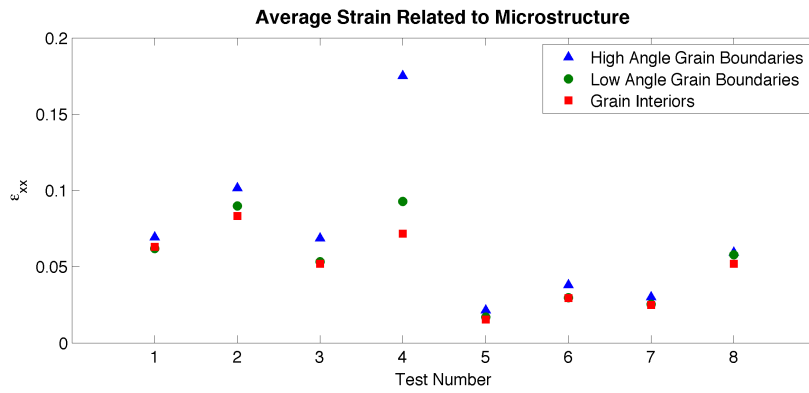
(a)

(b)

(c)
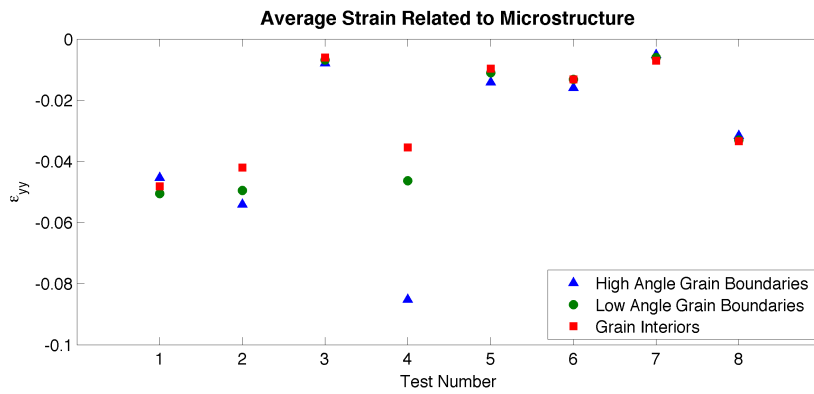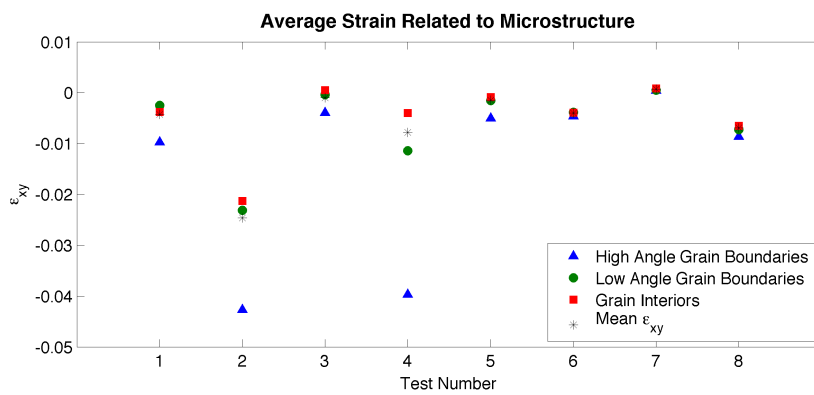
Figure 4.11: Mean ϵ_{xx} (a), ϵ_{yy} (b), and ϵ_{xy} (c) in each test FOV demonstrate that the largest magnitude mean strain typically occurs at HAGBs.

105

4.3.2 The Effect of the ECAP Theoretical Shear Plane on Strain Localization

The texture produced by ECAP processing had a strong effect on strain localization and was likely responsible for the reduced ductility of the material. As previously mentioned, dislocation slip occurred on slip planes with surface traces angled near 52.06° and intergranular strain localization primarily occurred at boundaries angled near 26.6°. Shear strain localization was strongly affected by the ECAP texture, with shear being of primarily one sign in all tests. This is best demonstrated in figure 4.11 (c) where in every test except for UFG-6, the mean shear strain is negative. Note that in the tests presented here, all FOVs are oriented so that the right side of the gage section exited the die first in the final ECAP pass. Thus, the ECAP theoretical shear plane is angled at 45° to the positive x-axis. This preferential shear direction is the result of significant plastic flow occurring in a similar direction. The effect of the strong texture can also be observed in the post test surface as shown in figure 4.12 for UFG-2. The surface deformation seen in this figure is aligned with the grain elongation axis and primarily angled between 15° and 52°. As tension was applied, shear occurred along shear bands and slip systems in the directions shown by the arrows in the figure. The high occurrence of both elongated grain boundaries and high Schmid factor slip systems being well aligned with the plane of maximum resolved shear stress in tension likely contributed to the early necking and catastrophic shear bands seen in these test samples that limited their ductility.

4.3.3 Banded Microstructure Strain Localization and Deformation Mechanisms

Unique strain localization behavior and grain boundary sliding were observed at the HAGBs separating microstructure bands. Due to the very high misorientation of the grain boundaries separating microstructure bands, slip was not able to transfer
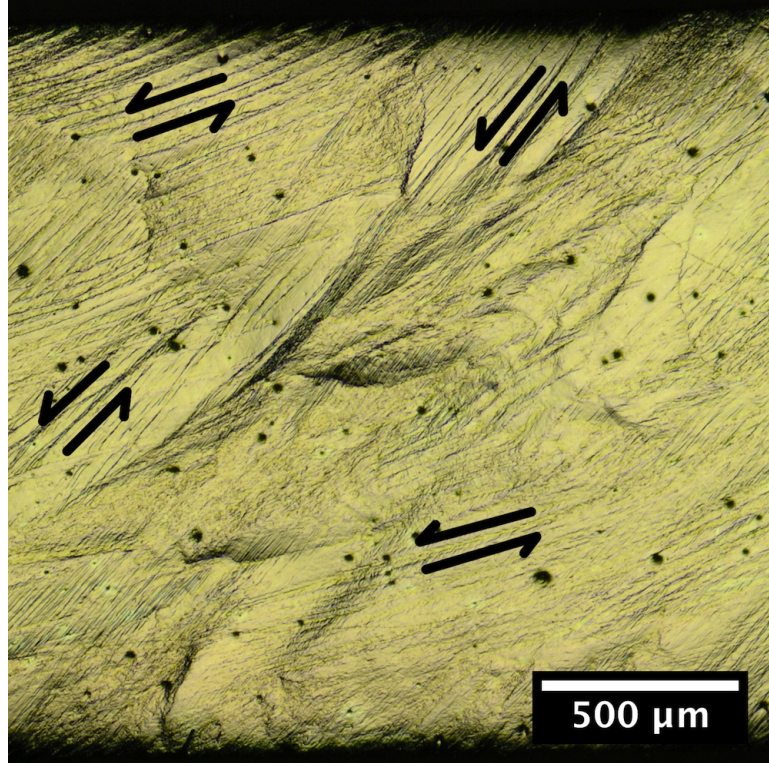
Figure 4.12: Post-test optical microscopy image of surface deformation of test sample UFG-2 revealing surface deformation angled at between 15° and 52° to the tension direction (horizontal).

easily into the neighboring bands. Instead, as in coarse grained microstructures, high strain localization generally occurred at the HAGBs where they were intersected by dislocation slip. Using UFG-2 as a model microstructure, the strain localization within microstructure bands and at points within 500 nm of HAGBs separating bands can be compared. This is shown in figure 4.13. The mean strain in each microstructure band shown in figure 4.13(a) and 4.13(b) and the boundaries between bands as shown in figure 4.13(c) is contained in the table in figure 4.13(d). The greatest mean strain, for every strain component, occurred at the HAGBs separating microstructure bands. In the shear strain field, the shear strain at these boundaries was approximately double the mean shear strain that occurred within either microstructure band. While transverse strain was the highest at the microstructure band boundaries, the mean value within the microstructure band with near $\{111\}\langle\overline{2}11\rangle$ orientation, Band "A",

approached the value at the boundaries at the end of the test. This acts to confirm the highly active dislocation slip in the microstructure band, which has a high Schmid factor slip system aligned favorably with the ECAP theoretical shear plane in the final pass.

Location	Mean ϵ_{xx}	Mean ϵ_{yy}	Mean ϵ_{xy}
Band "A" (a)	0.0883	-0.0516	-0.0234
Band "B" (b)	0.0777	-0.0337	-0.0149
Band Boundaries (c)	0.1035	-0.0541	-0.0447

(d)
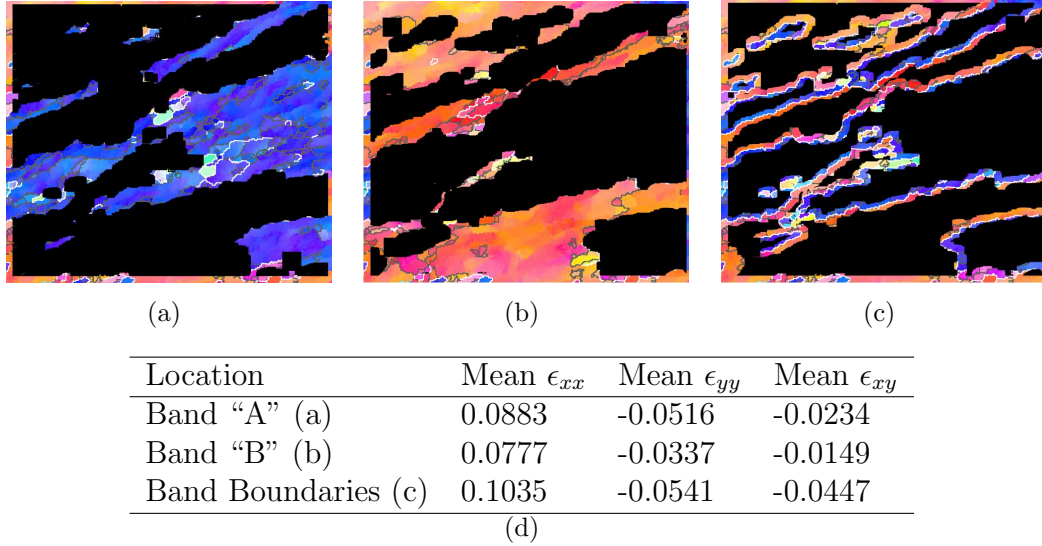
Figure 4.13: Inverse pole figure maps in which only microstructure band "A" (a), microstructure band "B" (b), and the boundary between microstructure bands (c) are shown. The table in (d) contains the mean strain for each of these regions and demonstrates that the highest magnitude strains are positioned at the boundaries between bands.

In both banded microstructures investigated, shear strain localized almost exclusively at the HAGBs separating microstructure bands. As previously mentioned, these HAGBs had an average misorientation of 55.26° +/- 2.62° in UFG-2 and 48.77° +/- 5.39° in UFG-5. In UFG-2, as shown in figure 4.6(b), at a macroscopic strain of 9%, sharp shear strain localization on the order of 30% was observed along the grain boundaries separating the microstructure bands with nearly zero shear strain localization within the grains. Much lower strain localization was observed in UFG-5 due to necking occurring at the end of the gage section, but still at a macroscopic strain of 14%, which was primarily localized within a narrow neck, shear strain localization of 3% was observed along the grain boundaries. This is much lower than the shear

strain in UFG-2 but, as with UFG-2, the shear strain is near zero everywhere else as shown in figure 4.8(a).

Grain boundary sliding was evident at the HAGBs separating microstructure bands, and led to shear offsets of up to 500 nm. The largest instance of grain boundary sliding in test specimen UFG-2 occurred in the black box in the ε_{xy} strain field in figure 4.6(b) and will be discussed here. The speckle pattern in this area is shown in figure 4.14 at three images: the reference (unloaded), intermediate, and final deformed image. Figures 4.14(a), 4.14(b), and 4.14(c) show the speckle pattern in that area in the reference, intermediate, and final deformed images. Figures 4.14(d) and 4.14(e) show the relative displacement of the bottom circle with respect to the top circle in the speckle pattern images in figures 4.14(a) – 4.14(c). Figure 4.14(f) shows the angle of displacement of the lower white circle with respect to the upper white circle. At image 20, it is apparent that shear displacements initialized at the grain boundary. The displacement angle was random until plastic deformation occurred around image 20, at which point it stabilized near 30° which was also the angle of the grain boundary trace at this location. The displacements appear to be unaffected by the global strain or strain rate in this room temperature test. These results, which have been verified at microstructure bands in additional test samples, confirm that localized shear was occurring parallel to the grain boundary plane as a result of grain boundary sliding.

The tests performed here are subject to the free boundary condition as discussed in [19], yet grain boundary sliding occurred in-plane as well as out-of-plane, unlike the indentation work where the grains were forced out of the surface by the penetration of the indenter [30, 31]. Out of plane grain boundary sliding was also observed at microstructure band boundaries as ledges in the surface. It is likely that the underlying microstructure played a role in the sliding behavior, as there was no significant difference between the active slip systems in adjacent grains for out-of-plane and in-plane

grain boundary sliding.

While grain boundary sliding was an active deformation mechanism, it only occurred at 40% of the microstructure band boundaries. Dislocation slip also contributed to shear strain localization. At many of the boundaries between microstructure bands that showed shear localization, abrupt shear offsets at the grain boundaries were not observed. Instead, the shear displacements occurred over a wider area centered about the grain boundary, with incremental offsets of speckles within the shear region. This suggests that grain boundary sliding was not active in this region and instead dislocation slip occurred near the grain boundary.

Adjacent microstructure bands were highly misoriented, however the active slip systems in adjacent bands were moderately well aligned. The active slip systems in the microstructure bands adjacent to the grain boundary sliding event in UFG-2 had an average compatibility factor m' of 0.54 +/- 0.09, indicating moderate alignment of the slip systems in these adjacent areas. Similar geometric compatibility values of 0.56 +/- 0.08 were measured in UFG-5. Additionally, the slip plane traces of these active slip systems were angled less than approximately 20° to the grain boundary traces. Numerous models have proposed that dislocations can be absorbed into the grain boundaries and decomposed into grain boundary glide and climb dislocations [3, 18, 157]. The shallow intersection angle here would result in a large glide component of the absorbed dislocations, encouraging low temperature grain boundary sliding through the motion of these dislocations. The results indicate that conditions conducive for grain boundary sliding are elongated, very high misorientation HAGBs separating grains with moderately well-aligned, highest Schmid factor slip systems that have shallow intersection angles with the grain boundaries.
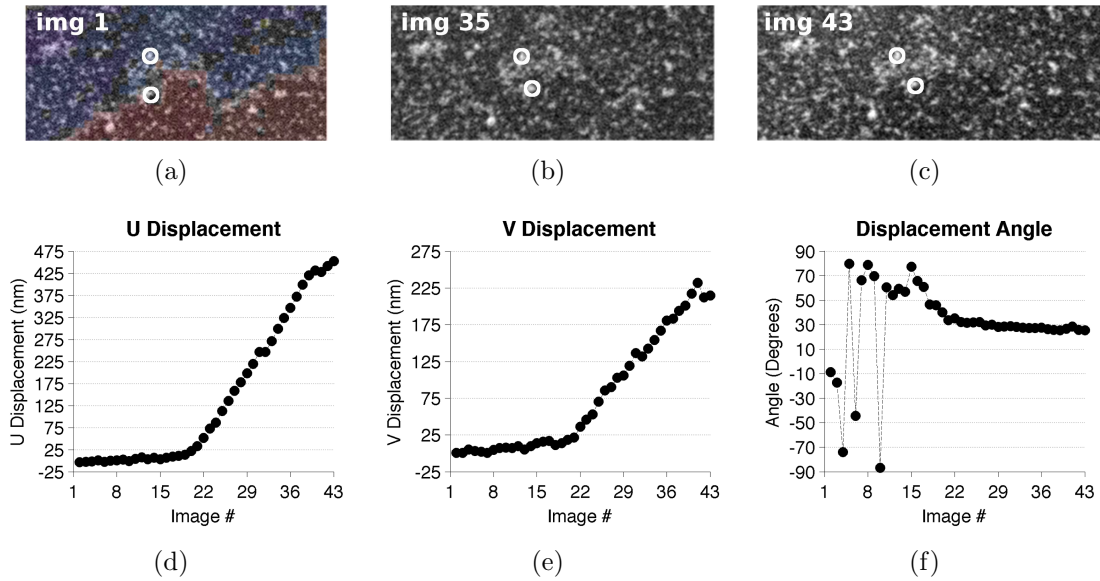
Figure 4.14: Evidence of grain boundary sliding at the boundary between deformation bands contained within the black box in figure 4.6(b). (a), (b), and (c) show the speckle pattern in that area in the reference, intermediate, and final deformed images. (d) and (e) show the relative displacement of the bottom circle with respect to the top circle in the speckle pattern images in (a) – (c). (f) shows the angle from horizontal of the bottom circles displacement relative to the top circle. A sharp offset occurs in the speckle pattern images and shear displacement at the angle of the grain boundary occurs starting at image #20. The markers are larger than the root mean square measurement error.

4.4 Conclusions

This work presents the local deformation response of eight in-SEM tension tests on ECAP-processed UFG 99.99% pure Al. Deformation and strain localization at the length scale of the microstructure were investigated using a custom experimental approach combining SEM and DIC. Full-field strain localization within individual ultrafine grains, and its relation to the underlying microstructure, was quantified. The following conclusions have been reached:

1. The fields of view investigated in this work, and that primarily make up the post-ECAP processing microstructure, consist of supergrains (areas of ultrafine grains separated by LAGBs), microstructure bands, and ultrafine-grained areas.

2. Supergrains behave similarly to coarse-grained material, with dislocation slip occurring on the slip system best aligned with the theoretical shear plane of the last ECAP pass, and typically possessing the highest Schmid factor.

3. The greatest strain localization occurs at HAGBs, especially those separating distinct microstructure regions, such as microstructure bands, and those angled at near 26.6°.

4. Shear strain localization is strongly influenced by the grain inclination angle, and will be primarily of one sign depending on the mean angle of the grain boundaries in the test FOV.

5. The propensity for grain boundaries and high-Schmid factor slip systems to be angled near the plane of maximum shear stress in tension likely contributes to the early, narrow necking seen in these test samples.

6. In banded microstructures, shear strains as high as 30% occurred at the HAGBs separating bands. The geometric compatibility of the active slip systems adjacent to the HAGBs separating bands was approximately 0.55.

7. Sharp shear offsets of up to 500 nm, indicative of grain boundary sliding, were also observed at the interface between microstructure bands. Grain boundary sliding was only observed at HAGBs separating microstructure bands and was present at 40% of these HAGBs.

CHAPTER V

Elevated Temperature Experiments

This chapter describes the characterization of microstructural features responsible for the macroscopic strain rate sensitivity of UFG Al. Elevated temperature strain rate jump tension tests were performed at 200 °C and strain rates of 2.5 x 10^{-5} s^{-1} and 3 x 10^{-3} s^{-1}, with strain steps of 2.5%. Four distinct microstructural regions were investigated, as presented in section 5.1. They consist of approximately the same size FOVs and include supergrains, microstructure bands, and ultrafine-grained regions. The experiments detailed in this chapter follow the general experimental procedure outlined in section 2.3, with specifics for each test detailed in section 5.2. Section 5.3 presents the experimental results, starting with general observations and comparisons between the macroscopic response of the material in this work and in previous works. Additionally, comparisons between strain rate sensitivity in the room temperature strain rate jump tests (chapter IV) and elevated temperature tests (this chapter) are discussed. Subsection 5.3.1 examines differences in strain localization at low strain rate versus high strain rate. The surface appearance after elevated temperature experiments is much different than after room temperature experiments. Images of the post test gage sections and analysis of their appearance is presented in subsection 5.3.2. Section 5.4 then summarizes the main findings of this chapter.

5.1 Microstructures Investigated

The FOVs investigated in these elevated temperature experiments were selected to contain microstructure features similar to those investigated at room temperature. Microstructure details for the four FOVs are provided in table 5.1 and inverse pole figure maps are shown in figure 5.1. The FOVs denoted "SRS-1" and "SRS-2" are composed primarily of ultrafine grains separated by a large percentage of HAGBs. SRS-2 is similar to UFG-3 (shown in figure 4.1(c)) in that they both contain a jagged boundary between original parent coarse grains. The FOV "SRS-3" is composed of microstructure bands with similar orientations and grain boundary misorientations as the banded microstructures investigated in UFG-2 and UFG-5 in chapter IV. The FOV "SRS-4" consists of a large supergrain region and a region of ultrafine-grains with similar orientations as the supergrain region. Note that three tension specimens were loaded in these experiments. The FOVs SRS-1 and SRS-2 are from two separate tension specimens. The FOVs SRS-3 and SRS-4 are from the same tensile specimen with the FOVs spaced approximately 200 µm apart.

Microstructure Identifier	FOV Size (µm x µm)	Avg. Grain Size (µm)	% HAGBs	Mode of Grain Boundary Trace Angle (°)
SRS-1	45 x 38.8	1.97	48	27.2° +/- 25.1°
SRS-2	46.5 x 40.1	1.92	60	17.0° +/- 23.3°
SRS-3	42.7 x 36.9	3.11	74	22.4° +/- 14.4°
SRS-4	42.7 x 36.9	2.82	61	28.8° +/- 21.4°

Table 5.1: Microstructural characteristics for the four fields of view investigated.

The FOVs have high percentages of HAGBs. This is particularly true in SRS-2, SRS-3, and SRS-4, which have a greater percentage of HAGBs than any of the room temperature FOVs. As in the room temperature tests, all of the FOVs here have similar inclination of the grain boundaries resulting from ECAP processing and there are large areas of grains with orientations near $\{111\}\langle\bar{2}11\rangle$, which appears as purple in the inverse pole figure maps. These common features lead us to expect similar
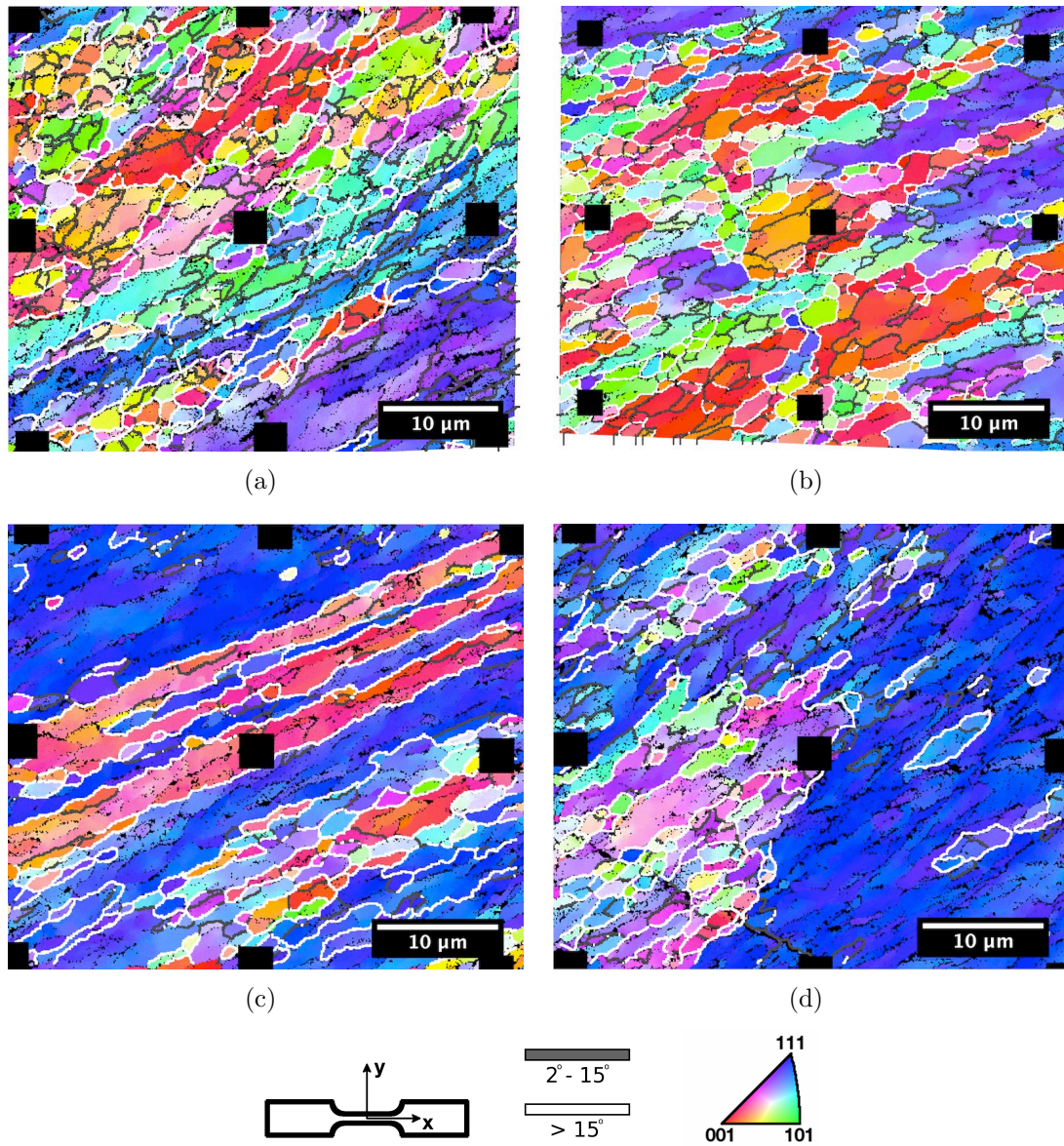
Figure 5.1: Inverse pole figure maps of the fields of view investigated in the elevated temperature strain rate jump tension tests. Areas (a) SRS-1 and (b) SRS-2, are composed primarily of ultra-fine grains, while (c) SRS-3 is composed of microstructure bands and (d) SRS-4 contains a large supergrain region and a large area of ultrafine grains.

dislocation slip angled at near 45° to horizontal within supergrains and larger grains and the highest magnitude strain localization to occur at HAGBs.

5.2   Experimental Procedure

Elevated temperature experiments were performed at strain rates that jumped between 2.5 x 10^{-5} s^{-1} and 3 x 10^{-3} s^{-1}. Note that these were not instantaneous jump tests, as the displacement was held constant between strain rates to capture images for DIC. Initial loading occurred at 2.5 x 10^{-5} s^{-1} to a strain of 2.5% to ensure the microstructure within the FOV had plastically deformed. Following this, the specimens were loaded at alternating strain rates, starting with the high strain rate. The strain rate was alternated after strain steps of 2.5% until a final macroscopic strain of 17.5% was achieved. Four load steps are presented out to a macroscopic strain of 12.5%. After this, localization was very small and not measurable in the majority of the remaining load steps. An accelerating voltage of 20 kV, dwell time of 30 µs, and single image scan were utilized in each test. A beam current of 0.31 nA was used for SRS-2, SRS-3, and SRS-4, while a beam current of 0.16 nA was used for SRS-1 as a new filament was installed in the SEM and this current provided the best images. Images of 2048 x 1768 pixels were utilized in each test.

DIC was performed utilizing a step size of 3 pixels and a subset size containing between 3 x 3 speckles and 5 x 5 speckles on average. Surprisingly, a 3 pixel step size allowed for improved correlation in these tests. It is probable that this step size, instead of a step size of 1 pixel, allowed for many pixels undergoing very large deformation to be skipped over. This prevented correlation failure in these high deformation areas, which can lead to failed correlation of the entire image. DIC was performed twice, with the first analysis correlating all deformed images to the single unloaded reference image. The second analysis correlated the images incrementally to measure strain localization unique to each load step. It is possible that we could

have subtracted the strain from the previous image of the continuous image set to obtain the incremental strain. But, this would have lead to greater noise than if a new deformed reference image was used for each load step as was done in the incremental DIC. Note that using this incremental correlation aligned the strain fields with a deformed image versus the reference image and EBSD FOV. Thus, the first continuous DIC analysis was used to relate the incrementally deformed image data back to the single unloaded reference image and corresponding EBSD FOV. Following distortion correction, strain was calculated utilizing the same procedure outlined in section 4.2.

At elevated temperatures, stress relaxation occurred at a much faster rate and did not level off as it did in room temperature experiments. Thus, single image scans were used in these experiments to avoid the blurring that exists in integrated scans. As a result, horizontal displacement shifts as mentioned in [87, 169, 170] existed in the DIC strain fields and caused high magnitude strain at the edges of the shifts. A code was written to recognize these shifts and remove the data so that it did not contaminate the accurate measurements. These shifts were not as problematic as expected and were only apparent in SRS-1 data. This removed data appears as blank lines in the SRS-1 strain fields shown later.

5.3 Experimental Results and Discussion

The elevated temperature macroscopic response of the UFG Al was significantly different than the room temperature response, with a lower yield strength and 3x greater strain rate sensitivity. The yield strength of these elevated temperature tensile specimens was approximately 64% of the room temperature yield strength (59.1 +/- 6.9 MPa vs. 93.0 +/- 11.2 MPa). Figure 5.2 shows a comparison between the stress-strain curve for strain rate jump tests at room temperature and elevated temperature. The room temperature stress-strain curve does not reveal work hardening for any load

steps except initial loading, suggesting that necking occurred and plastic deformation localized at the necked region. In fact, the room temperature specimen (UFG-5) failed by a narrow neck that formed shortly after the macroscopic yield strength was reached. In the elevated temperature specimen (SRS-3/4), work hardening was apparent at all low strain rate load steps except the final step. Specimen SRS-3/4 failed by a large macroscopic shear band that was observed after the fourth load step. The shear band appearance remained approximately unchanged in the following low strain rate load step, which still displayed work hardening. Offset at the band increased sharply in the next high strain rate load step, after which work hardening was no longer apparent even at the low strain rate. Strain localization occurred predominately at the shear band. Note that at the end of each test, the load was removed and the specimens were not allowed to fracture. The elevated temperature strain rate sensitivity was m = 0.057 +/- 0.008, which is over three times greater than the room temperature value of m = 0.018 +/- 0.002. Note that these are the steady state strain rate sensitivity values and would be larger if instantaneous strain rate sensitivity was calculated, or if the strain rate was changed instantaneously instead of following a period of constant displacement.

5.3.1 Strain Localization at Low vs. High Strain Rates

Incremental strain localization in each strain step was measured. Strain fields are shown in figures 5.3 – 5.6 for each test FOV at load steps of 2.5% - 5%, 5% - 7.5%, 7.5% - 10%, and 10% - 12.5%. This coincides to two high strain rate load steps and two low strain rate load steps, as shown in figure 5.2. In figures 5.3 – 5.6, the bottom plot shows the mean incremental strain for the entire FOV incurred during each load step. The mean strain response of SRS-2 (figure 5.4) dropped with each load increment, while in SRS-1, SRS-3, and SRS-4, the mean strain increased with each low strain rate load step. In each test, the mean strain in the first two load
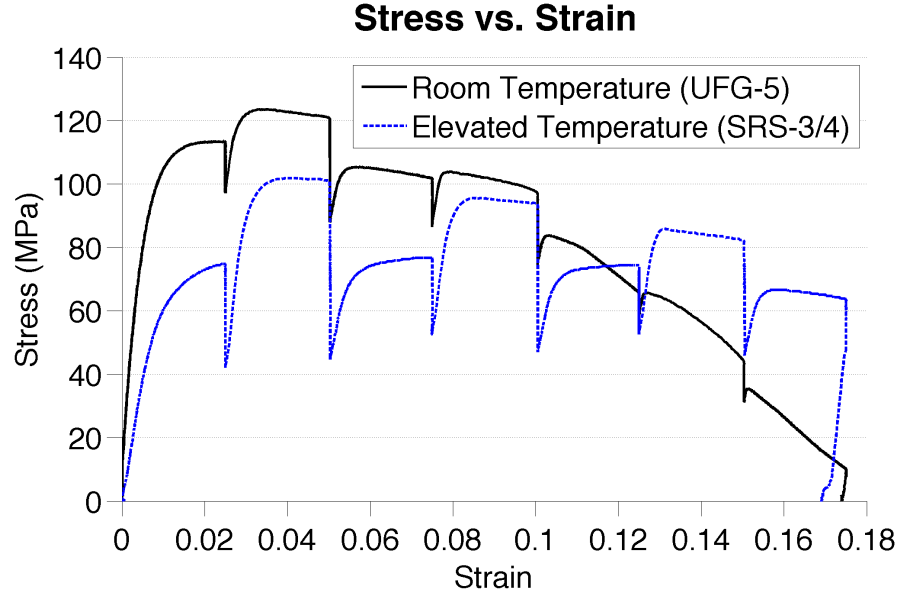
Stress vs. Strain

Figure 5.2: Macroscopic stress-strain curve calculated from the load cell data and grip displacement displaying differences in the strain rate sensitivity in the room temperature strain rate jump test in UFG-5 and the elevated temperature strain rate jump test in SRS-3/4. Work hardening is not apparent in the room temperature experiment except for in the initial load step. Work hardening is present in all low strain rate load steps of the elevated temperature experiments except the last.

steps was near the applied strain of 2.5%. After the second load step, the mean strain dropped to approximately 1% as a result of strain localization preferentially occurring at shear bands that formed after the second load step.

The strain localization at elevated temperatures has a similar configuration as room temperature localization. In all elevated temperature tests where intragranular strain localization was apparent, it primarily occurred on slip systems with surface traces angled near 45° to the positive x-axis, as with the room temperature tests. Also, the highest magnitude strain localization typically occurred at or very near HAGBs angled near to the ECAP theoretical shear plane in the final pass. Additionally, for the banded microstructure of SRS-3, shear strain localization occurred exclusively at the boundaries separating microstructure bands.

Quantitative measures of mean strain localization in each load step were computed
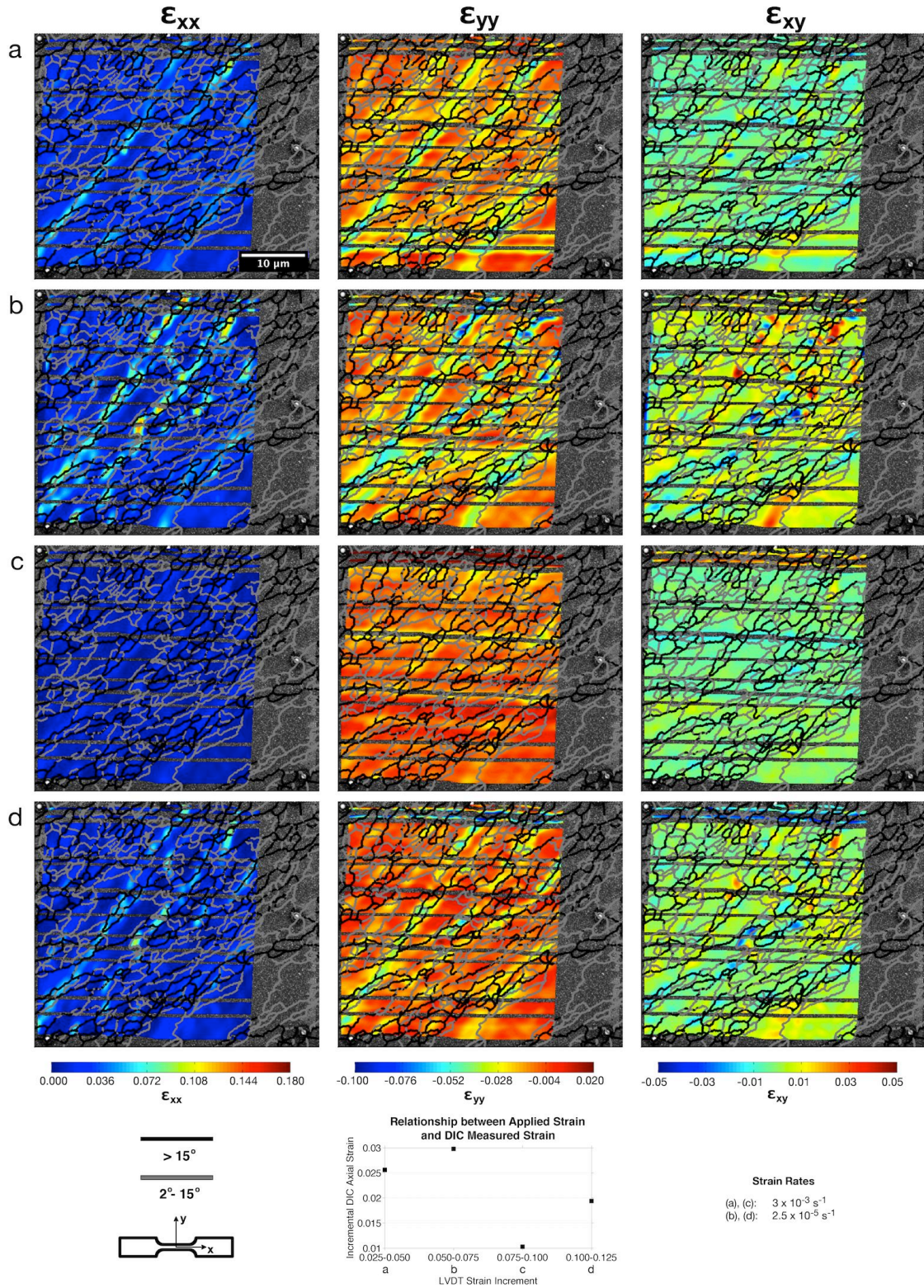
Figure 5.3: Strain fields for SRS-1. (a) and (c) show the incremental strain fields for a strain rate of 3 x 10⁻³ s⁻¹. (b) and (d) show the incremental strain fields for a strain rate of 2.5 x 10⁻⁵ s⁻¹.
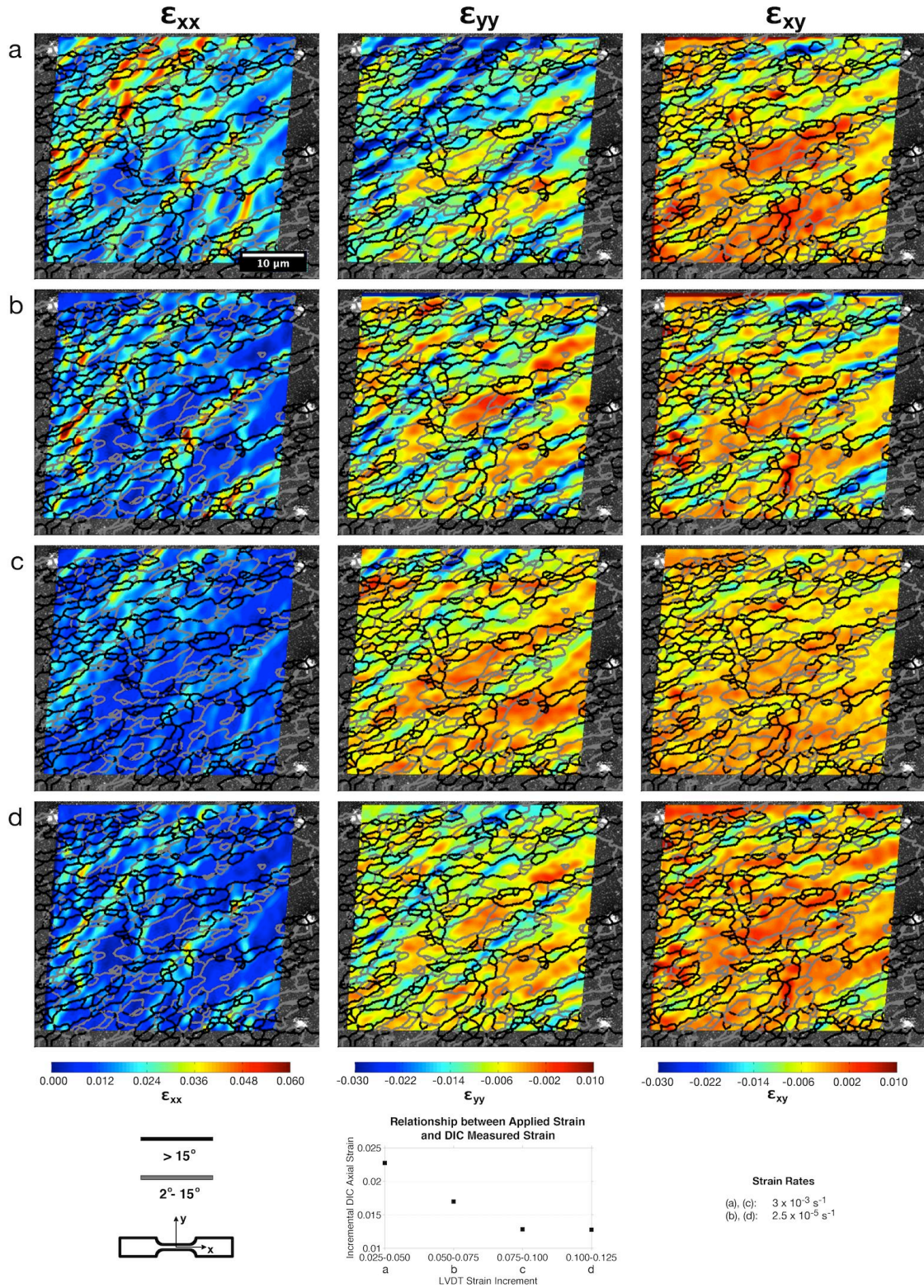
Figure 5.4: Strain fields for SRS-2. (a) and (c) show the incremental strain fields for a strain rate of 3 x 10⁻³ s⁻¹. (b) and (d) show the incremental strain fields for a strain rate of 2.5 x 10⁻⁵ s⁻¹.
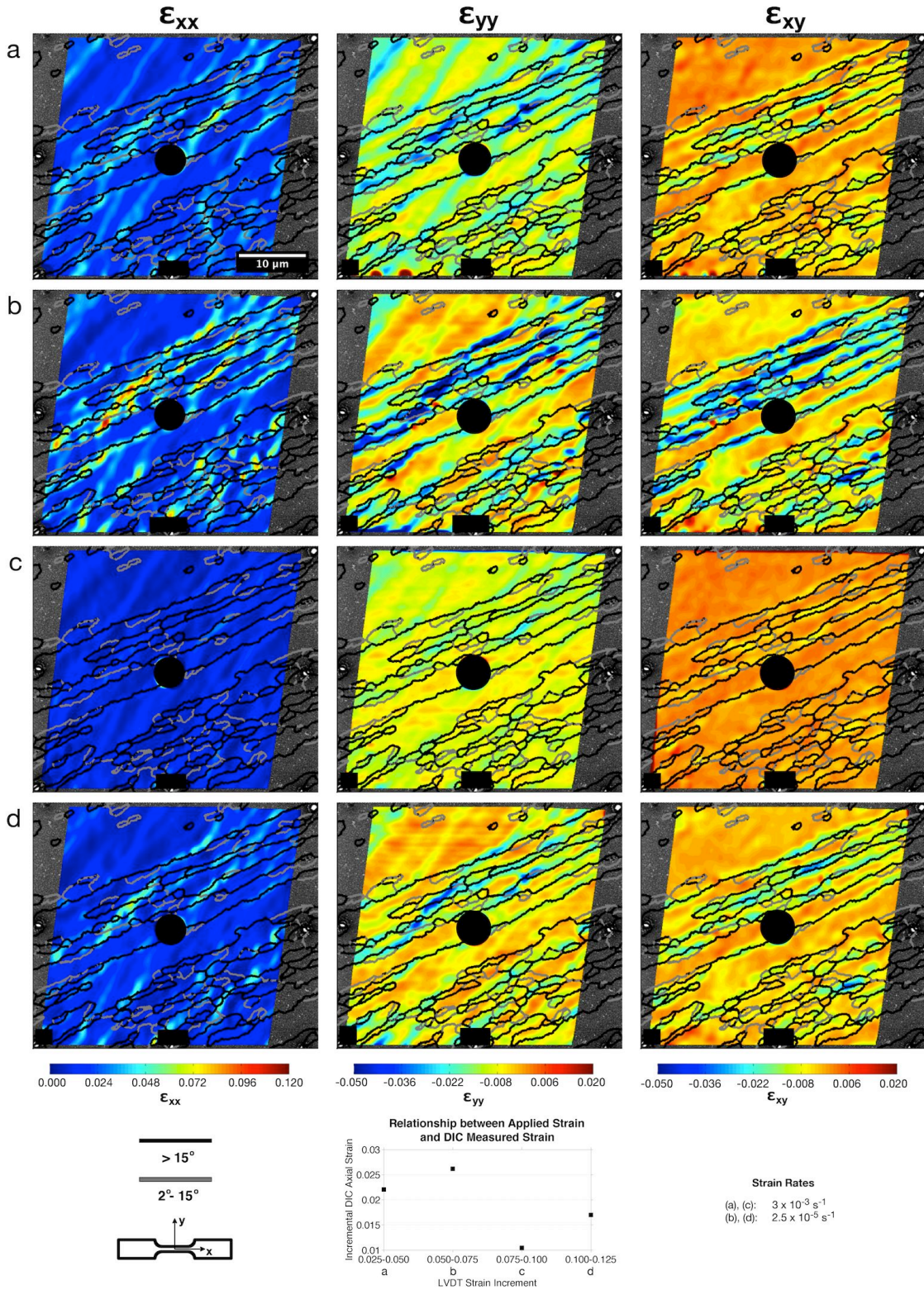
Figure 5.5: Strain fields for SRS-3. (a) and (c) show the incremental strain fields for a strain rate of 3 x 10^{-3} s^{-1}. (b) and (d) show the incremental strain fields for a strain rate of 2.5 x 10^{-5} s^{-1}. The black areas cover failed correlation resulting from the Pt markers.

123
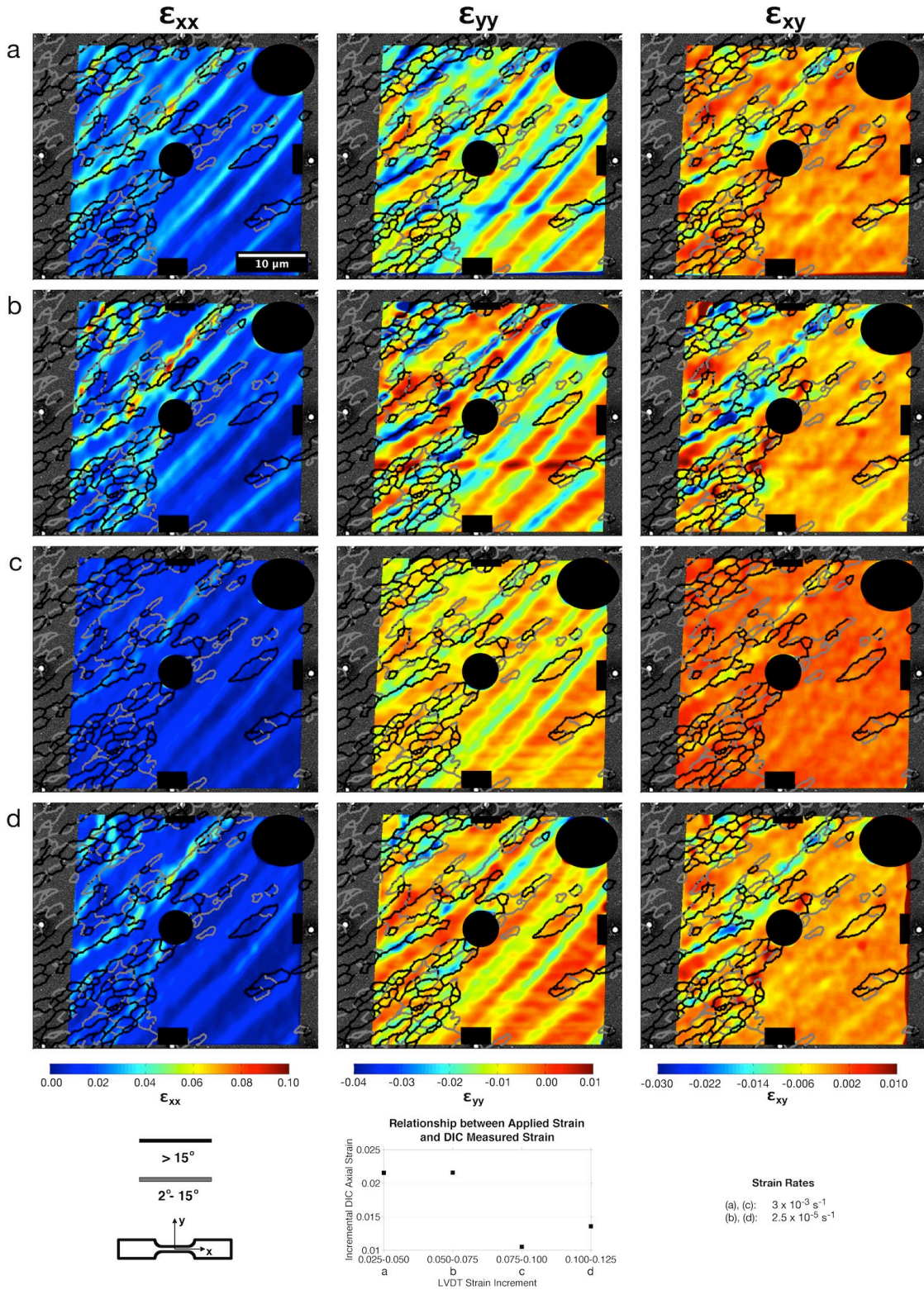
Figure 5.6: Strain fields for SRS-4. (a) and (c) show the incremental strain fields for a strain rate of 3 x 10⁻³ s⁻¹. (b) and (d) show the incremental strain fields for a strain rate of 2.5 x 10⁻⁵ s⁻¹. The black areas cover failed correlation resulting from the Pt markers.

and related to the underlying microstructure as follows: first, areas of visible strain localization were selected from the strain fields at each load step using the image manipulation program Gimp. Data points were selected if localization was present in at least one load step. Manual data selection was used in place of automated selection of data over a set strain cutoff value, to avoid selecting areas of high strain resulting from interpolation between DIC strain data points. This is demonstrated in figure 5.7, where utilizing a strain cutoff value including the strain localization in circle "A" in figure 5.7(a) would have selected the data shown in figure 5.7(b). This selected data includes the data points between the two bands of strain localization shown in circle "B". An additional benefit of manual strain selection is the ease in visibly recognizing and removing noise. The highlighted image files were imported into Matlab, converted to logical arrays with the same dimensions as the strain arrays, and used to select the strain data. To avoid selecting intragranular data points for strain localization at grain boundaries and vice-versa, the highlighted lines in the manipulated image files were eroded down to lines a single data point thick, and grain boundaries were dilated to accommodate small levels of misalignment. The data resulting from this procedure is shown in figures 5.8, 5.9, and 5.10 and discussed in the following paragraphs. In these figures, the top plots display the mean incremental strain for each global strain increment. The bar graphs demonstrate the change in mean incremental strain that occurs when changing strain rate. Note that this discussion characterizes grain boundaries by their misorientation. Other microstructure characteristics such as the difference in adjacent grain size, angle between highest Schmid factor slip directions and plane normals, and crystalline orientation were also investigated, but no relationships to strain rate sensitivity were found.

Grain boundaries, particularly HAGBs, exhibit the greatest strain rate sensitivity, with the mean incremental strain decreasing (increasing) when going from a low to high strain rate (high to low strain rate). At high strain rate (LVDT strain increments
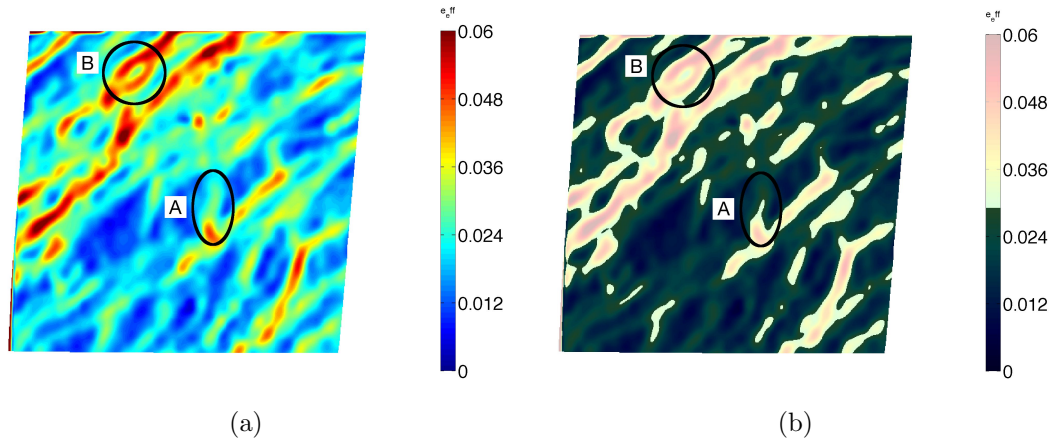
Figure 5.7: Challenges with selecting a cutoff value for selecting areas of strain localization. Selecting a cutoff value suitable for the strain localization in (a) in the area circled in circle A would result in the highlighted strain field in (b) which would include the area between strain localization in circle B.

from 0.025 - 0.050 and 0.075 - 0.100) the incremental mean strain at grain boundaries and within grains were of similar magnitudes as shown by the closely grouped markers in many of the top plots of figures 5.8 – 5.10. At low strain rate, intragranular localization increased; but not to the same level as localization at HAGBs, which could double in magnitude.

Boundaries between microstructure bands showed the greatest strain rate sensitivity and supergrains, which deformed primarily by dislocation slip, were the least sensitive to strain rate. For example, in SRS-3 which contained microstructure bands, the grain boundary incremental strain always increased when going from high to low strain rate and decreased when going from low to high strain rate. The mean incremental strain magnitude at grain boundaries was also always greater than in grain interiors (supergrains) for each strain component and at every load step. Additionally, the magnitude of the change in the incremental strain was always greater at the grain boundaries than in the grain interiors.

Dislocation slip, active in supergrains and often apparent in ϵ_{yy} limited strain rate sensitivity. In SRS-3 and SRS-4, which both contained supergrains, dislocation
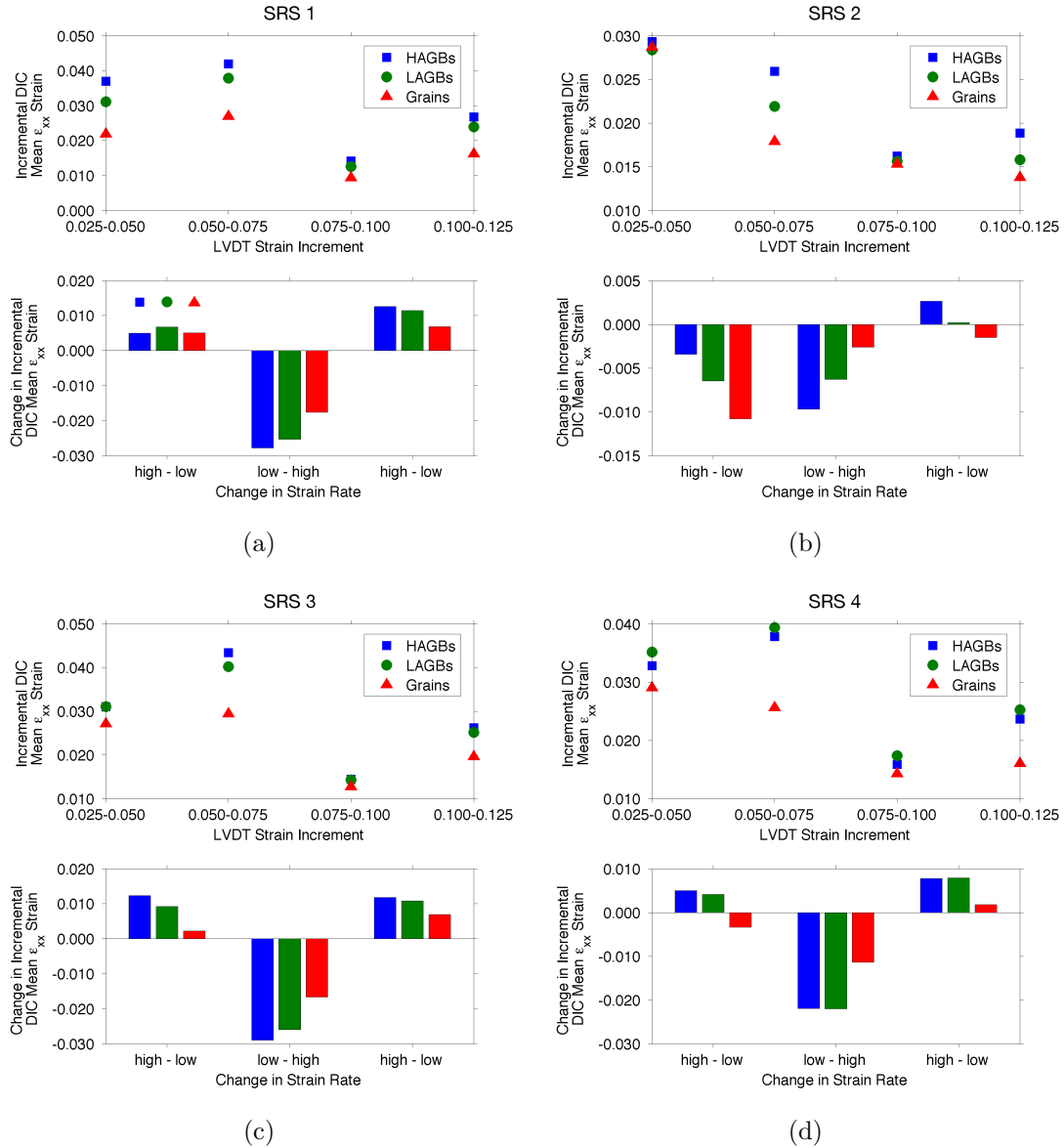
Figure 5.8: Incremental axial ε_{xx} strain at each load step for (a) SRS-1, (b) SRS-2, (c) SRS-3, and (d) SRS-4. The top plots demonstrate the incremental strain at HAGBs, LAGBs, and grain interiors (Grains) for each load step. The bottom bar graphs show how much the mean incremental strain changed when switching between strain rates. The colors of the data points in the top plots match the colors of the bars in the lower bar graphs. In general the greatest strain rate sensitivity is apparent at HAGBs. The mean strain at high strain rates is, in general, similar for grain boundaries with within grains.
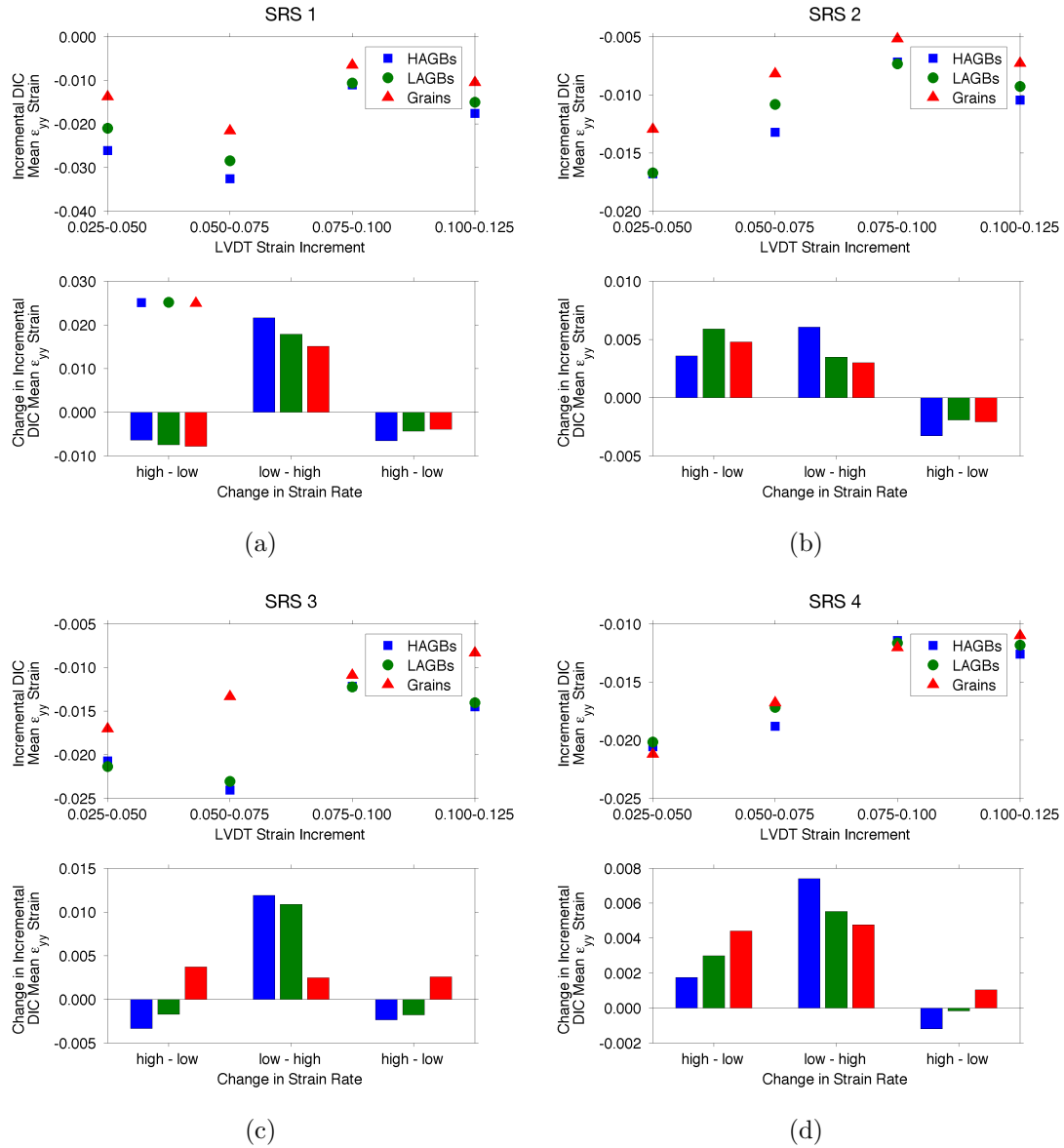
Figure 5.9: Incremental axial ε_{yy} strain at each load step for (a) SRS-1, (b) SRS-2, (c) SRS-3, and (d) SRS-4. In general the greatest strain rate sensitivity is apparent at HAGBs. The mean strain within grains from dislocation slip shows the least strain rate sensitivity and typically decreases in magnitude throughout the tests.
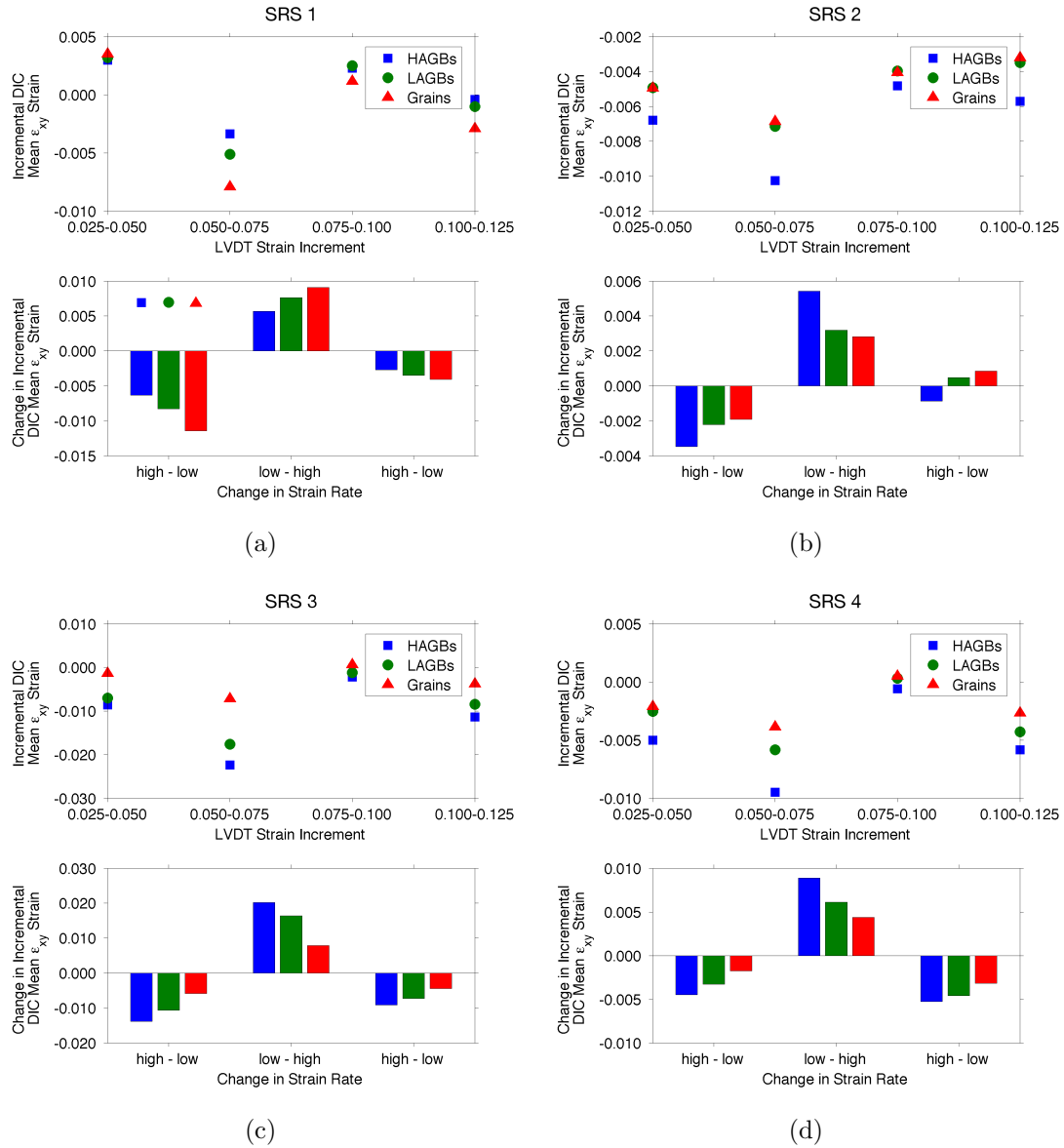
Figure 5.10: Incremental axial ε_{xy} strain at each load step for (a) SRS-1, (b) SRS-2, (c) SRS-3, and (d) SRS-4. In general the greatest strain rate sensitivity is apparent at HAGBs. Grain interiors show the greatest strain rate sensitivity in SRS-1 due to peaks that occur within larger grains.

slip led to strain localization in ϵ_{yy} that continually decreased in magnitude and was minimally affected by strain rate. The limited strain rate sensitivity of dislocation slip in the supergrains also limited the strain rate sensitivity at the grain boundaries in SRS-4. Many of the grain boundaries were elongated and parallel to the traces of the slip planes active in the neighboring supergrain. Since plastic deformation occurred on these grain boundaries to accommodate the slip which was primarily apparent in ϵ_{yy} and which shows little strain rate sensitivity, the strain rate sensitivity of the grain boundaries and grain interiors were similar and small in transverse strain localization. Thus, the limited strain rate sensitivity in supergrains can also limit strain rate sensitivity at neighboring grain boundaries.

These results provide quantitative evidence that grain boundaries, particularly HAGBs are responsible for the enhanced strain rate sensitivity of UFG Al. The fact that an elevated temperature and low strain rate was required to see this enhanced strain rate sensitivity also suggests that this behavior is the result of grain boundary diffusion deformation mechanisms as proposed by others [29, 31, 69, 98, 100, 119, 146, 150, 184, 194]. At high strain rates, diffusion is limited at the grain boundaries, causing lower strain localization with magnitudes near the same level as dislocation slip. Dislocation pileup likely contributes to high strain rate grain boundary strain localization. At low strain rates, diffusion deformation mechanisms are more active at the grain boundaries, allowing for significant strain localization. Dislocation slip originating/terminating at the grain boundaries acts to accommodate some of the large plastic deformation arising from diffusion.

5.3.2 Elevated Temperature Shear Bands

Enhanced diffusion at low strain rates and elevated temperatures improved ductility through the recovery of dislocations, which allowed plastic deformation to be spread over a wider area of the gage section. This is shown in figure 5.11 where plas-

tic deformation is visible in the elevated temperature gage sections (figures 5.11(b) – 5.11(d)), but not the room temperature gage section (5.11(a)). Still, elevated temperature gage sections (shown in figures 5.11(b) – 5.11(d)) all exhibit shear banding as opposed to the necking present in the room temperature gage section (figure 5.11(a)). Due to the shear bands playing a much larger role at elevated temperature, and growing at a faster rate at high strain rate, we conclude that these bands are the result of enhanced dislocation slip. Cooperative diffusion along grain boundaries which are primarily angled near the angle of the shear bands is likely also a contributing factor. SRS-1 shows a narrow shear band with no observable necking, while SRS-2 and SRS-3/4 show a combination of necking and wider shear banding. The cause of this is not known for SRS-2, but for SRS-3/4, the wider shear band likely resulted from the additional localized deformation at the right of the gage section. In each elevated temperature test, shear localization was observable on the surface during the second high strain rate load step from 7.5% to 10% macroscopic strain.

The room temperature (specimen UFG-5) gage section, figure 5.11(a), shows a narrow neck which formed during the second low strain rate load step. The subsequent high strain rate load step from 7.5% to 10% strain resulted in significant narrowing of the gage section in the necked region. This explains the very small increase in flow stress that occurred upon this high strain rate loading, shown in figure 5.2. An angled crack, which may have formed during the high strain rate step, grew during the subsequent low strain rate step from 10% to 12.5% strain. This is observable as a steep drop in the stress-strain curve during this load step at a macroscopic strain of approximately 11%.

Shear localization at shear bands begins before it is visible on the surface. An area of the gage section in which shear bands formed with increasing load is shown for specimen SRS-2 in figure 5.12. Table 5.2 provides measurements of the incremental strain in (A) the section that eventually developed a shear band and (B) the gage
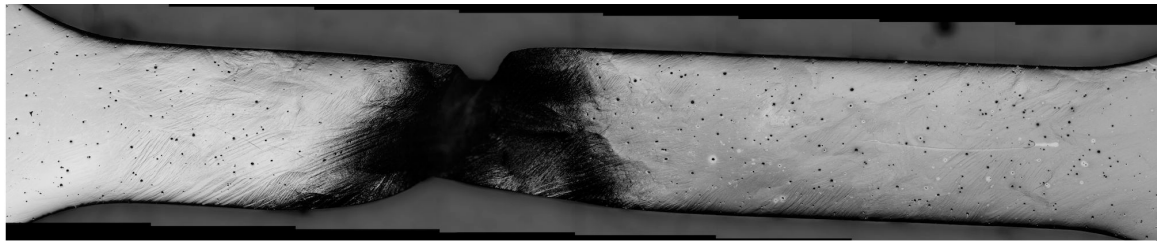
(a)
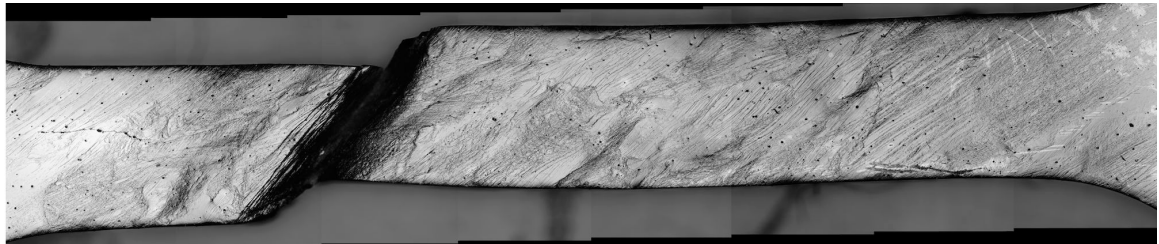
(b)
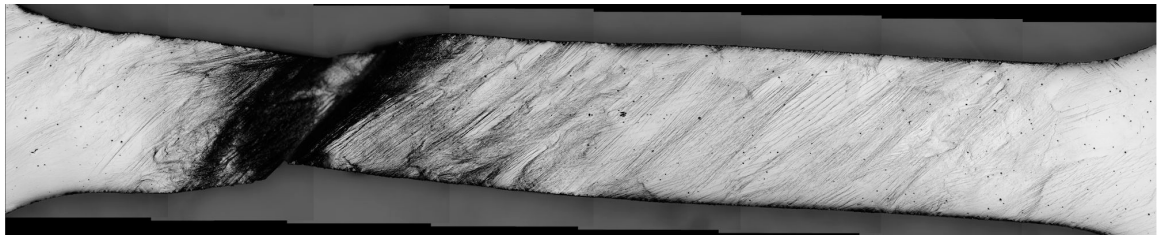
(c)
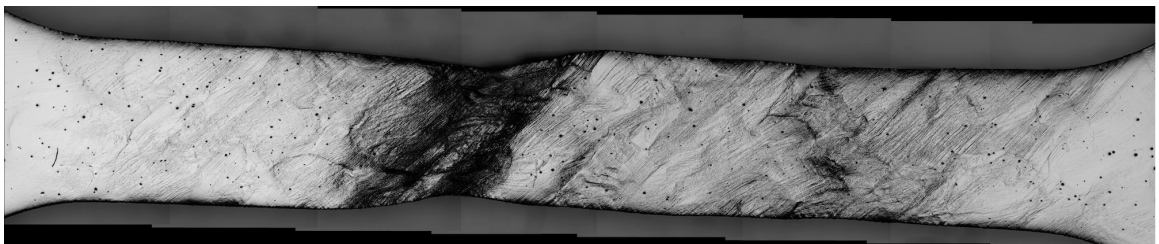
(d)

Figure 5.11: Post-test gage sections for room temperature specimen(a) UFG-5 and elevated temperature specimens (b) SRS-1, (c) SRS-2, and (d) SRS-3/4. The elevated temperature gage sections (b), (c), and (d) show similar shear band formation and plastic deformation across the entire gage section, while the room temperature gage section has a narrow necked region and minimal surface deformation visible away from the neck. Note, specimen UFG-5 is used for comparison because it was loaded identically to the elevated temperature specimens.
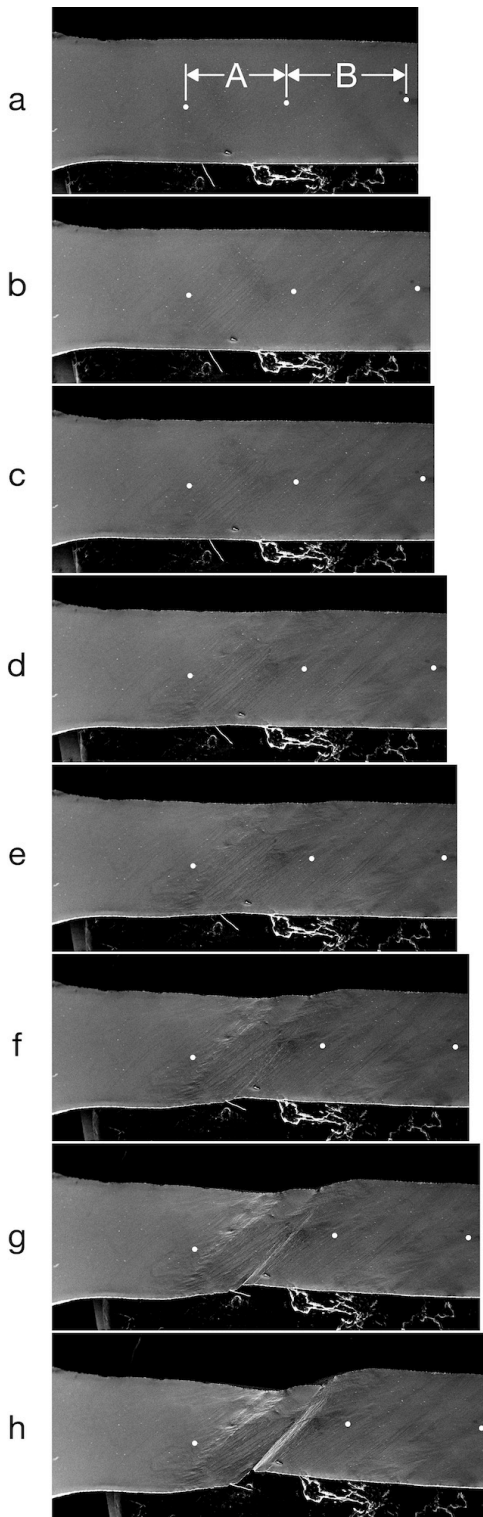
Figure 5.12: Surface deformation throughout loading of SRS-2. Load steps a – b, c – d, e – f, and g – h were at a strain rate of 3 x 10^{-3}. Load steps b – c, d – e, and f – g were at a strain rate of 2.5 x 10^{-5}. Data utilized in this test is from load steps a – b to d – e.

Load Step	Strain Rate s^{-1}	Incremental Strain (%)	
		A	B
a – b	3 x 10^{-3}	4.0	3.3
b – c	2.5 x 10^{-5}	2.0	2.4
c – d	3 x 10^{-3}	6.8	2.1
d – e	2.5 x 10^{-5}	4.0	2.3
e – f	3 x 10^{-3}	9.1	0.4
f – g	2.5 x 10^{-5}	8.1	0.6
g – h	3 x 10^{-3}	9.6	0.2

Table 5.2: Tabular data corresponding to the images in figure 5.12. Even before shear localization is visible on the surface in area A, strain is higher there in load step a – b. After the shear band is visible to the eye, strain almost exclusively localizes there.

section in which the DIC FOV was located. Note that the DIC data presented in this chapter consist of load steps a – b to d – e. After this, strain localization was not measurable at high strain rate and only small areas of localized strain were visible at low strain rate. Even from a – b in figure 5.12, the strain localization was greater in area A, suggesting that a shear band had already formed. The shear bands grew at a much faster rate at the high strain rate than at the low strain rate. Thus at high strain rate, plastic deformation occurred due to dislocation slip, as measured from the DIC data, and also from macroscopic shear banding.

Even after a shear band was visible on the surface, reducing the strain rate still resulted in increased strain localization at grain boundaries due to highly active diffusion based deformation mechanisms in the ECAP processed material. As table 5.2 shows, a large jump in the incremental strain in area A of the dogbone specimen occurred during load step c – d. This behavior was observed in all other elevated temperature strain rate sensitivity tests and corresponds to the drop in mean axial FOV strain as shown in figure 5.8. Even with this large strain localization outside of the DIC FOVs, in the following low strain rate load step for each test (shown in the last column of figure 5.8), the mean axial strain still increased, particularly at HAGBs as diffusion based deformation mechanisms dominated.

5.4 Conclusions

In this chapter, the strain rate sensitivity of UFG high purity aluminum was examined at 200 °C and strain rates alternating between 2.5 x 10^{-5} s^{-1} and 3 x 10^{-3} s^{-1}. The results presented here are the first full-field, quantitative investigations of the effect of strain rate on microstructural strain rate sensitivity. This work has yielded the following conclusions:

1. The strain rate sensitivity of UFG Al at 200 °C is over three times greater than the room temperature strain rate sensitivity.

2. The greatest strain rate sensitivity is observed at HAGBs due to diffusion deformation mechanisms that are more active at the elevated temperature during the low strain rate load steps. Intragranular strain localization displays the lowest strain rate sensitivity.

3. At high strain rate, strain localization at grain boundaries and within grains is generally of a similar magnitude.

4. High strain localization is visible in the gage section of these elevated temperature experiments as shear bands. At room temperature, necking plays a larger role.

5. Even after shear bands are visible in the gage section, strong strain localization still occurs at the grain boundaries at low strain rate.

CHAPTER VI

Summary and Future Directions

6.1 Summary

This thesis presents the development of the SEM-DIC experimental technique and its application to room temperature and elevated temperature tension experiments on ECAP processed UFG high purity aluminum. SEM-DIC was a new experimental technique when the research carried out in this thesis began in 2009. Thus, significant work went into developing the technique, with a large focus on the creation of small-scale surface patterning techniques. Improvements were also made to existing distortion correction techniques developed by Sutton et al. [169, 170, 171] to address stress relaxation. SEM-DIC was then applied to experimental investigations of ECAP processed Al, which for the first time enabled full-field strains and displacements to be linked to the underlying microstructure. Experiments were carried out at room temperature to study the strain localization behavior and active deformation mechanisms, and at elevated temperature to study the microstructural features responsible for the material's enhanced strain rate sensitivity.

One of the largest challenges in SEM-DIC, and the first addressed in this work, is the application of a suitable nanoscale surface tracking pattern. Our work greatly expanded the number of patterning techniques available for SEM-DIC experiments. The most successful patterning method, self-assembly of AuNPs, enables significantly

136

better spatial resolution than any previously published techniques. SEM-DIC spatial resolution is now limited by the resolution of the SEM and no longer by the size of the tracking pattern features. This technique enables the patterning of entire substrates with dense, even coverage of AuNPs which provide high contrast when imaged with a secondary electron or backscatter electron detector. Pattern feature size is easily controlled by AuNP diameter, and the technique can generate multi-scale patterns. This patterning method was utilized in the tests presented in chapters IV and V. Numerous other patterning techniques were also investigated including chemical vapor thin film rearrangement, FIB deposition of Pt markers, evaporation of gold through membrane filters, electron beam lithography, and drop-cast AuNPs. Electron beam lithography is suitable when precise control of the pattern location or features is required. On the other hand, drop cast AuNPs can be utilized for quick experiments when pattern location is not important.

Once a successful pattern has been applied, SEM image distortion is the next challenge that needs to be addressed. Sutton et al. [169, 170, 171] first addressed image distortion, but their original distortion correction methodology led to the capture of stress-relaxation displacements while the sample was under load. These displacements appear as large drift distortion and result in overcorrection of the DIC data. In this thesis, the accuracy of the original distortion correction technique was improved by accounting for stress relaxation. This was implemented through either the use of an unloaded calibration pattern or by relating the load drop during image capture to the stress-relaxation displacements. By utilizing the unloaded pattern, it was apparent that drift distortion remained nominally constant through tests, as opposed to steadily increasing as had been previously observed. SEM image noise was also investigated and image capture settings utilizing image integration, a high beam current, and long dwell times allowed for the greatest signal to noise ratio. For the best results, a field emission gun source SEM should be used in place of a tungsten filament SEM

to further reduce noise. A local averaging filter can be applied to noisy DIC data to make actual strain localization stand out over noise and allow for identification of initial strain localization.

SEM-DIC was applied to the study of microstructure length scale strain localization and active deformation mechanisms in ECAP processed UFG high purity Al. The first tests were carried out at room temperature at varying strain rates. Image resolutions as fine as 12 nm/pixel allowed us to quantitatively measure strain localization at the microstructural length scale and relate it to microstructural features. A room temperature strain rate sensitivity of 0.018, which is roughly 4x greater than the strain rate sensitivity of the coarse grained material, was measured from strain rate jump tests. However, this increase in strain rate sensitivity was not large enough to be measured in the SEM-DIC strain fields as the incremental strains were on the order of the DIC strain field noise. This work yielded the discovery that the shear strain imposed by the ECAP die has a large effect on the strain localization, causing dislocation slip to primarily occur on slip systems aligned with the theoretical shear plane in the final ECAP pass and high strain localization at HAGBs angled near 26.6°. This large amount of plastic flow occurring in similar directions likely leads to early necking and failure of the tension specimens. Additionally, the greatest strain localization typically occurred at HAGBs, especially in areas of characteristic UFG microstructure, where strain nearly exclusively localized at HAGBs. We also discovered that grain boundary sliding, while active in the material, only occurred at HAGBs separating banded microstructures. Shear strain localization occurred almost exclusively at these boundaries as a result of sliding.

Elevated temperature strain rate jump tests yielded first time results linking microstructural characteristics to strain rate sensitivity in ECAP processed UFG high purity Al. These experiments, carried out at 200 °C and with strain rates alternating between 2.5×10^{-5} s^{-1} and 3×10^{-3} s^{-1}, allowed us to measure the incremental full-field

strains and study the effect strain rate had on localization. The UFG Al displays a much greater strain rate sensitivity at 200 °C than at room temperature (0.057 +/- 0.008 versus 0.018 +/- 0.002). At elevated temperatures, the UFG Al work hardened during low strain rate load steps up to a macroscopic strain of 12.5%, unlike the room temperature material which did not work harden when the same loading parameters were used. As in the room temperature experiments, strain localization is strongly influenced by the ECAP shear direction in the final ECAP pass. The greatest strain rate sensitivity was observed at HAGBs, with much higher strain localization here during the low strain rate steps. During the high strain rate steps, strain localization at grain boundaries and grain interiors was of a similar magnitude. The elevated temperature tension specimens all developed shear bands which would have led to eventual failure. This is different from the room temperature tension specimens which all developed a localized neck. Even after these shear bands developed, strong strain localization occurred outside of the shear bands at low strain rates. As with the room temperature experiments, shear strain localized almost exclusively at the HAGBs separating microstructure bands in the banded microstructure.

6.2   Future Work

The research performed in this thesis has made apparent numerous areas where future research should be focused in both the SEM-DIC technique and the micro-scale mechanical properties of UFG metals. In developing SEM-DIC, significant effort should be exerted into error analysis and improving accuracy by reducing interpolation bias. Self-assembly of AuNPs has proven very successful at generating patterns for room temperature and low elevated temperature experiments and should be further developed to enable the assembly of nanoparticles with higher melting temperatures for high temperature experiments. With the recent ability to measure full-field displacements and strains with nanometer spatial resolution, there are significant

research opportunities in UFG metals. These include materials processed through different numbers of ECAP passes, or produced by ARB. Additionally, the unique behavior observed at HAGBs separating microstructure bands warrants additional TEM investigation.

6.2.1 Digital Image Correlation

Self-assembly of AuNPs yields excellent patterns for SEM-DIC experiments, yet cannot be utilized above gold's melting temperature of 1064 °C, which is much lower than that of numerous superalloys and ceramics suitable for turbine applications. E-beam lithography has been utilized by others to generate high temperature patterns [191], yet the benefits of self-assembly of nanoparticles over e-beam lithography makes it an attractive option. There is little existing literature on the self-assembly of high melting temperature nanoparticles. Challenges include synthesizing nanoparticles and finding an appropriate linking molecule since it is likely that silane will not work with the high temperature nanoparticles. One potential approach is the development of core-shell nanoparticles consisting of a shell of gold surrounding the high melting temperature core. Silane could then still be utilized to link the nanoparticles to the surface. The gold would melt at high temperatures but the core material would remain solid and van der Waals forces would hold it to the surface.

Error analysis in DIC experiments is challenging and a has recently attracted attention [6, 20]. Often error is presented as the standard deviation of the strain field in an unloaded image pair. However, this static error may not accurately reflect the error present in translated and strained images, making it difficult to provide error bounds to DIC measurements. More study is required into the source of DIC error so that it can be minimized. Additionally, interpolation bias present in low strain images can result in even greater error. Others have investigated removal of interpolation bias by fitting it with a sinusoidal function [32], but no true solution exists at the

present time. Research should be carried out to remove this bias either by relating it to the measured displacements or potentially through the use of different grayscale interpolation schemes.

6.2.2   UFG Strain Localization and Deformation Mechanisms

Pure Al processed through four ECAP passes was investigated in this work. Numerous investigations by others [42, 69, 123, 168, 179] have demonstrated that the mechanical properties of the material changes with additional passes. Research has shown that the occurrence of microstructure bands is reduced with additional processing, and ductility increases due to the development of a greater percentage of HAGBs. Thus as a continuation of this research, pure Al processed through eight and twelve passes following route B_C should be investigated in both room temperature constant strain rate and elevated temperature strain rate jump tension experiments. This would enhance our understanding of how the changes in microstructure affect strain localization and the active deformation mechanisms. These experiments could also be extended to ECAP material that has been processed utilizing other processing routes, although this is not a priority since prior work has shown that route B_C results in the greatest property improvements.

In this thesis, we propose that the reduced ductility likely resulted from the strong influence the ECAP shear plane had on the resulting microstructure and strain accommodation. Future work should investigate this narrow neck and shear band formation by performing SEM-DIC experiments on notched specimens to encourage shear band/necking in the FOV. This will improve our understanding of the failure of ECAP processed Al and also increase our overall understanding of the formation of shear bands. This work will be challenging since the high strains will interfere with correlation. However, small image steps and incremental correlation will likely allow for suitable correlation.

ECAP processing is only one way to produce UFG materials. Another technique that is promising for commercialization is ARB. In ARB, a sheet of material is rolled through rollers at elevated temperature to a thickness reduction of typically 50%. The sheet is then cut in half, wire brushed, heated and rolled again. This is repeated until the desired strain or laminate thickness is achieved. Like ECAP processing, this yields an ultrafine-grained microstructure and enhanced mechanical properties. ARB can produce single phase or dual-phase nanolaminates and can create metal-matrix nanocomposites by applying reinforcing material such as ceramic powder between layers [7]. Experiments should be carried out on ARB processed materials to study how the ordered interface between layers reacts to shock loading and straining [14]. The edge of the material should be observed to study how strain localization and active deformation mechanisms are affected by the interfaces.

In this thesis, grain boundary sliding was found at microstructure band boundaries, yet it is unclear if this is a result of enhanced room temperature diffusion or motion of extrinsic grain boundary dislocations. TEM investigations of these grain boundaries could act to answer this question. Thermo-mechanical loading though heating or the use of nano-manipulators could be utilized to observe dislocation motion within these grain boundaries. This work would have the potential to validate computational models and would improve our understanding of low temperature grain boundary sliding.

Finally, more research effort should focus on commercialization of UFG metals to take advantage of their impressive strength to weight ratios. In terms of ECAP processing, research should be focused on the incorporation of ECAP into conventional extrusion dies. Extruded aluminum is utilized in aerospace, automotive, sporting goods, and wind power generation applications where weight is the enemy. ECAP has been applied to solid rods and sheets, but expanding the process to hollow tubes and complex extruded shapes could revolutionize the extruded aluminum market.

APPENDICES

APPENDIX A

Gold Nanoparticle Synthesis Recipes

AuNPs were synthesized following the procedure outlined by Frens [54]. One gram of Gold (III) chloride trihydrate (HAuCl$_4$·3H$_2$O) (Sigma Aldrich item number 520918-1G) was dissolved in 250 mL of DI water to make a 10 mM stock solution of gold(III) ions. 0.5 grams of trisodium citrate dihydrate (C$_6$H$_5$Na$_3$O$_7$·2H$_2$O) (Sigma Aldrich item number S1804-500G) was dissolved in 50 mL of DI water to make a 38.8 mM stock solution of trisodium citrate. To make gold nanoparticles, 10 mL of the 10 mM stock solution of gold(III) ions was diluted to 100 mL with DI water to make a 1mM solution. The diluted solution was brought to boil in an Erlenmeyer flask on a 500 °C hotplate while stirred with a magnetic stirring rod at 300 RPM. When boiling, a volume of the 38.8 mM trisodium citrate solution was added to achieve the desired nanoparticle size as outlined in table A.1. The temperature of the hotplate was then reduced to 350°C, or a temperature sufficient to keep the solution above the boiling point, while the solution was stirred until the reaction had finished and color change ceased as specified in table A.1.

The AuNP concentration can be increased/decreased by increasing/decreasing the molarity of the gold(III) ion solution. However, as the concentration increases, the stability of the AuNPs decreases. For example, in an attempt to make highly

144

concentrated 13 nm diameter AuNPs, 34 mL of a 3 mM gold(III) ion solution and 10 mL of 38.8 mM trisodium citrate solution was used. The AuNP solution turned red as expected, indicating AuNP formation, but quickly turned black as the AuNPs agglomerated. The recipes in table A.1 produce stable AuNPs which have been proven capable of generating excellent surface patterns for SEM-DIC.

Approx. AuNP diameter (nm)	Volume of 38.8 mM (mL) trisodium citrate	Time to complete reaction (min)	Final color
13	10	3	red
30	5	5	red
45	4	5	red
60	3	10	dark red/purple
70	2.3	10	dark red/purple
100	1.7	30	orange
150	1.3	30	orange

Table A.1: Recipes for the production of gold nanoparticles. Each recipe starts by adding 100 mL of 1 mM solution of gold(III) ions to a flask. When boiling, the specified volume of 38.8 mM trisodium citrate is added. The solution is boiled for the specified time until the reaction is completed, indicated by a constant solution color.

APPENDIX B

DIC Strain Calculation

Two-dimensional DIC carried out in this work is only capable of measuring in-plane displacements, thus Lagrangian strain was calculated from the DIC displacement fields under the assumption of a plane strain condition. This is a simplification but does not require assumptions to be made for the out-of-plane displacements and strains which cannot be measured with two-dimensional DIC. Plane strain is typically assumed when calculating strain fields from two-dimensional DIC data [82, 110, 130, 171, 190]. However, there are works where plane stress is assumed and out-of-plane strain is approximated under the assumption of plastic incompressibility [1, 193] or transverse isotropy [129]. This appendix provides the reader with an explanation for our choice of plane strain and details of the procedure utilized to calculate strains from the in-plane DIC measured displacements.

When measuring microscopic strain localization, suitable assumptions for out-of-plane strain are not clear. For macroscopic strain measurements, a plane stress assumption may yield more accurate results for the tension specimen dimensions utilized in this work. However, macro-scale assumptions are not always appropriate for micro-scale measurements. First, in SEM-DIC the working distance is adjusted throughout the test to keep the FOV in focus. Thus the out-of-plane contraction

of the specimen that makes a macro-scale plane strain assumption inaccurate is accounted for and has a negligible effect on the microscopic strain field. Second, the best assumption for out-of-plane strain can change based on where strain is being measured in the microstructure. For example, in the case of dislocation slip, plane strain would be the best assumption for slip occurring in the $x - y$ plane. Out-of-plane slip, will cause out-of-plane normal and shear strains, thus plane stress would be a better assumption in these cases. To achieve accurate out-of-plane measures, three-dimensional SEM-DIC would be required. While this is possible [205], it is often not practical. Even the application of crystal plasticity models utilizing the FOVs EBSD data are not capable of accurately accessing out-of-plane displacements and strains due to the effects of the underlying microstructure. The application of *in-situ* three-dimensional DIC and the development of improved crystal plasticity models are left for future work.

The first step in calculating strain from the DIC displacement fields is to calculate the deformed coordinates of the DIC data points. These coordinates are defined as

$$\mathbf{x} = \mathbf{X} + \mathbf{d}, \tag{B.1}$$

where $\mathbf{x}$ is the position of the data point in the deformed coordinates, $\mathbf{X}$ is the position of the data point in reference coordinates, and $\mathbf{d}$ is the DIC calculated displacement of the point.

Raw DIC data can suffer from significant noise, requiring the deformed coordinate fields $\mathbf{x}$ to be smoothed prior to strain calculation. Smoothing is carried out in small subsets of the deformed coordinate fields, referred to as "strain calculation windows", to ensure heterogeneous strain localization is captured. Too small of a strain calculation window will not sufficiently suppress noise, while too large of a

window will not be capable of capturing local heterogeneous strain localization. The amount of smoothing is also affected by the order of the smoothing surface utilized. Bi-linear, bi-quadratic, and bi-cubic surfaces are commonly used. Strain localization in UFG Al, calculated from strain calculation windows of 5 x 5, 15 x 15, and 25 x 25 data points using bi-linear, bi-quadratic, and bi-cubic smoothing surfaces are shown in figure B.1. Strain field noise is reduced as the window size increases, and also to a lesser extent as the order of the polynomial smoothing surfaces decreases. Little difference can be seen between the bi-linear strain fields and the bi-quadratic strain fields, however bi-quadratic is still recommended as it will provide more accurate measures of strain at areas of sharp displacement offsets. This type of behavior could exist in composites composed of materials with different stiffnesses. In this thesis, 15 x 15 datapoint strain calculation windows smoothed with bi-quadratic surfaces were utilized (figure B.1(e)). These parameters yielded sufficient noise reduction while limiting excessive smoothing apparent in the larger 25 x 25 data point subsets (figure B.1(g) - (i)). There exist no rules for selection of the strain calculation window size or type of smoothing surface, so the user must decide on the combination which provides the best balance of noise suppression and accuracy.

The gradients of the smoothed surfaces are calculated within each strain calculation window to populate the deformation gradient tensor, $\mathbf{F}$. In tensor notation,

$$F_{ij} = \begin{bmatrix} \frac{\delta x_i}{\delta X_i} & \frac{\delta x_i}{\delta X_j} \\ \frac{\delta x_j}{\delta X_i} & \frac{\delta x_j}{\delta X_j} \end{bmatrix}. \tag{B.2}$$

The Lagrangian finite strain tensor $\mathbf{E}$ at the center point of each strain calculation window is then calculated according to the equation
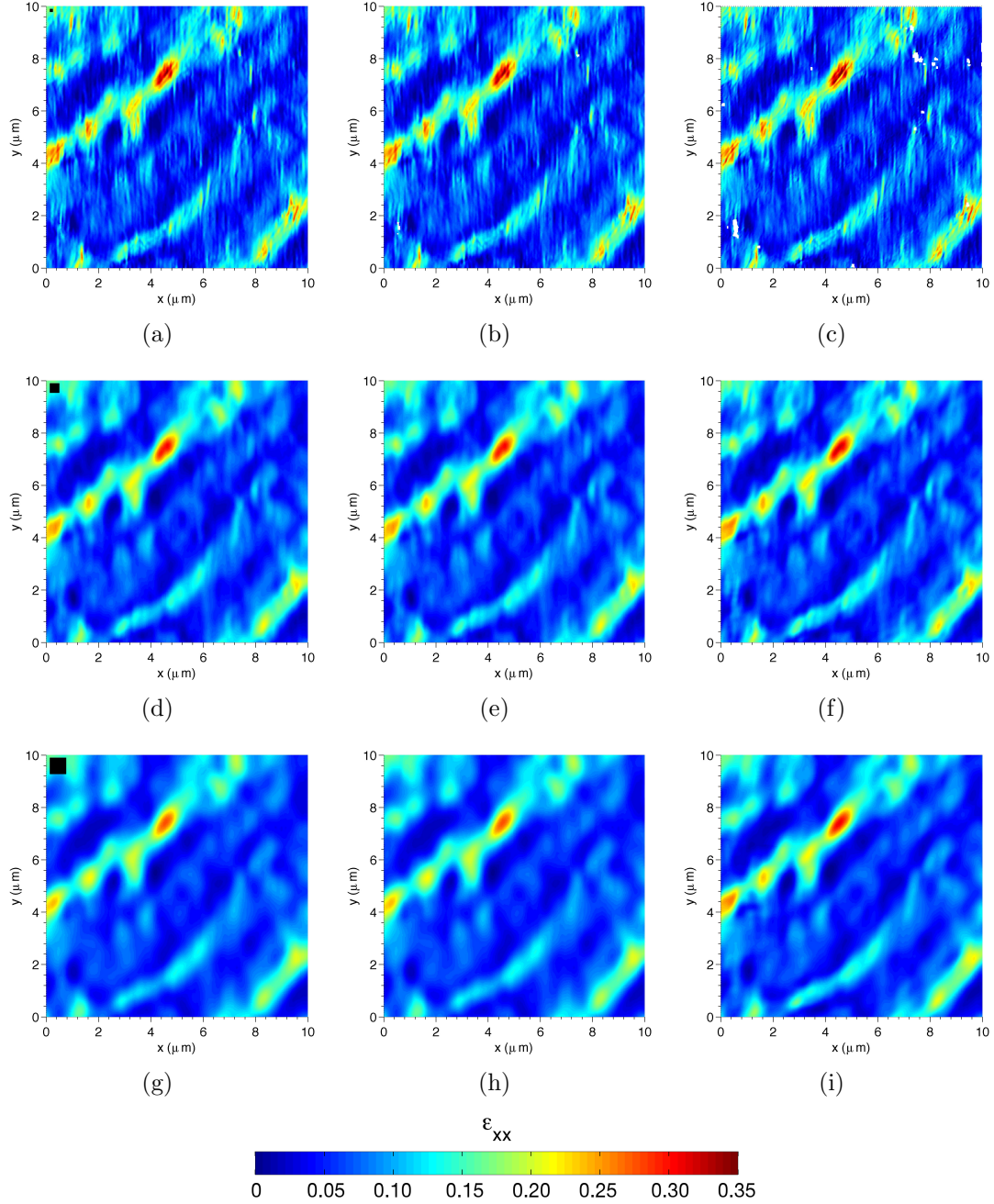
Figure B.1: Comparison of strain fields calculated with (a) a 5 x 5 data point subset and bi-linear surface fit, (b) a 5 x 5 data point subset and bi-quadratic surface fit, (c) a 5 x 5 data point subset and bi-cubic surface fit, (d) a 15 x 15 data point subset and bi-linear surface fit, (e) a 15 x 15 data point subset and bi-quadratic surface fit, (f) a 15 x 15 data point subset and bi-cubic surface fit, (g) a 25 x 25 data point subset and bi-linear surface fit, (h) a 25 x 25 data point subset and bi-quadratic surface fit, and (i) a 25 x 25 data point subset and bi-cubic surface fit. Lower order surface fits and large strain calculation windows result in greater smoothing. The black box in the corner of (a), (d), and (g) represent the size of the strain calculation window.

$$\mathbf{E} = \frac{1}{2}\left(\mathbf{F}^T\mathbf{F} - \mathbf{I}\right) \tag{B.3}$$

where $\mathbf{I}$ is the identity matrix. In tensor notation,

$$E_{ij} = \frac{1}{2}\left(F_{ki}F_{kj} - \delta_{ij}\right). \tag{B.4}$$

Using $F_{ij} = \delta_{ij} + \frac{\delta d_i}{\delta X_j}$, where δ_{ij} is the Kronecker delta and is 1 when $i = j$ and 0 when $i \neq j$,

$$\begin{aligned}
E_{ij} &= \frac{1}{2}\left[\left(\delta_{ki} + \frac{\delta d_k}{\delta X_i}\right)\left(\delta_{kj} + \frac{\delta d_k}{\delta X_j}\right) - \delta_{ij}\right] \\
&= \frac{1}{2}\left[\delta_{ki}\delta_{kj} + \delta_{ki}\frac{\delta d_k}{\delta X_j} + \delta_{kj}\frac{\delta d_k}{\delta X_i} + \frac{\delta d_k}{\delta X_i}\frac{\delta d_k}{\delta X_j} - \delta_{ij}\right] \\
&= \frac{1}{2}\left[\delta_{ij} + \frac{\delta d_i}{\delta X_j} + \frac{\delta d_j}{\delta X_i} + \frac{\delta d_k}{\delta X_i}\frac{\delta d_k}{\delta X_j} - \delta_{ij}\right] \\
&= \frac{1}{2}\left[\frac{\delta d_i}{\delta X_j} + \frac{\delta d_j}{\delta X_i} + \frac{\delta d_k}{\delta X_i}\frac{\delta d_k}{\delta X_j}\right]. \tag{B.5}
\end{aligned}$$

To match the naming convention utilized in DIC, d_1 is replaced with u, d_2 is replaced with v, X_1 is replaced with x, and X_2 is replaced with y. This yields the equations used to calculate the strain components utilized in this work,

$$\epsilon_{xx} = E_{11} = \frac{\delta u}{\delta x} + \frac{1}{2}\left[\left(\frac{\delta u}{\delta x}\right)^2 + \left(\frac{\delta v}{\delta x}\right)^2\right] \tag{B.6}$$

$$\epsilon_{yy} = E_{22} = \frac{\delta v}{\delta y} + \frac{1}{2}\left[\left(\frac{\delta u}{\delta y}\right)^2 + \left(\frac{\delta v}{\delta y}\right)^2\right] \tag{B.7}$$

$$\epsilon_{xy} = E_{12} = \frac{1}{2}\left(\frac{\delta u}{\delta y} + \frac{\delta v}{\delta x}\right) + \frac{1}{2}\left[\left(\frac{\delta u}{\delta x}\frac{\delta u}{\delta y}\right) + \left(\frac{\delta v}{\delta x}\frac{\delta v}{\delta y}\right)\right]. \tag{B.8}$$

Note that the calculated strains are only assigned to the center data point of each strain calculation window. This is done because the smoothing surface may not accurately reflect curvature of the deformed coordinate fields outside of the strain calculation window. Thus accuracy of the fit decreases as the edges of the strain calculation window are approached. Strain is calculated at every data point by shifting the strain calculation window by one data point and repeating the outlined procedure.

In this thesis, ϵ_{xx} is referred to as axial strain, ϵ_{yy} is referred to as transverse strain, and ϵ_{xy} is referred to as shear strain. While ϵ_{xy} is referred to as shear strain, the reader should note that according to equation B.8, it consists of both shear and normal deformations. In future work, in combination with 3D SEM-DIC, the polar decomposition of the deformation gradient could be utilized to determine the true stretch and rotation deformations.

REFERENCES

REFERENCES

[1] W. Abuzaid, H. Sehitoglu, and J. Lambros. Plastic strain localization and fatigue micro-crack formation in Hastelloy X. *Materials Science and Engineering: A*, 561(0):507 – 519, 2013.

[2] S.R. Agnew, U.F. Kocks, K.T. Hartwig, and J.R. Weertman. Texture evolution during equal channel angular forging and dislocation boundary misorientations after severe plastic deformation. In J.V. Carstensen, T. Leffers, T. Lorentzen, O.B. Pedersen, B.F. Søresen, and G. Winther, editors, *Proceedings of the 19th Risø International Symposium on Materials Science: Modeling of Structure and Mechanics from Microscale to Product*, pages 201–206. Risø National Laboratory, 1998.

[3] N. Ahmed and A. Hartmaier. Mechanisms of grain boundary softening and strain-rate sensitivity in deformation of ultrafine-grained metals at high temperatures. *Acta Materialia*, 59(11):4323 – 4334, 2011.

[4] B. Ahn, E.J. Lavernia, and S.R. Nutt. Dynamic observations of deformation in an ultrafine-grained Al-Mg alloy with bimodal grain structure. *Journal of Materials Science*, 43(23-24):7403–7408, 2008.

[5] B. Ahn and S.R. Nutt. Strain mapping of Al-Mg alloy with multi-scale grain structure using digital image correlation method. *Experimental Mechanics*, 50(1):117–123, 2010.

[6] F. Amiot, M. Bornert, P. Doumalin, J. C. Dupré, M. Fazzini, J. J. Orteu, C. Poilâne, L. Robert, R. Rotinat, E. Toussaint, B. Wattrisse, and J. S. Wienin. Assessment of digital image correlation measurement accuracy in the ultimate error regime: Main results of a collaborative benchmark. *Strain*, 49(6):483–496, 2013.

[7] S. Amirkhanlou, M. Ketabchi, N. Parvin, S. Khorsand, and R. Bahrami. Accumulative press bonding; a novel manufacturing process of nanostructured metal matrix composites. *Materials & Design*, 51(0):367 – 374, 2013.

[8] Y. Amouyal, S.V. Divinski, Y. Estrin, and E. Rabkin. Short-circuit diffusion in an ultrafine-grained copper-zirconium alloy produced by equal channel angular pressing. *Acta Materialia*, 55(17):5968 – 5979, 2007.

[9] A. Ando, H. Sunaoshi, S. Sato, S. Magoshi, K. Hattori, M. Suenaga, H. Wada, H. Housai, S. Hashimoto, and K. Sugihara. Contamination charging up effect in a variably shaped electron beam writer. *Japanese Journal of Applied Physics*, 35(Part 1, No. 12B):6426–6428, 1996.

[10] K.J. Aström and R.M. Murray. *Feedback Systems: An Introduction for Scientists and Engineers.* Princeton University Press, 2010.

[11] A. Azushima, R. Kopp, A. Korhonen, D.Y. Yang, F. Micari, G.D. Lahoti, P. Groche, J. Yanagimoto, N. Tsuji, A. Rosochowski, and A. Yanagida. Severe plastic deformation (SPD) processes for metals. *CIRP Annals - Manufacturing Technology*, 57(2):716 – 735, 2008.

[12] T.A. Berfield, J.K. Patel, R.G. Shimmin, P.V. Braun, J. Lambros, and N.R. Sottos. Fluorescent image correlation for nanoscale deformation measurements. *Small*, 2(5):631–635, 2006.

[13] T.A. Berfield, J.K. Patel, R.G. Shimmin, P.V. Braun, J. Lambros, and N.R. Sottos. Micro- and nanoscale deformation measurement of surface and internal planes via digital image correlation. *Experimental Mechanics*, 47:51–62, 2007.

[14] I.J. Beyerlein, N.A. Mara, J. Wang, J.S. Carpenter, S.J. Zheng, W.Z. Han, R.F. Zhang, K. Kang, T. Nizolek, and T.M. Pollock. Structure property functionality of bimetal interfaces. *JOM*, 64(10):1192–1207, 2012.

[15] T.R. Bieler, P. Eisenlohr, F. Roters, D. Kumar, D.E. Mason, M.A. Crimp, and D. Raabe. The role of heterogeneous deformation on damage nucleation at grain boundaries in single phase metals. *International Journal of Plasticity*, 25(9):1655 – 1683, 2009.

[16] N. Biery, M. Graef, and T.M. Pollock. A method for measuring microstructural-scale strains using a scanning electron microscope: Applications to γ-titanium aluminides. *Metallurgical and Materials Transactions A*, 34(10):2301–2313, 2003.

[17] N.E. Biery, M. DeGraef, and T.M. Pollock. Influence of microstructure and strain distribution on failure properties in intermetallic TiAl-based alloys. *Materials Science and Engineering: A*, 319321(0):613 – 617, 2001.

[18] W. Blum and X.H. Zeng. A simple dislocation model of deformation resistance of ultrafine-grained materials explaining Hall-Petch strengthening and enhanced strain rate sensitivity. *Acta Materialia*, 57(6):1966 – 1974, 2009.

[19] A. Böhner, V. Maier, K. Durst, H.W. Höppel, and M. Göken. Macro- and nanomechanical properties and strain rate sensitivity of accumulative roll bonded and equal channel angular pressed ultrafine-grained materials. *Advanced Engineering Materials*, 13(4):251–255, 2011.

[20] M. Bornert, F. Brémand, P. Doumalin, J.-C. Dupré, M. Fazzini, M. Grédiac, F. Hild, S. Mistou, J. Molimard, J.-J. Orteu, L. Robert, Y. Surrel, P. Vacher, and B. Wattrisse. Assessment of digital image correlation measurement errors: Methodology and results. *Experimental Mechanics*, 49(3):353–370, 2009.

[21] P.W. Bridgeman. *Studies In Large Plastic Flow And Fracture: With Special Emphasis On the Effects of Hydrostatic Pressure*. McGraw, New York, 1952.

[22] P.W. Bridgman. On torsion combined with compression. *Journal of Applied Physics*, 14(6):273–283, 1943.

[23] H.A. Bruck, S.R. McNeill, M.A. Sutton, and W.H. Peters III. Digital image correlation using Newton-Raphson method of partial differential correction. *Experimental Mechanics*, 29:261–267, 1989.

[24] J. Carroll, W. Abuzaid, J. Lambros, and H. Sehitoglu. An experimental methodology to relate local strain to microstructural texture. *Review of Scientific Instruments*, 81(8):083703, 2010.

[25] G.M. Castelluccio, A.A. Yawny, J.E. Perez Ipiña, and H.A. Ernst. In situ evaluation of tensile properties of heat-affected zones from welded steel pipes. *Strain*, 48(1):68–74, 2012.

[26] P.K. Chaudhury, B. Cherukuri, and R. Srinivasan. Scaling up of equal-channel angular pressing and its effect on mechanical properties, microstructure, and hot workability of AA 6061. *Materials Science and Engineering: A*, 410411(0):316 – 318, 2005.

[27] S.Y Chen, Kuen-Yu T., P.C.W. Ng, H.T Ng, C.H. Liu, Y.T. Shen, C.H. Kuan, Y.Y. Chen, Y.H. Kuo, C.J. Wu, and J.Y. Yen. In situ beam drift detection using a two-dimensional electron-beam position monitoring system for multiple-electron-beam direct-write lithography. *Journal of Vacuum Science Technology B: Microelectronics and Nanometer Structures*, 29(4):041607–041607–12, Jul 2011.

[28] N.Q. Chinh, T. Csanádi, J. Gubicza, and T.G. Langdon. Plastic behavior of face-centered-cubic metals over a wide range of strain. *Acta Materialia*, 58(15):5015 – 5021, 2010.

[29] N.Q. Chinh, T. Györi, R.Z. Valiev, P. Szommer, G. Varga, K. Havancsák, and T.G. Langdon. Observations of unique plastic behavior in micro-pillars of an ultrafine-grained alloy. *MRS Communications*, 2:75–78, 9 2012.

[30] N.Q. Chinh, P. Szommer, T. Csanádi, and T.G. Langdon. Flow processes at low temperatures in ultrafine-grained aluminum. *Materials Science and Engineering: A*, 434(12):326 – 334, 2006.

[31] N.Q. Chinh, P. Szommer, Z. Horita, and T.G. Langdon. Experimental evidence for grain-boundary sliding in ultrafine-grained aluminum processed by severe plastic deformation. *Advanced Materials*, 18(1):34–39, 2006.

[32] S. Choi and S.P. Shah. Measurement of deformations on concrete subjected to compression using image correlation. *Experimental Mechanics*, 37(3):307–313, 1997.

[33] S.A. Collette, M.A. Sutton, P. Miney, A.P. Reynolds, X. Li, P.E. Colavita, W.A. Scrivens, Y. Luo, T. Sudarshan, P. Muzykov, and M.L. Myrick. Development of patterns for nanoscale strain measurements: I. Fabrication of imprinted Au webs for polymeric materials. *Nanotechnology*, 15(12):1812, 2004.

[34] J. Dautriat, M. Bornert, N. Gland, A. Dimanov, and J. Raphanel. Localized deformation induced by heterogeneities in porous carbonate analysed by multi-scale digital image correlation. *Tectonophysics*, 503(12):100 – 116, 2011.

[35] D.L. Davidson. The effect of a cluster of similarly oriented grains (a supergrain) on fatigue crack initiation characteristics of clean materials. In J.E. Allison, J.W. Jones, J.M. Larsen, and R.O. Ritchie, editors, *Fourth International Conference on Very High Cycle Fatigue (VHCF-4)*, pages 23–28. Warrendale, PA: TMS, 2007.

[36] J.R. Davis and Associates. *Aluminum and Aluminum Alloys*. ASM International, 1993.

[37] R.D. Deegan, O. Bakajin, T.F. Dupont, G. Huber, S.R. Nagel, and T.A. Witten. Capillary flow as the cause of ring stains from dried liquid drops. *Nature*, 389:827 – 829, 1997.

[38] A. Delebecque, C. Thomas, C. Methivier, E. Coffre, H. Paoli, and M. Carre. Reactivity of a hydroxylated alumina surface in the presence of NO diluted in N2: A PM-IRRAS in situ investigation. *The Journal of Physical Chemistry C*, 112(8):2964–2971, 2008.

[39] A. Delebecque, C. Thomas, C.M. Pradier, C. Methivier, H. Paoli, E. Coffre, and M. Carré. On the reactivity of NO/N2 mixtures with aluminum surfaces: A combined PM-IRRAS and QCM investigation. *Surface Science*, 602(1):283 – 290, 2008.

[40] E. Dickinson and L. Eriksson. Particle flocculation by adsorbing polymers. *Advances in Colloid and Interface Science*, 34(0):1 – 29, 1991.

[41] S.V. Divinski, J. Ribbe, G. Reglitz, Y. Estrin, and G. Wilde. Percolating network of ultrafast transport channels in severely deformed nanocrystalline metals. *Journal of Applied Physics*, 106(6):–, 2009.

[42] J. Dvorak, V. Sklenicka, and Z. Horita. Microstructural evolution and mechanical properties of high purity aluminium processed by equal-channel angular pressing. *Materials Transactions*, 49(1):15–19, 2008.

[43] C. Efstathiou, H. Sehitoglu, and J. Lambros. Multiscale strain measurements of plastically deforming polycrystalline titanium: Role of deformation heterogeneities. *International Journal of Plasticity*, 26(1):93 – 106, 2010.

[44] U. Erb, A.M. El-Sherik, G. Palumbo, and K.T. Aust. Synthesis, structure and properties of electroplated nanocrystalline materials. *Nanostructured Materials*, 2(4):383 – 390, 1993.

[45] Y. Estrin, C. Kasper, S. Diederichs, and R. Lapovok. Accelerated growth of pre-osteoblastic cells on ultrafine grained titanium. *Journal of Biomedical Materials Research Part A*, 90A(4):1239–1242, 2009.

[46] Y. Estrin and A. Vinogradov. Extreme grain refinement by severe plastic deformation: A wealth of challenging science. *Acta Materialia*, 61(3):782 – 817, 2013.

[47] M. Fan and A.G. Brolo. Silver nanoparticles self assembly as SERS substrates with near single molecule detection limit. *Phys. Chem. Chem. Phys.*, 11:7381–7389, 2009.

[48] S. Ferrasse, K.T. Hartwig, R.E. Goforth, and V.M. Segal. Microstructure and properties of copper and aluminum alloy 3003 heavily worked by equal channel angular extrusion. *Metallurgical and Materials Transactions A*, 28(4):1047–1057, 1997.

[49] R.B. Figueiredo, P.R. Cetlin, and T.G. Langdon. The processing of difficult-to-work alloys by ecap with an emphasis on magnesium alloys. *Acta Materialia*, 55(14):4769 – 4779, 2007.

[50] A. Franquet, M. Biesemans, H. Terryn, R. Willem, and J. Vereecken. Study of the interaction of hydrolysed silane solutions with pre-treated aluminium substrates. *Surface and Interface Analysis*, 38(4):172–175, 2006.

[51] A. Franquet, H. Terryn, and J. Vereecken. Composition and thickness of non-functional organosilane films coated on aluminium studied by means of infra-red spectroscopic ellipsometry. *Thin Solid Films*, 441(12):76 – 84, 2003.

[52] S. Franssila. *Introduction to Microfabrication*. Chichester, UK: Wiley, 2010.

[53] R.G. Freeman, K.C. Grabar, K.J. Allison, R.M. Bright, J.A. Davis, A.P. Guthrie, M.B. Hommer, M.A. Jackson, P.C. Smith, D.G. Walter, and M.J. Natan. Self-assembled metal colloid monolayers: An approach to SERS substrates. *Science (New York, NY)*, 267(5204):1629, 1995.

[54] G. Frens. Controlled nucleation for the regulation of the particle size in monodisperse gold suspensions. *Nat Phys Sci*, 241:20–22, 1973.

[55] Y. Fukuda, K. Oh-ishi, M. Furukawa, Z. Horita, and T.G. Langdon. The application of equal-channel angular pressing to an aluminum single crystal. *Acta Materialia*, 52(6):1387 – 1395, 2004.

[56] Y. Fukuda, K. Oh-ishi, Z. Horita, and T.G. Langdon. Processing of a low-carbon steel by equal-channel angular pressing. *Acta Materialia*, 50(6):1359 – 1368, 2002.

[57] M. Furukawa, Z. Horita, M. Nemoto, R.Z. Valiev, and T.G. Langdon. Microhardness measurements and the Hall-Petch relationship in an Al-Mg alloy with submicrometer grain size. *Acta Materialia*, 44(11):4619 – 4629, 1996.

[58] M. Furukawa, Y. Iwahashi, Z. Horita, M. Nemoto, and T.G. Langdon. The shearing characteristics associated with equal-channel angular pressing. *Materials Science and Engineering: A*, 257(2):328 – 332, 1998.

[59] Londe G., Han A., and Cho H.J. *Functional Nanostructures: Processing, Characterization, and Applications.* New York: Springer, seal s. edition, 2007.

[60] A. Gilat, T.E. Schmidt, and A.L. Walker. Full field strain measurement in compression and tensile split Hopkinson bar experiments. *Experimental Mechanics*, 49:291–302, 2009.

[61] H. Gleiter. Nanocrystalline materials. *Progress in Materials Science*, 33(4):223 – 315, 1989.

[62] J.G. Goodberlet, J.T. Hastings, and H.I. Smith. Performance of the Raith 150 electron-beam lithography system. *Journal of Vacuum Science Technology B: Microelectronics and Nanometer Structures*, 19(6):2499–2503, Nov 2001.

[63] K.C. Grabar, K.J. Allison, B.E. Baker, R.M. Bright, K.R. Brown, R.G. Freeman, A.P. Fox, C.D. Keating, M.D. Musick, and M.J. Natan. Two-dimensional arrays of colloidal gold particles: A flexible approach to macroscopic metal surfaces. *Langmuir*, 12(10):2353–2361, 1996.

[64] K.C. Grabar, R.G. Freeman, M.B. Hommer, and M.J. Natan. Preparation and characterization of Au colloid monolayers. *Analytical Chemistry*, 67(4):735–743, 1995.

[65] R.F. Hamilton, S. Dilibal, H. Sehitoglu, and H.J. Maier. Underlying mechanism of dual hysteresis in NiMnGa single crystals. *Materials Science and Engineering: A*, 528(3):1877 – 1881, 2011.

[66] J.H. Han, H.K. Seok, Y.H. Chung, M.C. Shin, and J.C. Lee. Texture evolution of the strip cast 1050 Al alloy processed by continuous confined strip shearing and its formability evaluation. *Materials Science and Engineering: A*, 323(12):342 – 347, 2002.

[67] J.D. Helm, S.R. McNeill, and M.A. Sutton. Improved three-dimensional image correlation for surface displacement measurement. *Optical Engineering*, 35(7):1911–1920, 1996.

[68] D.W. Hess and K.A. Reinhard. 6 - plasma stripping, cleaning, and surface conditioning. In K.A. Reinhardt and W. Kern, editors, *Handbook of Silicon Wafer Cleaning Technology (Second Edition)*, pages 355 – 427. William Andrew Publishing, Norwich, NY, second edition edition, 2008.

[69] H.W. Höppel, J. May, P. Eisenlohr, and M. Göken. Strain-rate sensitivity of ultrafine-grained materials. *Zeitschrift für Metallkunde*, 96(6):566–571, 2005.

[70] Z. Horita, T. Fujinami, and T.G. Langdon. The potential for scaling ECAP: effect of sample size on grain refinement and mechanical properties. *Materials Science and Engineering: A*, 318(12):34 – 41, 2001.

[71] Z. Horita, T. Fujinami, M. Nemoto, and T.G. Langdon. Equal-channel angular pressing of commercial aluminum alloys: Grain refinement, thermal stability and tensile properties. *Metallurgical and Materials Transactions A*, 31(3):691–701, 2000.

[72] Z. Horita, M. Furukawa, M. Nemoto, and T.G. Langdon. Development of fine grained structures using severe plastic deformation. *Materials Science and Technology*, 16(11):1239, Nov 2000.

[73] R.J. Hunter. *Foundations of Colloid Science, Vol 1*. Oxford University Press, New York, 1987.

[74] K.V. Ivanov and E.V. Naydenkin. Structure evolution and deformation mechanisms in ultrafine-grained aluminum under tension at room temperature. In *Materials Science Forum*, volume 667, pages 915–920. Trans Tech Publ, 2010.

[75] Y. Iwahashi, M. Furukawa, Z. Horita, M. Nemoto, and T.G. Langdon. Microstructural characteristics of ultrafine-grained aluminum produced using equal-channel angular pressing. *Metallurgical and Materials Transactions A*, 29(9):2245–2252, 1998.

[76] Y. Iwahashi, Z. Horita, M. Nemoto, and T.G. Langdon. An investigation of microstructural evolution during equal-channel angular pressing. *Acta Materialia*, 45(11):4733 – 4741, 1997.

[77] Y. Iwahashi, Z. Horita, M. Nemoto, and T.G. Langdon. Factors influencing the equilibrium grain size in equal-channel angular pressing: Role of Mg additions to aluminum. *Metallurgical and Materials Transactions A*, 29(10):2503–2510, 1998.

[78] Y. Iwahashi, Z. Horita, M. Nemoto, and T.G. Langdon. The process of grain refinement in equal-channel angular pressing. *Acta Materialia*, 46(9):3317 – 3331, 1998.

[79] Y. Iwahashi, J. Wang, Z. Horita, M. Nemoto, and T.G. Langdon. Principle of equal-channel angular pressing for the processing of ultra-fine grained materials. *Scripta Materialia*, 35(2):143 – 146, 1996.

[80] H. Jin, W.Y. Lu, and J. Korellis. Micro-scale deformation measurement using the digital image correlation technique and scanning electron microscope imaging. *The Journal of Strain Analysis for Engineering Design*, 43(8):719–728, 2008.

[81] H.H. Jin, W-Y Lu, J. Chames, and N. Yang. Characterization of LIGA microsystems using digital image correlation technique and SEM imaging. In *ASME 2005 International Mechanical Engineering Congress and Exposition*, pages 457–461. American Society of Mechanical Engineers, 2005.

[82] E.M.C. Jones, M.N. Silberstein, S.R. White, and N.R. Sottos. In situ measurements of strains in composite battery electrodes during electrochemical cycling. *Experimental Mechanics*, pages 1–15, 2014.

[83] K.N. Jonnalagadda, I. Chasiotis, S. Yagnamurthy, J. Lambros, J. Pulskamp, R. Polcawich, and M. Dubey. Experimental investigation of strain rate dependence of nanocrystalline Pt films. *Experimental Mechanics*, 50:25–35, 2010.

[84] S. Joshi, W.G. Fahrenholtz, and M.J. O'Keefe. Effect of alkaline cleaning and activation on aluminum alloy 7075-t6. *Applied Surface Science*, 257(6):1859 – 1863, 2011.

[85] David C. Joy. Noise and its effects on the low-voltage SEM. In H. Schatten and J.B. Pawley, editors, *Biological Low-Voltage Scanning Electron Microscopy*, pages 129–144. Springer New York, 2008. 10.1007/978-0-387-72972-5_4.

[86] A.M. Jorge Jr., E.P., G. Ferreira de Lima, E. Rauch, M. Veron, W.J. Botta, M. Kawasaki, and T.G. Langdon. An investigation of hydrogen storage in a magnesium-based alloy processed by equal-channel angular pressing. *International Journal of Hydrogen Energy*, 38(20):8306 – 8312, 2013.

[87] A.D. Kammers and S. Daly. Digital image correlation under scanning electron microscopy: Methodology and validation. *Experimental Mechanics*, 53(9):1743–1761, 2013.

[88] A.D. Kammers and S. Daly. Self-assembled nanoparticle surface patterning for improved digital image correlation in a scanning electron microscope. *Experimental Mechanics*, 53(8):1333–1341, 2013.

[89] M. Kawasaki, Z. Horita, and T.G. Langdon. Microstructural evolution in high purity aluminum processed by ECAP. *Materials Science and Engineering: A*, 524(12):143 – 150, 2009.

[90] H.S. Kim. Finite element analysis of equal channel angular pressing using a round corner die. *Materials Science and Engineering: A*, 315(12):122 – 128, 2001.

[91] H.S. Kim, M.H. Seo, and S.I. Hong. On the die corner gap formation in equal channel angular pressing. *Materials Science and Engineering: A*, 291(12):86 – 90, 2000.

[92] K. Kim and S. Daly. Martensite strain memory in the shape memory alloy nickel-titanium under mechanical cycling. *Experimental Mechanics*, 51(4):641–652, 2011.

[93] T. Kim, C.H. Lee, S.W. Joo, and K. Lee. Kinetics of gold nanoparticle aggregation: Experiments and modeling. *Journal of Colloid and Interface Science*, 318(2):238 – 243, 2008.

[94] M. Kimiecik, J.W. Jones, and S. Daly. Quantitative studies of microstructural phase transformation in nickel-titanium. *Materials Letters*, 95(0):25 – 29, 2013.

[95] M.S. Kirugulige and H.V. Tippur. Measurement of fracture parameters for a mixed-mode crack driven by stress waves using image correlation technique and high-speed digital photography. *Strain*, 45(2):108–122, 2009.

[96] C.C. Koch and Y.S. Cho. Nanocrystals by high energy ball milling. *Nanostructured Materials*, 1(3):207 – 212, 1992.

[97] M. Köhler and W. Fritzsche. *Nanotechnology: An Introduction to Nanostructuring Techniques*. Verlag GmbH: Wiley, 2007.

[98] Y.R. Kolobov, G.P. Grabovetskaya, M.B. Ivanov, A.P. Zhilyaev, and R.Z. Valiev. Grain boundary diffusion characteristics of nanostructured nickel. *Scripta materialia*, 44(6):873–878, 2001.

[99] S. Komura, Z. Horita, M. Nemoto, and T.G. Langdon. Influence of stacking fault energy on microstructural development in equal-channel angular pressing. *Journal of Materials Research*, 14:4044–4050, 10 1999.

[100] V.I. Konstantin and V.N. Evgeny. Grain boundary sliding in ultrafine grained aluminum under tension at room temperature. *Scripta Materialia*, 66(8):511 – 514, 2012.

[101] Y.H. Kuo, C.J. Wu, J.Y. Yen, S.Y. Chen, K.Y. Tsai, and Y.Y. Chen. Silicon photodiodes for electron beam position and drift detection in scanning electron microscopy and electron beam lithography system. *Nuclear Instruments and Methods in Physics Research Section A: Accelerators, Spectrometers, Detectors and Associated Equipment*, 645(1):84 – 89, 2011.

[102] J.H. Lai and M.E. Levenston. Meniscus and cartilage exhibit distinct intra-tissue strain distributions under unconfined compression. *Osteoarthritis and Cartilage*, 18(10):1291 – 1299, 2010.

[103] T.G. Langdon. Twenty-five years of ultrafine-grained materials: Achieving exceptional properties through grain refinement. *Acta Materialia*, 61(19):7035 – 7059, 2013.

[104] V. Latysh, G.Y. Krallics, I. Alexandrov, and A. Fodor. Application of bulk nanostructured materials in medicine. *Current Applied Physics*, 6(2):262 – 266, 2006.

[105] H.J. Lee, G. Cornella, and J.C. Bravman. Stress relaxation of free-standing aluminum beams for microelectromechanical systems applications. *Applied Physics Letters*, 76(23):3415–3417, 2000.

[106] I.F. Lee, T.Q. Phan, L.E. Levine, J.Z. Tischler, P.T. Geantil, Y. Huang, T.G. Langdon, and M.E. Kassner. Using X-ray microbeam diffraction to study the long-range internal stresses in aluminum processed by ecap. *Acta Materialia*, 61(20):7741 – 7748, 2013.

[107] J.C. Lee, Y.H. Chung, H.K. Seok, J.Y. Suh, and J.H. Han. Structural evolution of a strip-cast Al alloy sheet processed by continuous equal-channel angular pressing. *Metallurgical and Materials Transactions A*, 33(3):665–673, 2002.

[108] J.C. Lee, H.K. Seok, and J.Y. Suh. Microstructural evolutions of the al strip prepared by cold rolling and continuous equal channel angular pressing. *Acta Materialia*, 50(16):4005 – 4019, 2002.

[109] N. Li, S. Guo, and M.A. Sutton. Recent progress in e-beam lithography for SEM patterning. In T. Proulx, editor, *MEMS and Nanotechnology, Volume 2*, volume 2 of *Conference Proceedings of the Society for Experimental Mechanics Series*, pages 163–166. Springer New York, 2011.

[110] N. Li, M.A. Sutton, X. Li, and H.W. Schreier. Full-field thermal deformation measurements in a scanning electron microscope by 2D digital image correlation. *Experimental Mechanics*, 48(5):635–646, 2008.

[111] S. Li, I.J. Beyerlein, D.J. Alexander, and S.C. Vogel. Texture evolution during equal channel angular extrusion: Effect of initial texture from experiment and simulation. *Scripta Materialia*, 52(11):1099 – 1104, 2005.

[112] I. Liascukiene, N. Aissaoui, S.J. Asadauskas, J. Landoulsi, and J.F. Lambert. Ordered nanostructures on a hydroxylated aluminum surface through the self-assembly of fatty acids. *Langmuir*, 28(11):5116–5124, 2012.

[113] Z. Lodziana, N.Y. Topsoe, and J.K. Norskov. A negative surface energy for alumina. *Nat Mater*, 3:289 – 293, 2004.

[114] T.C. Lowe. Metals and alloys nanostructured by severe plastic deformation: Commercialization pathways. *JOM*, 58(4):28–32, 2006.

[115] P.F. Luo, Y.J. Chao, M.A. Sutton, and W.H. Peters III. Accurate measurement of three-dimensional deformations in deformable and rigid bodies using computer vision. *Experimental Mechanics*, 33(2):123–132, 1993.

[116] J. Luster and M.A. Morris. Compatibility of deformation in two-phase Ti-Al alloys: Dependence on microstructure and orientation relationships. *Metallurgical and Materials Transactions A*, 26(7):1745–1756, 1995.

[117] M.J. Luton, C.S. Jayanth, M.M. Disko, S. Matras, and J. Vallone. Cryomilling of nanophase dispersion strengthened aluminum. *Mater Res Soc Symp Proc - Multicompon Ultrafine Microstruct*, 132:79–86, 1989.

[118] Tim Maitland and Scott Sitzman. Backscattering detector and EBSD in nanomaterials characterization. In W. Zhou and Z.L. Wang, editors, *Scanning Microscopy for Nanotechnology*, pages 41–75. Springer New York, 2006.

[119] J. May, H.W. Höppel, and M. Göken. Strain rate sensitivity of ultrafinegrained aluminium processed by severe plastic deformation. *Scripta Materialia*, 53(2):189 – 194, 2005.

[120] J. May, H.W. Höppel, and M. Göken. Strain rate sensitivity of ultrafine grained FCC- and BCC-type metals. In *Materials Science Forum*, volume 503, pages 781–786. Trans Tech Publ, 2006.

[121] M.A. McCord and M.J. Rooks. *Handbook of Microlithography, Micromachining, and Microfabrication. Volume 1: Microlithography.* Society of Photo-Optical Instrumentation Engineers, 1997.

[122] R.M. Mueller, C. Buchal, T. Oversluizen, and F. Pobell. Superconducting aluminum heat switch and plated pressure contacts for use at ultralow temperatures. *Review of Scientific Instruments*, 49(4):515–518, 1978.

[123] M.Y. Murashkin, I. Sabirov, V.U. Kazykhanov, E.V. Bobruk, A.A. Dubravina, and R.Z. Valiev. Enhanced mechanical properties and electrical conductivity in ultrafine-grained Al alloy processed via ecap-pc. *Journal of Materials Science*, 48(13):4501–4509, 2013.

[124] A.A. Nazarov, A.E. Romanov, and R.Z. Valiev. On the structure, stress fields and energy of nonequilibrium grain boundaries. *Acta Metallurgica et Materialia*, 41(4):1033 – 1040, 1993.

[125] G. Nicoletto, G. Anzelotti, and E. Riva. Mesoscopic strain fields in woven composites: Experiments vs. finite element modeling. *Optics and Lasers in Engineering*, 47(34):352 – 359, 2009.

[126] A.S. Nowick and B.S. Berry, editors. *Anelastic Relaxation in Crystalline Solids*. Academic Press, 1972.

[127] M. Ogasawara, K. Ohtoshi, and K. Sugihara. Reduction of electron beam drift caused by deflecting electrode by downflow cleaning process. *Japanese Journal of Applied Physics*, 34(12S):6655, 1995.

[128] K. Oh-ishi, A.P. Zhilyaev, and T.R. McNelley. Effect of strain path on evolution of deformation bands during ECAP of pure aluminum. *Materials Science and Engineering: A*, 410-411(0):183 – 187, 2005.

[129] H.A. Padilla, J. Lambros, A.J. Beaudoin, and I.M. Robertson. Relating inhomogeneous deformation to local texture in zirconium through grain-scale digital image correlation strain mapping experiments. *International Journal of Solids and Structures*, 49(1):18 – 31, 2012.

[130] B. Pan, A. Asundi, H. Xie, and J. Gao. Digital image correlation using iterative least squares and pointwise least squares for displacement field and strain field measurements. *Optics and Lasers in Engineering*, 47(78):865 – 874, 2009.

[131] J.W. Park, Y.J. Kim, C.H. Park, D.H. Lee, Y.G. Ko, J.H. Jang, and C.S. Lee. Enhanced osteoblast response to an equal channel angular pressing-processed pure titanium substrate with microrough surface topography. *Acta Biomaterialia*, 5(8):3272 – 3280, 2009.

[132] S. Park, P. Yang, P. Corredor, and M.J. Weaver. Transition metal-coated nanoparticle films: Vibrational characterization with surface-enhanced raman scattering. *Journal of the American Chemical Society*, 124(11):2428–2429, 2002.

[133] W.H. Peters and W.F. Ranson. Digital imaging techniques in experimental stress analysis. *Optical Engineering*, 21(3):427–431, 1982.

[134] W.H. Peters, W.F. Ranson, M.A. Sutton, T.C. Chu, and J. Anderson. Application of digital correlation methods to rigid body mechanics. *Optical Engineering*, 22(6):226738, 1983.

[135] F. Pierron, M. Sutton, and V. Tiwari. Ultra high speed DIC and virtual fields method analysis of a three point bending impact test on an aluminium bar. *Experimental Mechanics*, 51(4):537–563, 2011.

[136] C. Pithan, T. Hashimoto, M. Kawazoe, J. Nagahora, and K. Higashi. Microstructure and texture evolution in ECAE processed A5056. *Materials Science and Engineering: A*, 280(1):62 – 68, 2000.

[137] D.L. Porter and T.C. Totemeier. 22 - mechanical properties of metals and alloys. In W.F. Gale and T.C. Totemeier, editors, *Smithells Metals Reference Book (Eighth Edition)*, pages 1 – 162. Butterworth-Heinemann, Oxford, eighth edition edition, 2004.

[138] G.J. Raab, R.Z. Valiev, T.C. Lowe, and Y.T. Zhu. Continuous processing of ultrafine grained Al by ECAP-Conform. *Materials Science and Engineering: A*, 382(12):30 – 34, 2004.

[139] K. Renard, S. Ryelandt, and P.J. Jacques. Characterisation of the Portevin-Le Chátelier effect affecting an austenitic TWIP steel based on digital image correlation. *Materials Science and Engineering: A*, 527(12):2969 – 2977, 2010.

[140] S. Reyntjens and R. Puers. A review of focused ion beam applications in microsystem technology. *Journal of Micromechanics and Microengineering*, 11(4):287, 2001.

[141] J. Ribbe, D. Baither, G. Schmitz, and S.V. Divinski. Ultrafast diffusion and internal porosity in ultrafine-grained copper-lead alloy prepared by equal channel angular pressing. *Scripta Materialia*, 61(2):129 – 132, 2009.

[142] R.W. Rohde, W.B. Jones, and J.C. Swearengen. Deformation modeling of aluminum: Stress relaxation, transient behavior, and search for microstructural correlations. *Acta Metallurgica*, 29(1):41 – 52, 1981.

[143] N. Sabaté, D. Vogel, J. Keller, A. Gollhardt, J. Marcos, I. Grácia, C. Cané, and B. Michel. FIB-based technique for stress characterization on thin films for reliability purposes. *Microelectronic Engineering*, 84(5-8):1783 – 1787, 2007.

[144] I. Sabirov, M.R. Barnett, Y. Estrin, and P.D. Hodgson. The effect of strain rate on the deformation mechanisms and the strain rate sensitivity of an ultra-fine-grained Al alloy. *Scripta Materialia*, 61(2):181 – 184, 2009.

[145] I. Sabirov, M.R. Barnett, Y. Estrin, I. Timokhina, and P.D. Hodgson. Deformation mechanisms in an ultra-fine grained Al alloy. *International journal of materials research*, 100(12):1679–1685, 2009.

[146] I. Sabirov, Y. Estrin, M.R. Barnett, I. Timokhina, and P.D. Hodgson. Tensile deformation of an ultrafine-grained aluminium alloy: Micro shear banding and grain boundary sliding. *Acta Materialia*, 56(10):2223 – 2230, 2008.

[147] Y. Saito, H. Utsunomiya, H. Suzuki, and T. Sakai. Improvement in the r-value of aluminum strip by a continuous shear deformation process. *Scripta Materialia*, 42(12):1139 – 1144, 2000.

[148] Y. Saito, H. Utsunomiya, N. Tsuji, and T. Sakai. Novel ultra-high straining process for bulk materials-development of the accumulative roll-bonding (ARB) process. *Acta Materialia*, 47(2):579 – 583, 1999.

[149] S. Sasaki and J.B. Pethic. Effects of surrounding atmosphere on micro-hardness and tribological properties of sintered alumina. *Wear*, 241(2):204 – 208, 2000.

[150] X. Sauvage, G. Wilde, S.V. Divinski, Z. Horita, and R.Z. Valiev. Grain boundaries in ultrafine grained materials processed by severe plastic deformation and related phenomena. *Materials Science and Engineering: A*, 540(0):1 – 12, 2012.

[151] H.W. Schreier, J.R. Braasch, and M.A. Sutton. Systematic errors in digital image correlation caused by intensity interpolation. *Optical Engineering*, 39(11):2915–2921, 2000.

[152] R.A. Schwarzer, D.P. Field, B.L. Adams, M. Kumar, and A.J. Schwartz. Present state of electron backscatter diffraction and prospective developments. In A.J. Schwartz, M. Kumar, B.L. Adams, and D.P. Field, editors, *Electron Backscatter Diffraction in Materials Science*, pages 1–20. Springer US, 2009.

[153] W.A. Scrivens, Y. Luo, M.A. Sutton, S.A. Collette, M.L. Myrick, P. Miney, P.E. Colavita, A.P. Reynolds, and X. Li. Development of patterns for digital image correlation measurements at reduced length scales. *Experimental Mechanics*, 47:63–77, 2007.

[154] V.M. Segal. Materials processing by simple shear. *Materials Science and Engineering: A*, 197(2):157 – 164, 1995.

[155] V.M. Segal, V.I. Reznikov, A.E. Drobyshevskii, and V.I. Kopylov. Plastic treatment of metals by simple shear. *Russian Metallurgy*, 1:115–123, 1981.

[156] S.L Semiatin, P.B Berbon, and T.G Langdon. Deformation heating and its effect on grain size evolution during equal channel angular extrusion. *Scripta Materialia*, 44(1):135 – 140, 2001.

[157] T. Shimokawa, T. Hiramoto, T. Kinari, and S. Shintaku. Effect of extrinsic grain boundary dislocations on mechanical properties of ultrafine-grained metals by molecular dynamics simulations. *Materials Transactions*, 50(1):2–10, 2009.

[158] D.H. Shin, B.C. Kim, Y.S. Kim, and K.T. Park. Microstructural evolution in a commercial low carbon steel by equal channel angular pressing. *Acta Materialia*, 48(9):2247 – 2255, 2000.

[159] D.H. Shin, I. Kim, J. Kim, Y.S. Kim, and S.L. Semiatin. Microstructure development during equal-channel angular pressing of titanium. *Acta Materialia*, 51(4):983 – 996, 2003.

[160] V. Skripnyuk, E. Buchman, E. Rabkin, Y. Estrin, M. Popov, and S. Jorgensen. The effect of equal channel angular pressing on hydrogen storage properties of a eutectic Mg-Ni alloy. *Journal of Alloys and Compounds*, 436(1-2):99 – 106, 2007.

[161] V.M. Skripnyuk, E. Rabkin, Y. Estrin, and R. Lapovok. The effect of ball milling and equal channel angular pressing on the hydrogen absorption/desorption properties of Mg-4.95 wt% Zn-0.71 wt% Zr (ZK60) alloy. *Acta Materialia*, 52(2):405 – 414, 2004.

[162] V.M. Skripnyuk, E. Rabkin, Y. Estrin, and R. Lapovok. Improving hydrogen storage properties of magnesium based alloys by equal channel angular pressing. *International Journal of Hydrogen Energy*, 34(15):6320 – 6324, 2009.

[163] N.A. Smirnova, V.I. Levit, V.I. Pilyugin, R.I. Kuznetsov, L.S. Davydova, and V.A. Sazonova. Evolution of the structure of f.c.c. single crystal subjected to strong plastic deformation. *Fiz. Met. Metalloved.*, 61:1170–1177, 1986.

[164] H.I. Smith, S.D. Hector, M.L. Schattenburg, and E.H. Anderson. A new approach to high fidelity e-beam and ion-beam lithography based on an in-situ global-fiducial grid. *Journal of Vacuum Science & Technology B*, 9(6):2992–2995, 1991.

[165] V.V. Stolyarov, Y.T. Zhu, I.V. Alexandrov, T.C. Lowe, and R.Z. Valiev. Influence of ECAP routes on the microstructure and properties of pure Ti. *Materials Science and Engineering: A*, 299(1-2):59 – 67, 2001.

[166] M.G. Stout and J.A. O'Rourke. Experimental deformation textures of OFE copper and 70:30 brass from wire drawing, compression, and torsion. *Metallurgical Transactions A*, 20(1):125–131, 1989.

[167] M.G. Stout, A.D. Rollett, J.S. Kallend, M.L. Lovato, M.A. Przystupa, and U.F. Kocks. Material dependence of deformation texture development. In *Journal of Metals*, volume 39, pages A18–A18. Minerals Metals Materials Soc, Warrendale, PA, USA, 1987.

[168] T. Suo, Y. Chen, Y. Li, C. Wang, and X. Fan. Strain rate sensitivity and deformation kinetics of ECAPed aluminium over a wide range of strain rates. *Materials Science and Engineering: A*, 560(0):545 – 551, 2013.

[169] M. Sutton, N. Li, D. Garcia, N. Cornille, J. Orteu, S. McNeill, H. Schreier, X. Li, and A. Reynolds. Scanning electron microscopy for quantitative small and large deformation measurements part II: Experimental validation for magnifications from 200 to 10,000. *Experimental Mechanics*, 47:789–804, 2007.

[170] M. Sutton, N. Li, D. Joy, A. Reynolds, and X. Li. Scanning electron microscopy for quantitative small and large deformation measurements part I: SEM imaging at magnifications from 200 to 10,000. *Experimental Mechanics*, 47:775–787, 2007.

[171] M.A. Sutton, N. Li, D. Garcia, N. Cornille, J.J. Orteu, S.R. McNeill, H.W. Schreier, and X. Li. Metrology in a scanning electron microscope: theoretical developments and experimental validation. *Measurement Science and Technology*, 17(10):2613, 2006.

[172] M.A. Sutton, S.R. McNeill, J.D. Helm, and Y.J. Chao. Advances in two-dimensional and three-dimensional computer vision. In Pramod Rastogi, editor, *Photomechanics*, volume 77 of *Topics in Applied Physics*, pages 323–372. Springer Berlin Heidelberg, 2000.

[173] M.A. Sutton, C. Mingqi, W.H. Peters, Y.J. Chao, and S.R. McNeill. Application of an optimized digital correlation method to planar deformation analysis. *Image and Vision Computing*, 4(3):143 – 150, 1986.

[174] M.A. Sutton, J.J. Orteu, and H. Schreier. *Image Correlation for Shape, Motion and Deformation Measurements: Basic Concepts,Theory and Applications*. Springer Publishing Company, Incorporated, 1st edition, 2009.

[175] M.A. Sutton, W.J. Wolters, W.H. Peters, W.F. Ranson, and S.R. McNeill. Determination of displacements using an improved digital correlation method. *Image and Vision Computing*, 1(3):133 – 139, 1983.

[176] S.D. Terhune, D.L. Swisher, K. Oh-Ishi, Z. Horita, T.G. Langdon, and T.R. McNelley. An investigation of microstructure and grain-boundary evolution during ECA pressing of pure aluminum. *Metallurgical and Materials Transactions A*, 33(7):2173–2184, 2002.

[177] M.A. Tschopp, B.B. Bartha, W.J. Porter, P.T. Murray, and S.B. Fairchild. Microstructure-dependent local strain behavior in polycrystals through *In-Situ* scanning electron microscope tensile experiments. *Metallurgical and Materials Transactions A*, 40:2363–2368, 2009.

[178] R.Z. Valiev. Nanostructuring of metals by severe plastic deformation for advanced properties. *Nature materials*, 3(8):511–516, 2004.

[179] R.Z. Valiev, I.V. Alexandrov, Y.T. Zhu, and T.C. Lowe. Paradox of strength and ductility in metals processed by severe plastic deformation. *Journal of Materials Research*, 17:5–8, 1 2002.

[180] R.Z. Valiev, N.A. Enikeev, M.Y. Murashkin, V.U. Kazykhanov, and X. Sauvage. On the origin of the extremely high strength of ultrafine-grained al alloys produced by severe plastic deformation. *Scripta Materialia*, 63(9):949 – 952, 2010.

[181] R.Z. Valiev, Y. Estrin, Z. Horita, T.G. Langdon, M.J. Zechetbauer, and Y.T. Zhu. Producing bulk ultrafine-grained materials by severe plastic deformation. *JOM*, 58(4):33–39, 2006.

[182] R.Z Valiev, R.K Islamgaliev, and I.V Alexandrov. Bulk nanostructured materials from severe plastic deformation. *Progress in Materials Science*, 45(2):103 – 189, 2000.

[183] R.Z. Valiev, A.V. Korznikov, and R.R. Mulyukov. Structure and properties of ultrafine-grained materials produced by severe plastic deformation. *Materials Science and Engineering: A*, 168(2):141 – 148, 1993.

[184] R.Z. Valiev, E.V. Kozlov, Y.F. Ivanov, J. Lian, A.A. Nazarov, and B. Baudelet. Deformation behaviour of ultra-fine-grained copper. *Acta Metallurgica et Materialia*, 42(7):2467 – 2475, 1994.

[185] R.Z. Valiev, N.A. Krasilnikov, and N.K. Tsenev. Plastic deformation of alloys with submicron-grained structure. *Materials Science and Engineering: A*, 137(0):35 – 40, 1991.

[186] R.Z. Valiev and T.G. Langdon. Principles of equal-channel angular pressing as a processing tool for grain refinement. *Progress in Materials Science*, 51(7):881 – 981, 2006.

[187] R.Z. Valiev, I.P. Semenova, V.V. Latysh, H. Rack, T.C. Lowe, J. Petruzelka, L. Dluhos, D. Hrusak, and J. Sochova. Nanostructured titanium for biomedical applications. *Advanced Engineering Materials*, 10(8):B15–B17, 2008.

[188] J. van den Brand, P.C. Snijders, W.G. Sloof, H. Terryn, and J.H.W. de Wit. Acid-base characterization of aluminum oxide surfaces with XPS. *The Journal of Physical Chemistry B*, 108(19):6017–6024, 2004.

[189] W.J. van Ooij and D. Zhu. Electrochemical impedance spectroscopy of bis-[triethoxysilylpropyl] tetrasulfide on Al 2024-T3 substrates. *Corrosion*, 57:413–427, 2001.

[190] VIC-2D. *version 2009*. Correlated Solutions, Inc., Columbia, SC, 2009.

[191] J. Walley, R. Wheeler, M. Uchic, and M. Mills. *In-Situ* mechanical testing for characterizing strain localization during deformation at elevated temperatures. *Experimental Mechanics*, 52:405–416, 2012.

[192] C.T. Wang, N. Gao, M.G. Gee, R.J.K. Wood, and T.G. Langdon. Processing of an ultrafine-grained titanium by high-pressure torsion: An evaluation of the wear properties with and without a tin coating. *Journal of the Mechanical Behavior of Biomedical Materials*, 17(0):166 – 175, 2013.

[193] B. Wattrisse, A. Chrysochoos, J.-M. Muracciole, and M. Nmoz-Gaillard. Analysis of strain localization during tensile tests by digital image correlation. *Experimental Mechanics*, 41(1):29–39, 2001.

[194] Y. Wei, A.F. Bower, and H. Gao. Enhanced strain-rate sensitivity in fcc nanocrystals due to grain-boundary diffusion and sliding. *Acta Materialia*, 56(8):1741 – 1752, 2008.

[195] J.M. Wheeler, V. Maier, K. Durst, M. Göken, and J. Michler. Activation parameters for deformation of ultrafine-grained aluminium as determined by indentation strain rate jumps at elevated temperature. *Materials Science and Engineering: A*, 585(0):108 – 113, 2013.

[196] D.B. Witkin and E.J. Lavernia. Synthesis and mechanical behavior of nanostructured materials via cryomilling. *Progress in Materials Science*, 51(1):1 – 60, 2006.

[197] C. Xu, M. Furukawa, Z. Horita, and T.G. Langdon. Using ECAP to achieve grain refinement, precipitate fragmentation and high strain rate superplasticity in a spray-cast aluminum alloy. *Acta Materialia*, 51(20):6139 – 6149, 2003.

[198] Q. Xue, I.J. Beyerlein, D.J. Alexander, and G.T. Gray III. Mechanisms for initial grain refinement in ofhc copper during equal channel angular pressing. *Acta Materialia*, 55(2):655 – 668, 2007.

[199] A. Yamashita, Z. Horita, and T.G. Langdon. Improving the mechanical properties of magnesium and a magnesium alloy through severe plastic deformation. *Materials Science and Engineering: A*, 300(1-2):142 – 147, 2001.

[200] B.D. Yan, S. Meilink, G.W. Warren, and P. Wynblatt. Water adsorption and surface conductivity measurements on θ-alumina) substrates. *Components, Hybrids, and Manufacturing Technology, IEEE Transactions on*, 10(2):247–251, Jun 1987.

[201] S. Yoneyama, A. Kitagawa, S. Iwata, K. Tani, and H. Kikuta. Bridge deflection measurement using digital image correlation. *Experimental Techniques*, 31(1):34–40, 2007.

[202] Y. Zhang, T.D. Topping, E.J. Lavernia, and S.R. Nutt. Dynamic micro-strain analysis of ultrafine-grained aluminum magnesium alloy using digital image correlation. *Metallurgical and Materials Transactions A*, 45(1):47–54, 2014.

[203] A.P. Zhilyaev and T.G. Langdon. Using high-pressure torsion for metal processing: Fundamentals and applications. *Progress in Materials Science*, 53(6):893 – 979, 2008.

[204] A.P. Zhilyaev, D.L. Swisher, K. Oh-ishi, T.G. Langdon, and T.R. McNelley. Microtexture and microstructure evolution during processing of pure aluminum by repetitive ecap. *Materials Science and Engineering: A*, 429(1-2):137 – 148, 2006.

[205] T. Zhu, M.A. Sutton, N. Li, J.J. Orteu, N. Cornille, X. Li, and A.P. Reynolds. Quantitative stereovision in a scanning electron microscope. *Experimental Mechanics*, 51:97–109, 2011.

[206] Y.T. Zhu and T.C. Lowe. Observations and issues on mechanisms of grain refinement during ECAP process. *Materials Science and Engineering: A*, 291(1-2):46 – 53, 2000.